Electrophysiological, Hemodynamic, and Metabolic Effects of Transcranial Photobiomodulation (tPBM) on Topographical and Physiological Connectivity in the Human Brain

Sadra Shahdadian

Presented to the Faculty of the Graduate School of
The University of Texas at Arlington in Partial Fulfillment
Of the Requirements
For the Degree of

DOCTOR OF PHILOSOPHY

THE UNIVERSITY OF TEXAS AT ARLINGTON
August 2022

ACKNOWLEDGMENTS

First, I would like to acknowledge and thank my supervising professor, Dr. Hanli Liu for her guidance, mentorship, and support towards completing the degree. Her professional guidance and powerful encouragement made this work possible.

Second, I would like to thank my committee members, Dr. Alexandrakis, Dr. Busch, and Dr. Wang for their time and guidance on this work.

Third, I would like to extend my appreciation to fellow doctoral, post-doctoral colleagues for their assistance and support in my research including Dr. Xinlong Wang, Dr. Nghi Troung, Dr. Anqi Wu, Dr. Parisa Rabbani, Dr. Hashini Wanniarachchi, Dr. Tyrell Pruitt, Dr. Akhil Chaudhari, Kang Shu, Caroline Carter, Haylea Renguul, Sheetala Ranjitkar, Sylvine Ineza.

Finally, and most importantly, I would like to thank my parents, Dr. Javad Shahdadian and Dr. Zohreh Esmaili, and my sister Ms. Sana Shahdadian who have always supported and encouraged me during my long journey. Special thanks to my fiancé, Ms. Yasamin Mahboub for her unconditional support and encouragement throughout the past year.

ABSTRACT

Electrophysiological, Hemodynamic, and Metabolic Effects of Transcranial Photobiomodulation (tPBM) on Topographical and Physiological Connectivity in the Human Brain

Sadra Shahdadian

The University of Texas at Arlington, 2022

Supervising Professor: Dr. Hanli Liu

Transcranial photobiomodulation (tPBM) targets the human brain with near-infrared (NIR) light and is shown to affect human cognitive performance and neural electrophysiological activity as well as concentration changes of oxidized cytochrome-c-oxidase (Δ[CCO]) and hemoglobin oxygenation (Δ[HbO]) in human brain.

Brain topographical connectivity, which shows the communication between regions of the brain, and its alteration can be assessed to quantify the effects of external stimuli, diseases, and cognitive decline, in resting-state or task-based measurements. Furthermore, understanding the interactions between different physiological representations of neural activity, namely electrophysiological, hemodynamic, and metabolic signals in the human brain, has been an important topic among researchers in recent decades. In my doctoral study, neurophysiological networks were constructed using frequency-domain analyses on oscillations of electroencephalogram (EEG), Δ[CCO], and Δ[HbO] time series that were acquired by a portable EEG and 2-channel broadband near-infrared spectroscopy (2-bbNIRS).

Specifically, my dissertation included three aims. The first one was to examine how tPBM altered the topographical connectivity in the electrophysiological oscillations of the resting human brain. As the first step, I defined and found key regions and clusters in the EEG sensor space that were affected the most by tPBM during and after the stimulation using both cluster-based power analysis and graph-based connectivity analysis. The results showed that the right prefrontal 1064-nm tPBM modulates several global and regional electrophysiological networks by shifting the information path towards frontal regions, especially in the beta band. For the second aim, I performed 2-bbNIRS measurements from 26 healthy humans and developed a methodology that enabled quantification of the infra-slow oscillation (ISO) power and connectivity between bilateral frontal regions of the human brain in resting state and in response to frontal tPBM stimulation at different sites and laser wavelengths. As the result, several stable and consistent features were extracted in the resting state of 26 young healthy adults. Moreover, these features were used to reveal some effects of tPBM on prefrontal metabolism and hemodynamics, while illustrating the similarities and differences between different stimulation conditions. Finally, the third aim was to investigate the resting-state prefrontal physiological network and the corresponding modulation in response to left frontal 800-nm tPBM by determining the effective connectivity/coupling between each pair of the electrophysiological, hemodynamic, and metabolic ISO of the human brain. Complementary to the previous studies, my study showed that prefrontal tPBM not only modulates the information path between two locations of the prefrontal cortex, it can also induce unilateral alterations in interactions between neural activity, hemodynamics, and metabolism. Overall, my dissertation shed light on the mechanism of action of prefrontal tPBM.

Table of Contents

List of Figures

List of Tables

Chapter 1

Introduction

1.1 Significance and Specific Aims

A type of photobiomodulation technique known as transcranial photobiomodulation (tPBM) targets the human brain with near-infrared (NIR) light [1] and human performance on a variety of cognitive tasks has been shown to improve in several studies using tPBM with different wavelengths for laser and LED [2-6]. Our group has previously shown that tPBM enabled significant upregulation in concentrations of oxidized cytochrome-c-oxidase ([CCO]) and hemoglobin oxygenation ([HbO]) during and after tPBM on the right forehead using broadband near-infrared spectroscopy (bbNIRS) [7-9]. These studies support the hypothesis that tPBM photo-oxidizes CCO to boost the metabolism of cells [1, 10, 11].

Electroencephalogram (EEG) is commonly used to monitor and record the electrical activity of neurons. Brain functional (topographical) connectivity, which shows the communication between regions of the brain, can be utilized as a measure to understand the effects of stimuli, diseases, and cognitive decline, in resting-state or task-based measurements [13-20]. Understanding the correlation between different physiological systems, namely electrophysiological, hemodynamic, and metabolic systems in the human brain, has been an attractive topic among researchers in recent decades [21-25]. In this study, Neurovascular, neurometabolic, and metabolic-vascular coupling is calculated using oscillations of EEG, Δ[HbO], and Δ[CCO] time series to investigate the connectivity between different physiological systems in a specific region of the brain.

The goal of this study is to examine how tPBM can alter the topographical and physiological connectivity in the electrophysiological, hemodynamic, and metabolic systems of the human brain in resting state. As the first step, I found the regions and clusters in EEG sensor space that have been affected the most by tPBM during and after stimulation using both cluster-based power analysis and graph-based connectivity analysis. In the second step, I assessed the power and connectivity between bilateral frontal regions of the human brain in resting state and in response to different conditions of tPBM using two-channel bbNIRS system. Finally, I quantified the modulation in metabolic-vascular and physiological network in rest and in response to left frontal tPBM by determining the effective connectivity between electrophysiological, hemodynamic, and metabolic oscillations of the human brain using a dual-modality (i.e., EEG and bbNIRS) dataset.

1.1.1 The need for a topographical mapping of the brain's electrophysiological network modulation in response to tPBM

The electrophysiological response of the human brain to tPBM is not well studied and understood. All previous studies utilized either laser or LED sources of NIR light and recorded the electrophysiological responses using a 19-channel (i.e., the 10-20 EEG electrode placement) or 64-channel (i.e., the 10-10 electrode placement) EEG system. Power spectral density (PSD) analysis and graph theory analysis (GTA) are two major data analysis methods. Graph theory is a branch of mathematics that can serve as a theoretical tool for quantifying the specific features of network architecture (topology). The outcome of GTA can provide information on the anatomical localization of areas responding to given stimuli or tasks (topography), or human brain functional connectivity and networks [26].

Although the previous studies have consistently reported that tPBM enables alterations in EEG PSDs, different tPBM protocols, such as laser versus LEDs, 19- versus 64-channel electrodes, and PSD versus GTA analysis, have given rise to sparse and incomparable findings. For example, only two studies reported 64-channel EEG responses to tPBM [27, 28], but they did not examine tPBM-induced topological alterations in brain connectivity. On the other hand, based on 19-channel EEG, two recent studies reported tPBM-induced modulations of global network parameters [29] and alterations in brain connectivity between the two hemispheres [30], respectively. However, light stimulation was delivered at different cortical regions, either locally at the right forehead or at multiple scalp sites near the default mode network, and by LEDs.

The distinct focus of this study was to investigate tPBM-induced modulations of EEG functional connectivity by performing GTA on a 64-channel EEG, followed by quantification of changes in brain connectivity in global network metrics and 10 nodal/local regions. Specifically, I identified 10 cortical clusters in the sensor space that were most affected by tPBM during and after stimulation. Next, cluster-based permutation testing after PSD analysis was performed to identify topographical regions that were significantly modulated by tPBM. Then, global and nodal graphical measures or metrics were obtained based on GTA, revealing respective augments of functional connectivity, brain network, and information pathways in response to tPBM.

1.1.2 The need for a topographical mapping of the resting state prefrontal cortex hemodynamic and metabolic network

Many studies have focused on investigating the mechanism of cerebral metabolic activity and have found vasomotion to be a major source of metabolic and hemodynamic modulations [31-35]. Vasomotion is a spontaneous oscillation that originates from the blood vessel wall with an infra-slow oscillation (ISO) of 0.005-0.2 Hz [36, 37]. In addition, a correlation is found between the ISO of cerebral metabolic activities and human cognitive functions [38]. Furthermore, vasomotion malfunction has been observed in older adults and in patients with different diseases, such as atherosclerosis [39], cardiovascular disease [40], and Alzheimer’s disease [41]. Thus, it may be beneficial to quantify and characterize cerebral metabolism in the ISO range, which may provide better insight into neurophysiological mechanisms and discover features that differ between healthy humans and patients with brain disorders.

In the present exploratory study [42], I hypothesized that 2-bbNIRS, along with frequency-domain analysis, one can quantify prefrontal cortical connectivity and coupling of ISO in the resting human brain. Specifically, the features analyzed from the 2-bbNIRS time series included (1) resting-state spectral amplitude (SA) of bilateral cortical hemodynamic and metabolic (i.e., SA_{HbO_i} and SA_{CCO_i}) activities, where i represents either the left or right prefrontal region, (2) bilateral hemodynamic connectivity ($bCON_{HbO}$), (3) bilateral metabolic connectivity ($bCON_{CCO}$), and (4) coupling between cerebral hemodynamic and metabolic activities on the unilateral side ($uCOP_{HbO\text{-}CCO\_i}$) of the prefrontal cortex over the three ISO frequency bands. Then the results support this hypothesis by presenting relatively stable and consistent values for these features in healthy young humans, revealing the translation potential of these features for future clinical applications.

1.1.3 The need for a topographical mapping of the prefrontal cortex hemodynamic and metabolic network in response to different wavelengths and stimulation sites of tPBM

Our group recently introduced a set of hemodynamic and metabolic characteristics quantified by frequency-domain spectral amplitude and connectivity analysis of hemodynamic and metabolic ISO activity of prefrontal cortex, assessed by a dual-channel bbNIRS setup [43]. These metrics are (1) bilateral hemodynamic (i.e., [HbO]) connectivity, (2) bilateral metabolic (i.e., [CCO]) connectivity, (3) unilateral hemodynamic-metabolic coupling on the left and (4) right side of the prefrontal cortex. In addition, we have demonstrated that these constant and relatively reproducible characteristics can be considered potential biomarkers to identify neurological disorders and diseases [44]. Furthermore, we have shown distinct alterations in these metrics as well as Δ[HbO] and Δ[CCO] ISO spectral amplitudes across all three frequency bands in response to 1064-nm tPBM. Modulation of Δ[HbO] and Δ[CCO] in response to tPBM is also demonstrated to be wavelength-dependent in another study [12]. As reported in [12], 800-850 nm wavelengths enable CCO to be more stimulated with an increased concentration. On the other hand, 1064 nm laser have demonstrated its effect on enhancement of human cognition. 1064 nm is not at the absorption peak of CCO, but it has much less light scattering ability or a smaller light scattering coefficient than that at 800–850 nm light which leads to deeper penetration in tissue. Moreover, no behavioral or physiological alteration is reported in response to left prefrontal tPBM. Thus, it would be beneficial to investigate the effect of the laser's wavelength and stimulation site on the alteration of the proposed metrics.

In this study, young healthy human participants were at rest while Δ[HbO] and Δ[CCO] time series with a sampling frequency of 0.67 Hz were acquired using a 2-bbNIRS system from two sides of the prefrontal cortex in pre- and post-tPBM. These time series were then analyzed to quantify the amplitude and coherence of hemodynamic and metabolic ISO over three frequency bands. In the first set of analyses, I assessed the spectral amplitude of hemodynamic and metabolic activity (SA_{HbO} and SA_{CCO}) over the three ISO frequency bands. Then, four physiological metrics were used to characterize the connectivity/coupling between each pair of signals. These measures include (1) bilateral hemodynamic connectivity ($bCON_{HbO}$), (2) bilateral metabolic connectivity ($bCON_{CCO}$), (3) coupling between cerebral hemodynamic and metabolic activities on the ipsilateral side to the stimulation ($uCOP_{Ipsi}$), and (4) coupling between cerebral hemodynamic and metabolic activities on the contralateral side to the stimulation ($uCOP_{Contra}$), of the prefrontal cortex over the three ISO frequency bands. Five separate visits with different conditions were used for each participant including 8 minutes of (1) Right prefrontal 800-nm laser, (2) Right prefrontal 850-

nm laser, (3) Right prefrontal sham, (4) Left prefrontal 800-nm laser, (5) Left prefrontal sham in a randomized order.

Then results support the hypothesis that hemodynamic and metabolic ISO is significantly modulated by tPBM. This modulation is distinct for each frequency band, can be local or bilateral/global, and in some cases is closely related to the wavelength and stimulation location. These observations can be beneficial for further investigation of the mechanism behind cerebral metabolism as well as wavelength- or location-specific cognitive function improvement or treatment of neurological disorder/disease based on the modulated metric and frequency band.

1.1.4 The need for a physiological connectivity assessment of the brain's electrophysiological, hemodynamic, and metabolic network modulation in response to tPBM

Investigation of the intertwined behavior of hemodynamic and metabolic ISO activities can be facilitated by assessment of metabolic-vascular coupling (MVC), and utilizing EEG and bbNIRS in parallel opens the door to the assessment of neurometabolic coupling (NMC). Although these different metrics can be assessed separately, they can be observed as a semi-complex physiological network of a specific region in the cerebral cortex where electrophysiological (here, the beta band of EEG), hemodynamic, and metabolic activity are the nodes, and these coupling metrics are the links between them. Furthermore, the level by which the hemodynamic and metabolic activities on lateral sides of prefrontal cortex are interacting can be quantified by the topographical functional connectivity.

In this study, a dual-mode setup (EEG and bbNIRS) was utilized to assess the topographical effective connectivity between lateral prefrontal hemodynamic and metabolic ISO to identify any directionality between these activities in young healthy human adults at rest. In addition, local

MVC was quantified to determine the effective coupling between hemodynamic and metabolic ISO. Furthermore, I constructed two local physiological networks on the lateral prefrontal cortices consisting of a beta band of EEG, Δ[HbO], Δ[CCO] as nodes, and NVC, NMC, and MVC as links. Finally, I quantified the tPBM-induced changes in the abovementioned networks and investigated any possible alterations in information flow among these nodes.

Then the results support the hypothesis that resting-state interactions between electrophysiological, hemodynamic, and metabolic ISO is mostly bi-directionally balanced and they can be significantly altered by tPBM. This modulation can be local or bilateral/global. These observations can be beneficial for further investigation of the mechanism behind NVC, NMC, and MVC as well as location-specific cognitive function improvement or treatment of neurological disorders/diseases based on the modulated metrics.

Chapter 2

Neuromodulation of brain topography and network topology by prefrontal transcranial photobiomodulation

Sadra Shahdadian, Xinlong Wang, Hashini Wanniarachchi, Hanli Liu

(This chapter is a manuscript that is under revision in Journal of Neural Engineering)

2.1 Introduction

Transcranial photobiomodulation (tPBM) is a non-invasive neuromodulation technique that delivers near-infrared (NIR) light to the human brain using lasers or light-emitting diode (LED) clusters [11, 45-47]. Recent studies have demonstrated the promising effects of tPBM in treating traumatic brain injuries [47-51], psychiatric or neurological disorders [52-55], and in enhancing cognitive performance in normal humans [2-6, 56]. To better understand the underlying mechanism of tPBM, neurophysiological measurements of the human brain were performed non-invasively from healthy human controls using an optical spectroscopy approach before, during, and after prefrontal tPBM. The results of these measures quantified and demonstrated tPBM-induced increases in mitochondrial metabolism (i.e., the redox state of cytochrome-c-oxidase (Δ[CCO])) and hemodynamic oxygenation (i.e., oxygenated haemoglobin (Δ[HbO])) [7-9]. Moreover, it was shown that the increases in both Δ[CCO] and Δ[HbO] were not caused by the thermal effects of the tPBM [57], hardware-related noise, or drift [58, 59]. All these published reports provide strong support that tPBM facilitates the photo-oxidization of mitochondrial CCO to boost the cellular metabolism of neurons [1, 10, 11].

However, the electrophysiological response of the human brain to tPBM is not well studied and understood. Table 2.1 summarizes the recently published articles that reported scalp electroencephalography (EEG) responses to tPBM with the respective measurement and analysis parameters. All studies utilized either laser or LED clusters of NIR light sources and recorded the electrophysiological responses using a 19-channel (i.e., the 10-20 EEG electrode placement) or 64-channel (i.e., the 10-10 electrode placement) EEG system. Pruitt et al. [12] have shown that the laser and LED have different effects on the stimulated tissue in terms of changes hemodynamic and metabolic activity which is mainly due to significantly lower irradiance of LED sources, which is a result of broader bandwidth of LED compared to laser. The table also lists two major data analysis methods, namely, power spectral density (PSD) analysis and graph theory analysis (GTA). Graph theory is a branch of mathematics that can serve as a theoretical tool for quantifying the specific features of network architecture (topology). The outcome of GTA can provide information on the anatomical localization of areas responding to given stimuli or tasks (topography), or human brain functional connectivity and networks [26].

Table 2.1 List of references that reported EEG responses to tPBM with related measurement and analysis parameters

Refs.	Authors	Source of tPBM	Location of tPBM	# of Subjects	# of Channels	PSD analysis	Graph-theory based connectivity analysis
[60]	Berman, et al., 2017	Multiple LED clusters (1070 nm)	Whole head	19	19	No. It was based on qEEG analysis	No
[30]	Ghaderi, et al., 2021	1 cluster of LED (850 nm)	Right forehead	40	19	No.	Yes; changes in connectivity within each of or between two hemispheres
[61]	Spera, et al.	4 clusters of LED (830 nm)	Bilateral frontal	10	19	Yes, with topography	No
[5]	Vargas, et al. 2017	Laser (1064 nm)	Right forehead	12	19	Yes, but no topography	No
[27]	Wang, et al., 2021	Laser (1064 nm)	Right forehead	46	64	Yes, with topography	No
[28]	Wang, et al. 2022	Laser (1064 nm)	Right forehead	44	64	No. It was based on singular value decompensation	No
[29]	Zomorrodi, et al., 2019	3 clusters of LED (810 nm)	3 default mode locations	20	19	Yes, with topography	Yes; changes in global connectivity parameters only
	Current study	Laser (1064 nm)	Right forehead	45	64	Yes, with topography	Yes; changes of connectivity in global network metrics and 10 nodal regions

PSD is the most common method for analysing EEG data and gives rise to an absolute oscillation power spectrum of local electrophysiological signals in the frequency range of 0.5 to 70 Hz or higher. Frequency-dependent PSD values facilitate a better understanding of the effects or impacts of external stimuli, cognitive decline, disturbances in consciousness, and certain brain disorders in the human brain [13, 16-20]. However, statistical analysis of multi-channel EEG is challenging when conducting multi-variable comparisons (e.g., 64 comparisons for 64 channels) [62, 63]. Cluster-based permutation testing is an established method for minimizing type-I errors in null hypothesis testing for these datasets. This method is based on the fact that the electrophysiological time series of brain oscillations is highly correlated with neighbouring channels [63]. Using cluster-based permutation testing, we identified topographical clusters of EEG channels on the human scalp template, where frequency-specific EEG oscillation powers were significantly altered between two different conditions (i.e., active tPBM versus sham intervention). Consequently, the corresponding brain regions with modulated powers were identified.

Topologically, GTA is a practical and quantitative approach for characterizing functional connectivity and networks in the human brain [64]. In this method, a network is considered a mathematical representation of a real-world complex system and is defined by the composition of nodes (vertices) and links (edges) between pairs of nodes. The outcome of GTA measures mainly represents the functional integration, segregation, and centrality of the network, all of which can topologically characterize changes in brain functional connectivity in both global and nodal regions [14, 15, 65]. When GTA is used to analyse EEG data, the scalp locations of the EEG electrodes represent the network nodes, and the links among the electrodes represent the functional connections between these nodes [14].

In general, both PSD and GTA-derived parameters or metrics can provide instructive information on functional brain networks in the resting state or under external neuromodulation. Because multi-channel EEG signals contain rich information in the temporal, spectral, and spatial domains, these pieces of information can be grouped temporally and/or spectrally to visualize brain activation and networks in topographical clusters and regions [66, 67].

Although the studies summarized in Table 2.1 have consistently reported that tPBM enables alterations in EEG PSDs, different tPBM protocols, such as laser versus LEDs, 19- versus 64-channel electrodes (i.e. instrument with low cost and low setup time versus high spatial resolution data), and PSD versus GTA analysis, have given rise to sparse and incomparable findings. For example, only two studies reported 64-channel EEG responses to tPBM [27, 28], but they did not examine tPBM-induced topological alterations in brain connectivity. On the other hand, based on 19-channel EEG, two recent studies reported tPBM-induced modulations of global network parameters [29] and alterations in brain connectivity between the two hemispheres [30], respectively. However, light stimulation was delivered at different cortical regions, either locally at the right forehead or at multiple scalp sites near the default mode network, and by LEDs.

As shown in Table 2.1, the distinct focus of this study was to investigate tPBM-induced modulations of EEG functional connectivity by performing GTA on a 64-channel EEG, followed by quantification of changes in brain connectivity in global network metrics and 10 nodal/local regions. Specifically, we identified 10 cortical clusters in the sensor space (scalp EEG) that were most affected by tPBM during and after stimulation. Next, cluster-based permutation testing after PSD analysis was performed to identify topographical regions that were significantly modulated by tPBM. Then, global and nodal graphical measures or metrics were obtained based on GTA, revealing respective augments of functional connectivity, brain network, and information pathways in response to tPBM.

2.2 Materials and methods

2.2.1 Participants

A total of 49 healthy human subjects (30 men and 19 women; 26 ± 8.8 years of age) were enrolled from the local community of the university. The subjects were seated on a chair with closed eyes in resting state during the measurement. Four subjects were removed from the dataset because of self-reported or observed tiredness or sleepiness (through subjects' movement and EEG signal) during the measurement, resulting in 45 participants being considered for further data analysis. The participants were instructed to refrain from consuming any caffeinated drinks for at least 3 h before each experiment. All measurements were obtained with informed consent from each participant.

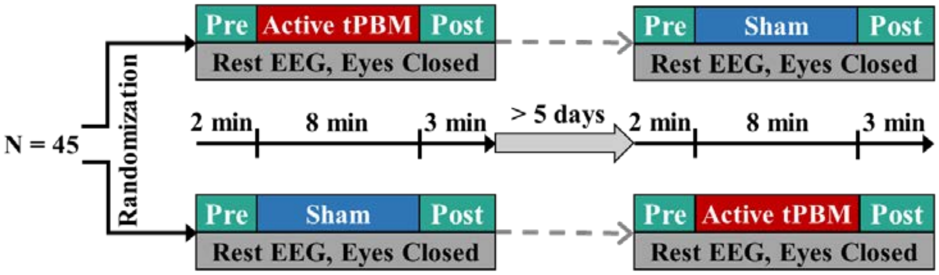

Figure 2.1 A crossover experimental protocol for tPBM and sham experiments (n=45) with simultaneous EEG recording. The participants were at wakeful resting state with eyes closed.

2.2.2 Experimental setup and protocol

In this study, tPBM and sham experiments were performed using a continuous-wave laser at 1064 nm (Model CG-5000 Laser, Cell Gen. Therapeutics LLC, Dallas, TX, USA), which was cleared by the Food and Drug Administration (FDA). The laser was delivered to each participant's right forehead above the eyebrow with an aperture of 4.2 cm in diameter and a period of 8 min. A sham experiment was performed with the laser device turned on but set to 0.1 W also for 8 min, while the laser aperture was covered with a black-colour cap. A power meter was used to confirm that the output power in the presence of the cap was zero. Table 2.2 lists the light irradiance (W/cm^2), light fluence (J/cm^2), and total energy (dose) (J) delivered by the 8-min active and sham tPBM, respectively. The participants wore protective goggles throughout the experiment.

Table 2.2 Parameters for 8-min tPBM and sham by a 4.2-cm diameter laser at 1064 nm over the right eyebrow

Stimulation	Irradiance (W/cm^2)	Fluence (J/cm^2)	Total Dose (J)
tPBM	0.25	120	1662
sham	0	0	0

EEG data were collected during the entire experiment using a 64-channel EEG instrument (Biosemi, Netherlands). Each subject wore an EEG cap with 64 electrodes positioned according to the standard 10-10 EEG electrode placement [68]. Electrode gel (MFI Medical Equipment Inc., CA, USA) was used to increase the signal-to-noise ratio of the recorded EEG data. The recorded EEG time series were directed to a desktop computer using electrical cables.

The stimulation protocol (figure 2.1) consisted of a 2-min baseline (pre), an 8-min stimulation (active tPBM or sham), and a 3-min recovery (post) period. The EEG data were acquired at either 256 Hz or 512 Hz; all 512-Hz data were down-sampled to 256 Hz during data pre-processing. tPBM was delivered near electrodes FP2 and AF8 under either sham or active conditions.

The study was conducted in a single-blind crossover design, with each subject completing both sham and active tPBM experiments in a random order, with a minimum 5-day interval between the two experiments. All participants were asked whether they felt drowsy during the experiment and whether they noticed any heat sensations at the stimulation site.

2.2.3 Overview of data processing steps

Each of the recorded EEG datasets represented a 13-min time series of 64 channels during both the active and sham tPBM experiments for 45 participants (after exclusion of 4 subjects). Because the data processing and analysis procedures included multiple steps in this study, we outline a flow chart of these steps in figure 2.2 to better guide the reader through them easily. Briefly, there were five steps in data processing: (1) data pre-processing, (2) PSD-based power analysis to obtain frequency-specific power topography, (3) graphical edge formation based on the “imaginary part of coherence” analysis, (4) GTA-based analysis to quantify global connectivity metrics altered by tPBM, and (5) GTA-based analysis to identify local or nodal graphical metrics changed by tPBM in 10 cluster regions.

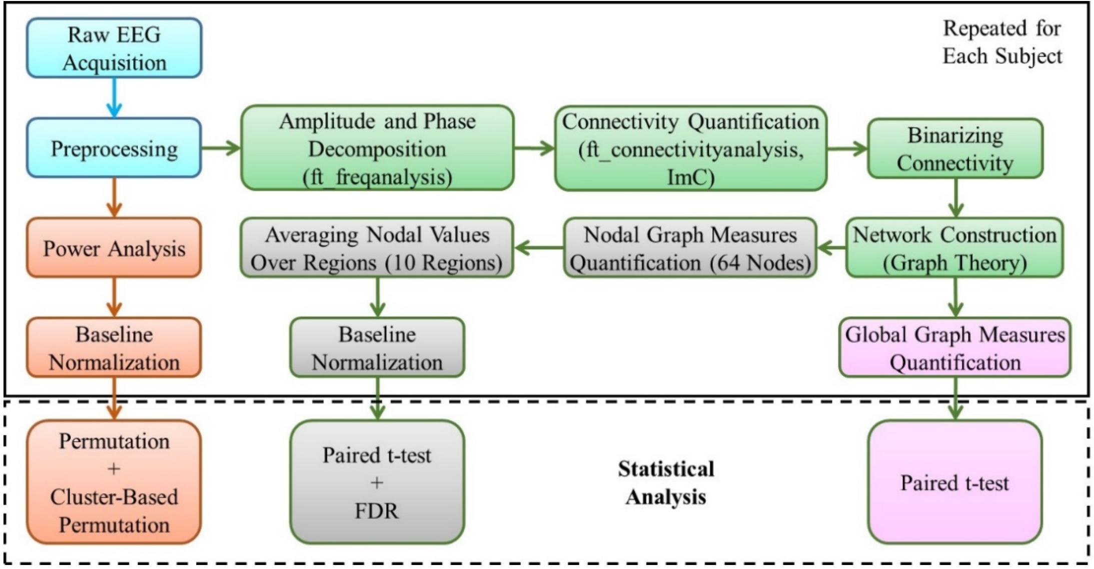

Figure 2. 2 A data processing flow chart, including steps for (1) data pre-processing (blue boxes), (2) PSD-based analysis and permutation tests to form power topographies (orange boxes), (3) graphical edge formation based on the “imaginary part of coherence” analysis, (4) GTA-based assessment for global graphical connectivity metrics (pink boxes), and (5) GTA-based assessment for nodal graphical connectivity metrics (gray boxes).

2.2.4 Data pre-processing for EEG time series

EEGLAB, an open-source software package based on MATLAB, was used to pre-process the EEG data. First, EEGLAB's "filtfilt" function was used to band-pass filter the 64-channel raw EEG data to ensure zero phase distortion of the time series, followed by a 60-Hz notch filter to eliminate line noise. Second, each EEG time series was re-referenced with respect to the voltage average over all the 64 channels. Next, robust PCA (rPCA) was applied to identify and remove significant signal artifacts and/or outliers from EEG signals [69, 70]. Finally, to further remove noise and artifacts [71, 72] such as eye movements, saccades, and jaw clenching, independent component analysis (ICA) [73, 74] was used.

To quantify the dose-dependent responses of EEG to tPBM/sham, each artifact-free time series was divided into four temporal sections: (1) the last minute of the 2-min baseline before the onset of active or sham stimulation (pre), (2) the first 4-min stimulation period (Stim1), (3) the second 4-min stimulation period (Stim2), and (4) the first 2-min recovery (post). The pre-processed data were then used for both PSD analysis and GTA-based assessment of graphical metrics during each temporal segment.

2.2.5 EEG power spectral density and changes in power

With the use of the "Pwelch" function (with a 4-sec window and 75% overlap [75]) in EEGLAB, a PSD curve of artifact-free time series for each EEG channel in each time section was calculated. The frequency-specific PSD bandwidths were then selected to cover the delta (1-4 Hz), theta (4-8 Hz), alpha (8-13 Hz), beta (13-30 Hz), and gamma (30-70 Hz) bands. Next, the mean power change at each of the five frequency bands, f, $\Delta mPower^f$, during each of the three temporal segments (Stim1, Stim2, and post) was normalized to the last minute of its respective baseline (pre), as expressed below [27]:

$$\Delta mPower_i^{\,f} = \frac{PSD^f{}_i - PSD^f{}_{pre}}{PSD^f{}_{pre}} \times 100\% = \frac{\left(PSD^f{}_i - PSD^f{}_{pre}\right) \times f_{band}}{PSD^f{}_{pre} \times f_{band}} \times 100\%$$

$$= \frac{Power^f{}_i - Power^f{}_{pre}}{Power^f{}_{pre}} \times 100\%. \qquad (2-1)$$

where superscript "*f*" denotes the five frequency bands, subscript "*i*" represents the three temporal segments (Stim1, Stim2, or post), subscript "*pre*" represents the baseline segment, f_{band} denotes the bandwidth of a chosen frequency band for PSD calculations, and PSD_i and PSD_{pre} indicate bandwidth-averaged PSD values. Note that *ΔmPower* is a relative value or percentage change in bandwidth-averaged power caused by tPBM or sham treatment (see the first two orange boxes in figure 2.2). To illustrate the difference in *ΔmPower* between the two conditions, we further calculated the sham-subtracted (*ss*) and tPBM-induced change in power ($\Delta mPower_{ss}$) at each electrode for each of the five frequency bands within each of the three temporal periods:

$$\Delta mPower_{ss-i}^{f} = \Delta mPower_{tPBM-i}^{f} - \Delta mPower_{sham-i}^{f}. \qquad (2-2)$$

2.2.6 Statistical analysis for EEG power topography

Because EEG data taken at neighbouring time points and spatial channels are highly correlated, it is necessary to perform advanced statistical analysis to remove such correlations and for multi-variable comparisons. For this purpose, we utilized several functions (including "ft_freqstatistics") available in the FieldTrip toolbox [76, 77] to perform cluster-based permutation tests for statistical comparisons of changes in the EEG power (i.e., $\Delta mPower_{ss}{}^{f}$ as shown in Eq. (2-2)) among the 64 electrodes in each of the five frequency bands within each of the three temporal periods. In principle, cluster-based permutation tests have two components: The first is the cluster-forming algorithm, which converts one high-dimensional observation into a quantifiable summary of its cluster structure. The second one creates a surrogate null distribution, against which the observed data is compared to obtain p-values [78].

Following this method, we first grouped electrodes as clusters within a given scalp distance (e.g., 4-5 cm), followed by identification of the EEG channels whose $\Delta mPower_{ss}{}^{f}$ values were significantly different from zero based on parametric or non-parametric testing for each electrode at a significance level of 0.05. Second, a statistical evaluation was performed by taking the sum of the t-values over each cluster. Third, the summed t-value was compared to a null distribution. The null distribution for both permutation tests and cluster-based correction was obtained by randomly permuting $\Delta mPower_{ss}^{f}$ values 1000 times. (see the last orange box in figure 2.)

2.2.7 Amplitude and phase decomposition of EEG signal

For GTA-based connectivity quantification, we determined the edges or links of a graphical network between all pairs of EEG electrodes. Based on the mathematical definition of the graphical connectivity measure, the correlation between the phases or amplitudes of these EEG channels can be interpreted as the functional connectivity between these points [13, 14]. Thus, we performed amplitude and phase decompositions of the time series for all 64 channels. The amplitude and phase of an EEG time point can be represented as a complex number [13, 15]. Moreover, multitaper power spectral density estimation is a well-known method for extracting spectral information from time series [79, 80]. In this study, we utilized multiple tapers, namely, Slepian sequences, to taper the EEG signal in the time domain before performing the Fourier transform. This part of the calculation was conducted using the “ft_freqanalysis” function within the FieldTrip toolbox to generate a complex time series [76].

2.2.8 Imaginary part of coherence as EEG connectivity measure

Coherence, a widely used connectivity measure, is a frequency-domain function equivalent to the time-domain cross-correlation function. The coherence coefficient is a normalized quantity between 0 and 1, and is computed mathematically for the frequency of ω as follows [13]:

$$coh_{xy}(\omega) = \frac{|S_{xy}(\omega)|}{\sqrt{S_{xx}(\omega)S_{yy}(\omega)}} = \frac{\left|A_x(\omega)A_y(\omega)e^{i(\varphi_x(\omega)-\varphi_y(\omega))}\right|}{\sqrt{A_x^2(\omega)A_y^2(\omega)}}\,, \qquad \text{(2-3)}$$

where S_{xx}, S_{yy} denote the power estimates of signals x and y, and S_{xy} represents the averaged cross-spectral density term of the two signals. In addition, A and φ are amplitude and phase of the signals obtained from multitaper method.

The main drawback of using coherence in sensor space, especially in high-density EEG, is the effect of volume conduction. In general, signals generated in one region of the brain can be detected by several electrodes because of the high electrical conductivity of the brain, which leads to an artificially high coherence value among these channels. To negate this effect, the numerator of equation (2-3) is set to zero when the phase difference between x and y signals is 0 or π. This method is called the 'imaginary part of coherence', which explicitly removes instantaneous interactions that are potentially spurious owing to volume conduction [13]. A study has shown that the imaginary part of coherence allows for excellent detection of brain interaction from rhythmic EEG data [81].

The pairwise connectivity values for all pairs of electrodes (64 in this study) can be represented in an n×n (i.e., 64 × 64) adjacency matrix, where n is the number of nodes (i.e., 64 channels). The FieldTrip toolbox facilitates the computation of the imaginary part of coherence for all pairs of channels using the "ft_connectivityanalysis' (see the first two green boxes in figure 2).

Each temporal segment was divided into 10-second epochs (i.e., 6 epochs per min), and the adjacency matrices generated for all epochs in each frequency band were averaged for each of the three temporal segments and five frequency bands for each subject individually. These averaged matrices were then binarized by varying the sparsity level and used for further GTA-derived global and nodal connectivity analysis as described in the following sections.

2.2.9 Global and nodal graphical metrics selected for GTA

Graph theory analysis enables researchers to explore topological changes in brain networks through pair-wise functional connectivity between channels (nodes). A network and its regions can be characterized based on three main measures: functional segregation, functional integration, and centrality. A couple of previous studies have shown tPBM-induced alterations in global connectivity and graph measures of the brain network with different setups and protocols [29, 30]. However, these studies focused only on the residual modulation in post stimulation with a lower spatial EEG electrode placement (i.e., 19 channels).

In this study, we utilized GRETNA [82], a widely used GTA toolbox, to quantify the global and nodal graphical metrics of the human brain network for individual subjects under both active and sham tPBM in four temporal segments and five frequency bands. This step was repeated 19 times to assess the respective values of the chosen metrics under a sparsity range from 5% to 95% with an increment of 5% (see the last two green boxes in figure 2.2).

To examine tPBM-induced effects, five global graphical measures were chosen for the analysis: synchronization (*S*), global efficiency (*GE*), small-worldness (*SW*), rich-club, and assortativity. However, no significant difference was observed between tPM and sham groups in rich-club and assortativity. The group-level values (averaged over 45 subjects) for each global measure at each sparsity level were statistically compared between the active tPBM and sham conditions using a paired t-test (see the pink boxes in figure 2.2).

As noted in the Introduction, two publications reported tPBM-induced modulations of the GTA-derived brain network [29, 30]. However, they showed alterations only in global network metrics [29] and within each hemisphere or between two hemispheres [30], respectively. In this study, we aimed to detect the ability of tPBM to neural-modulate regional or local brain connectivity, based on 64-channel EEG measurements. Accordingly, our analysis gave rise to five nodal graphical metrics, namely, nodal clustering coefficient (*nCC*), nodal efficiency (*nE*), nodal local efficiency (*nLE)*, betweenness centrality (*BC*), and degree centrality (*DC*), which were significantly altered by tPBM across different clusters on the human scalp. It is worth noting that another nodal metric, i.e., shortest path length, was evaluated and no statistically significant difference was observed in comparison between sham and tPBM groups. The definitions or explanations of the three global and five local graph metrics are listed in Table A1 in the Appendix.

2.10 Topographical clusters for nodal connectivity

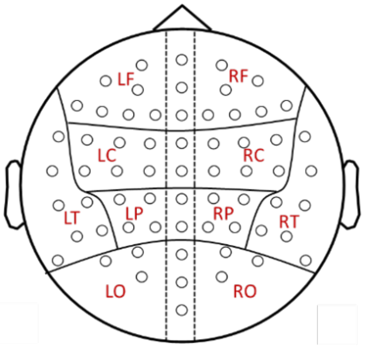

Figure 2. 3 A layout of 10 clusters for the 64 EEG electrodes. Circles represent electrodes; lines separate different clusters. The 10 medial electrodes are grouped in both left and right regions; the overlapped regions are marked by the two dashed lines. LF: Left frontal; RF: Right frontal; LC: Left central; RC: Right central; LP: Left parietal; RP: Right parietal; LT: Left temporal; RT: Right temporal; LO: Left occipital; RO: Right occipital.

Although GTA was performed on the 64-channel EEG, resulting in quantitative changes in nodal network metrics, the 64 EEG nodal locations were too dispersed to locate or identify cortical and anatomical regions on the human scalp. Thus, we focused on 10 nodal/local sections according to several key cortical areas of the human brain, namely the prefrontal, central, temporal, parietal, and occipital regions [83]. Therefore, 64 nodes (i.e., EEG channels) were divided into 10 clusters based on their locations in the brain topography, with an average of 6-10 electrodes in each cluster. Figure 2.3 illustrates the topographical clusters of EEG electrodes. The 10 medial electrodes were grouped twice in both the left and right clusters (see the first two right gray boxes in figure 2.2).

At the subject level, each nodal graphical metric within each cluster area was obtained by averaging the specific metric over all electrodes within the respective region (for each of the three temporal segments and five frequency bands). To compare the changes induced by tPBM vs. sham, nodal measures for each temporal segment were baseline-normalized by subtracting the corresponding baseline (pre) values from those in each of the three subsequent time windows (Stim1, Stim2, and post). Next, for each cluster region, group-level (n=45) and baseline-subtracted nodal metric values were compared between the active and sham conditions using paired t tests. To correct for multiple comparisons, false discovery rate (FDR) correction was performed for 10 regions with a corrected significance level of 0.05, as shown in the last two gray boxes in figure 2.2.

In summary, figure 2.2 outlines the processing procedures, where the first two blue boxes show the common pre-processing steps. The three orange blocks and arrows denote the power spectral analysis at the subject and group levels. The four green boxes represent the connectivity analysis and lead to two separate outputs: the global and nodal connectivity measures. All analysis steps, except statistical analysis, were applied to individual subject datasets, followed by statistical analysis as the last step performed at the group level.

2.3 Results

The EEG signals from 45 subjects in three temporal segments (Stim1, Stim2, and post) were analysed for both active and sham stimulation cases. The respective results are presented in the following three sub-sections: First, baseline-normalized, sham-subtracted topographies were obtained, illustrating significant differences in topographical EEG powers ($\Delta mPower_{SS}$) between the two experimental conditions in the respective frequency bands. Second, three global graphical metrics were derived from the GTA and between the active tPBM and sham treatments compared at the group level. Comparisons were made for all three temporal segments in the beta band only because tPBM significantly affected the chosen connectivity metrics of the beta rhythm. Finally, five nodal graphical metrics were characterized and presented using topographic maps. Thus, we revealed how the segregation, integration, and centrality of each cluster/region were significantly altered by tPBM at the group level. Similar to the global metrics case, it was only in the beta band that tPBM significantly altered the local graphical metrics.

2.3.1 Topographic changes in power between tPBM and sham stimulations

As shown in figure 2.2 and described in Sections 2.2.5 and 2.2.6, the baseline-normalized values of $\Delta mPower^f$ (see eq. (2-1)) for each group of tPBM and sham conditions among the three temporal segments (Stim1, Stim2, and post) and five frequency bands were calculated. Group-level statistical comparison to the baseline for each stimulation case was performed using a permutation test for each of the three temporal periods and five frequency bands, resulting in respective group-

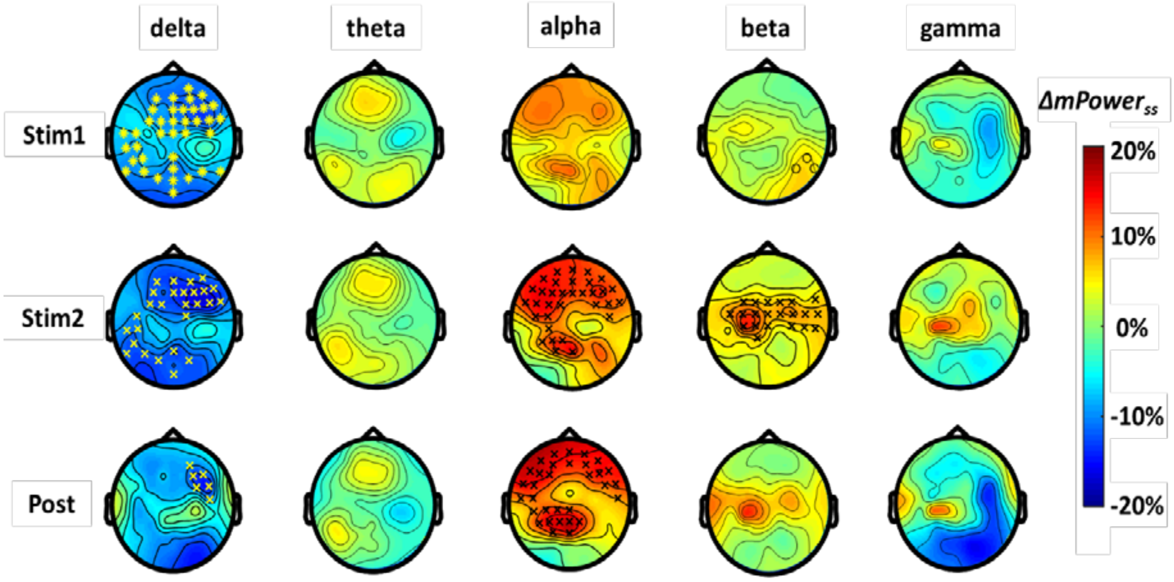

Figure 2.4 Topographic maps of group-averaged (n=45), baseline-normalized, and sham-subtracted changes in ΔmPowerss (see eq. (2-2)) in delta (1-4 Hz), theta (4-8 Hz), alpha (8-13 Hz), beta (13-30 Hz), and gamma (30-70 Hz) bands during the first 4 minutes of tPBM (Stim1), second 4 minutes of tPBM (Stim2), and post tPBM period. Also, statistical results after the cluster-based permutation testing are superimposed in each topographical map, showing significant differences in ΔmPower between the tPBM and sham stimulations during respective three time segments and in five frequency bands with corrected significance levels of $p < 0.05$ (×) and $p < 0.01$ (*).

level topographies (n=45). However, to show clear statistical differences in $\Delta mPower^f$ between the two stimulation conditions, baseline-normalized and sham-subtracted topographical maps of $\Delta mPower_{ss}^f$ (%) values (see Eq. (2-2)) over 64 channels were achieved, as shown in figure 2.4 for all five frequency bands. In addition, after the cluster-based permutation testing for 64-channel statistical comparison, the electrode sites/clusters that were significantly affected by tPBM are superimposed on the topographies in figure 2.4 with '*' denoting $p<0.01$ and '×' denoting $p<0.05$.

These results illustrate a significant, dose-dependent increase in EEG rhythm powers at alpha (8-13 Hz) and beta (13-30 Hz) during the last 4 min of tPBM (i.e., Stim2). Specifically, the increase in alpha $\Delta mPower_{ss}$ was shown as two major clusters of channels in the bilateral frontal and left parietal-occipital regions, whereas the increase in beta $\Delta mPower_{ss}$ was mainly seen as one cluster of electrodes in the central/parietal region of the scalp. The enhanced alpha $\Delta mPower_{ss}$ remained in the affected locations during the post-tPBM period, whereas significant increase in beta $\Delta mPower_{ss}$ ceased during the recovery time. Furthermore, delta power was reduced in the frontal, left temporal, and occipital regions during tPBM, and in the right frontal region during recovery.

2.3.2 Global graphical metrics of functional connectivity altered by tPBM

Following the steps given in Sections 2.2.7-2.2.9, adjacency matrices for all three temporal segments and five frequency bands were generated. These matrices were further binarized for different sparsity values, resulting in the GTA-derived graphical networks. In this study, we identified three global network metrics (*S*, *GE*, and *SW*) that were significantly altered by tPBM with respect to the sham condition and only in the beta band. As shown in figure 2.5, the three rows illustrate the respective global metrics during Stim1, Stim2, and the post-period under both active and sham stimulation. The grey bars in each panel of figure 2.5 highlight the sparsity values at which the corresponding graphical metrics were altered significantly by tPBM based on paired t-tests ($p < 0.05$).

These results suggest that tPBM significantly reduces the global synchronization, global efficiency, and small-worldness of the network connectivity of the human brain. Specifically, significant decreases in synchronization and global efficiency is observed during Stim1 and the recovery period with more sparsity values, while a significant reduction in small-worldness appeared in Stim2 with more sparsity units. Additionally, we confirmed that there was no significant difference between the pre-stimulation baselines under tPBM and sham stimulation for any of the three global network metrics.

2.3.3 Nodal graphical metrics of functional connectivity altered by tPBM

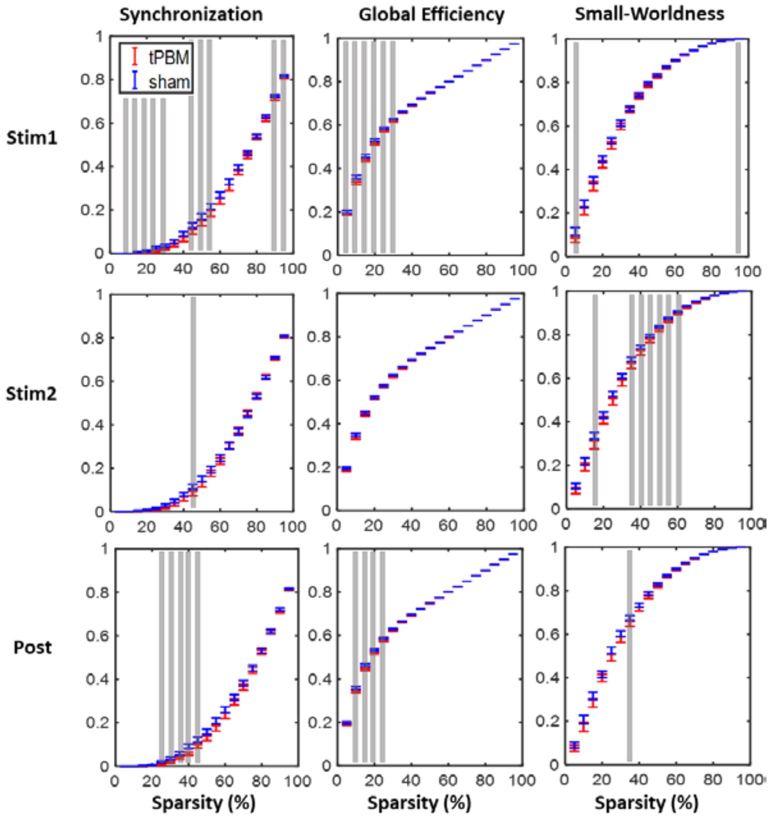

Figure 2.5 Three GTA-derived global graphical metrics, namely, synchronization (the 1st column), global efficiency (the 2nd column), and small-worldness (the 3rd column), of the EEG brain network in the beta band (13-30 Hz) under both active tPBM and sham stimulation during Stim1 (the 1st row), Stim2 (the 2nd row), and the post period (the 3rd row). In each panel, the y axis denotes respective metric values while the x axis presents sparsity values with an increment of 5%. The grey bars mark sparsity values at which the corresponding graphical metrics were altered significantly by tPBM with respect to sham based on paired t-tests ($p < 0.05$). Error bars represent standard error of the mean.

After performing the analysis steps given in Sections 2.2.9, cluster-averaged, baseline-subtracted values for each of the five nodal graphical metrics (i.e., *nCC*, *nE*, *nLE*, *BC*, and *DC*) were obtained for each of the 10 spatial clusters (figure 2.3) under both tPBM and sham conditions. Next, after performing paired t-tests with FDR correction for 10 spatial clusters (i.e., $p < 0.05$, FDR corrected), we identified or categorized the clusters whose nodal metric values were significantly altered (i.e., increased or decreased) by tPBM for each of the five metrics at all three temporal periods, and only in the beta rhythm band. The topographical representations of the results for the five nodal metrics are shown in figure 2.6.

Based on figure 2.6, we made the following observations. (1) During Stim1, significant increases in nodal efficiency, betweenness centrality, and degree centrality occurred in the right frontal region near the tPBM stimulation site. (2) During Stim2 and post stimulation, significant changes occurred in the bilateral frontal regions for all five nodal metrics. More specifically, tPBM significantly decreased the clustering coefficient and nodal local efficiency while the stimulation significantly increased the other three nodal metrics. (3) Combined temporal and spatial results revealed that both nodal efficiency and degree centrality were initially enhanced by tPBM in the right frontal region during Stim1, followed by expansion of this enhancement to the contralateral side during Stim2, which remained during the post-tPBM period. (4) In the case of betweenness centrality, unilateral enhancement in the right frontal region remained during the entire stimulation time (i.e., Stim1 and Stim2) and then expanded to the contralateral side in the post. (5) On the other hand, during Stim2 and post stimulation, significant decreases occurred in the bilateral frontal regions for the nodal clustering coefficient (*nCC*) and nodal local efficiency (*nLE*). (6) During the same time periods for the same two metrics (*nCC* and *nLE*), decreases occurred in the left parietal and occipital regions. (7) Moreover, the left temporal region showed a reduction in nodal efficiency and betweenness centrality only for Stim2. (8) The only significant modulation in the right occipital region was a decrease in betweenness centrality in Stim2.

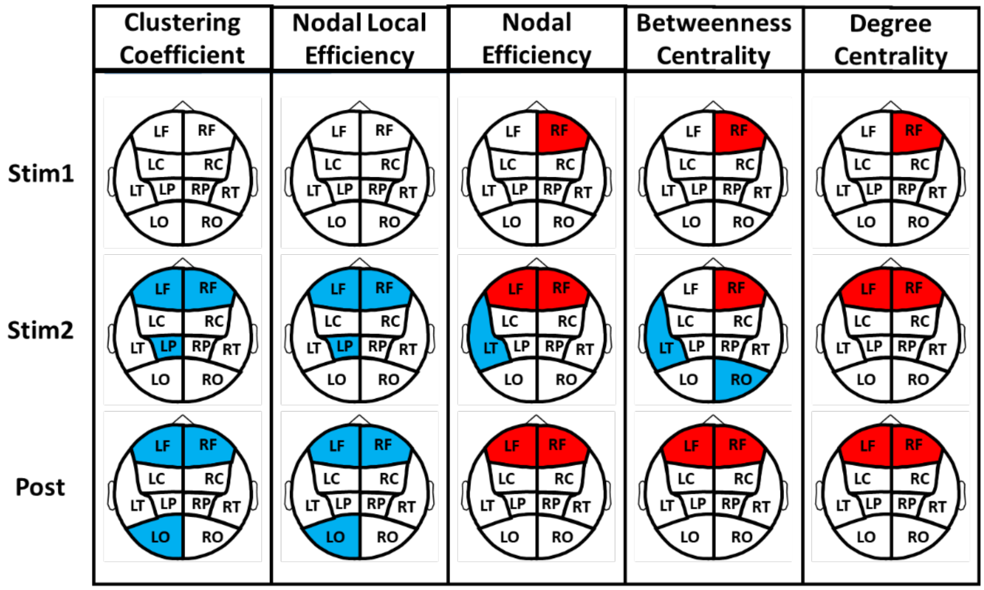

Figure 2.6 Comparative topographical maps of 10-Cluster-distributed nodal network metrics at the beta band (13-30 Hz). The comparison was made between tPBM and sham stimulation conditions for each of the five nodal metrics, namely, the clustering coefficient (the 1st column), nodal local efficiency (the 2nd column), nodal efficiency (the 3rd column), betweenness centrality (the 4th column), and degree centrality (the 5th column) of the EEG brain network during Stim1 (the 1st row), Stim2 (the 2nd row), and the post period (the 3rd row). LF: Left frontal, RF: Right frontal, LC: Left central, RC: Right central, LP: Left parietal, RP: Right parietal, LT: Left temporal, RT: Right temporal, LO: Left occipital, RO: Right occipital. Red color represents tPBM > sham; blue color indicates tPBM < sham with $p < 0.05$ (FDR corrected).

2.4 Discussion

In Section 2.3, we identified and showed the clusters and regions on the scalp where tPBM modulated EEG oscillation powers and GTA-based EEG beta network connectivity. All these observations provided a better topographical overview of tPBM-induced electrophysiological effects on brain functional connectivity in the resting state. In this section, we will further interpret and discuss our observations, compare our results with previous studies, and associate the neurophysiological changes in different brain regions with behavioural improvement by tPBM that have been reported by others [2-6, 46, 54, 84].

As shown in figure 2.4, under the eyes-closed resting-state condition, tPBM significantly increased the power of alpha oscillations in clusters over the bilateral frontal, left parietal, and left occipital regions, as well as the beta power over the bilateral central and parietal regions during the second 4-min of stimulation. These observations agree with previous reports on eyes-open tPBM experiments [85, 86]. Moreover, tPBM significantly decreased the delta power during stimulation, followed by a residue of reduced power over a smaller region during recovery.

2.4.1 tPBM-induced alterations on EEG *ΔmPower* in clusters of electrodes in frontoparietal network

A significant increase in alpha power over frontal-parietal regions confirmed the ability of tPBM to neurally modulate the frontoparietal network, which is an executive network facilitating rapid instantiation of new tasks [87]. According to previous studies, alpha rhythm is thought to be associated with awareness [88] and cognitive functions, such as memory encoding and attention [89-91]. The same experimental protocol with a 1064-nm laser has been used previously, demonstrating a significant improvement in cognitive performance in human participants [2-4, 46, 84]. Moreover, the presence of stronger beta waves has been linked to better cognitive abilities, as reported in several studies [92, 93]. Thus, the beneficial outcome in human cognition by frontal tPBM can be, at least partially, attributed to its significant modulation of electrophysiological alpha and beta powers in the frontoparietal network. Regarding the reduction in delta power in the channel clusters during the stimulation period, we interpreted this observation as a result of the mild thermal sensation of the laser on the superficial tissue [27].

2.4.2 tPBM-induced alterations in global measures of functional network in beta band

As shown in figure 2.5, tPBM significantly changed three global graph measures, namely, synchronization, global efficiency, and small-worldness, in the beta wave only. We discuss each of these changes as follows:

Our observation that brain network synchronization in the beta band was significantly reduced during Stim1 and recovery agrees with a recent study that reported the effects of tPBM on brain network synchronization with 850 nm LEDs [30]. In addition, a behavioural study attributed a decrease in synchronization in the healthy human brain to awareness and cognitive processing [94]. Thus, the outcome and effect of tPBM on desynchronizing EEG beta waves may be associated with cognitive processing.

Similarly, the global efficiency of the brain network was significantly reduced by tPBM compared to sham during Stim1 and post. This reduction indicates a decrease in brain network integration, which may imply less efficient or more complex information paths in the network. In other words, from a global point of view, tPBM may increase the energy and wiring costs of the information flow owing to the trade-off between network efficiency, energy, and wiring costs [95, 96]. This could be an indicator of increased brain complexity, which is related to higher cognitive function [97]. This observation indirectly supports the expected benefit of tPBM, namely, the beneficial effects of tPBM on cognitive improvement.

It is known that small-worldness is dependent on the global integration and segregation of the network and is calculated as the ratio of normalized integration to normalized segregation [65]. Thus, the reduction in this metric could be attributed to a significant reduction in global integration (as reflected by a reduction in *GE*) and/or a significant increase in the global segregation of the brain network caused by tPBM. These observed significant effects of tPBM on small-worldness taking place only in Stim2 could result from the resistance of resting-state networks against changes in network composition, as well as the dose-dependent nature of tPBM-induced effects on neural activity [98, 99]. However, a possible explanation for the lack of significant alteration in synchronization and global efficiency in Stim2 could be the high variability in the functional topography of the frontoparietal network [87].

In summary, significant decreases in synchronization, global efficiency, and small-worldness can be associated with potential increases in the complexity of the brain network and the improvement or enhancement of human cognitive function [94, 97]. In addition, the observation that tPBM altered only beta-wave oscillations in the EEG graphical network was in agreement with other studies [30, 64]. Several publications have shown the role of the beta band in different brain networks [100] and cognitive functions [101, 102].

2.4.3 tPBM-induced alterations in nodal graphical measures in beta band

Figure 2.6 shows how tPBM would alter nodal connectivity of the functional brain network in the beta band in healthy participants. Specifically, this figure illustrates that nodal clustering coefficient and nodal local efficiency, as measures of segregation of the brain network [103], were reduced significantly in bilateral frontal regions in Stim2 and post. Furthermore, these two segregation nodal metrics were decreased in the left parietal and left occipital regions during Stim2 and post, respectively. All these observations implied that the clusters of nodes in these regions of the network became less segregated during the 2nd 4-min and post period of tPBM. In other words, tPBM facilitated less separation and more integration of nodal graphical connectivity.

Consistent with the aforementioned observation, nodal efficiency, which reflects nodal integration, increased in the right frontal region during the first 4 min of tPBM. This increase indicates enhanced integrity of the nodes over this region in the information flow [103] and parallel information transfer. Furthermore, during the last 4 min of tPBM, the bilateral frontal regions showed an increase in integration into the functional network, while the integrity of the left temporal region in the network was significantly reduced. This phenomenon implies that the tPBM stimulated more network integration at the beta rhythm in the frontal regions, with the cost of reducing network integration in the left temporal segment/cluster.

Betweenness centrality represents the fraction of all shortest paths in the network that pass through a particular central node [104]. A large value of betweenness centrality denotes a large impact of this central node on the information flow over the entire network. It is common for nodes at intersections of disparate parts of the network to have a high betweenness centrality [65]. It is clear from figure 2.6 that betweenness centrality increased in the right frontal region during Stim1 and Stim2. Similar changes in the frontal and temporal regions of beta waves have been reported during cognitive training [101]. After stimulation, the effects of tPBM on betweenness centrality remained bilateral in the frontal regions. These observations suggest that the frontal regions, especially the right frontal region under tPBM, became more prominent in connecting the disparate parts of the network throughout the stimulation and recovery periods.

The last nodal measure investigated was degree centrality, which quantifies the number of links from nodes in a specific region to other nodes in the same region or other regions [65]. An increase in this nodal metric was observed in the right frontal region during all three temporal segments and in the left frontal region during Stim2 and Post. The enhancement of this nodal parameter revealed that these cortical/brain regions could be prominently stimulated by tPBM for more information connections or links at beta wave oscillations. It has also been reported that a working memory task during the encoding phase triggers similar increases in degree centrality over the frontal regions of the beta band [102].

Combining all these observations, we concluded that tPBM facilitated a reduction in local segregation, increases in nodal integration and centrality of frontal regions, and the growth of connection links between nodes in these frontal regions compared to other regions. These results are in agreement with the observed changes in the flow of information reported in a tPBM-evoked causal connectivity study [105].

2.4.4 The role of the beta band in tPBM-induced network modulation and its relation to enhancement of human cognition

The alpha and beta powers of the human brain, especially in the frontoparietal network, are believed to be related to cognitive functions, such as memory encoding and attention [89-91], especially in the frontal, temporal, and parietal regions. Our observations (as presented in Section 2.3.1) clearly demonstrated that tPBM enabled increases in the alpha and beta powers in the frontal-central-parietal regions, indicating the underlying association between tPBM and enhancement of human memory.

However, our results in Sections 2.3.2 and 2.3.3 showed that tPBM altered EEG graphical network metrics only in the beta band, which was consistent with the results given in ref. [30]. Thus, an implication of the relationship between prefrontal tPBM and its effects on EEG beta-wave network metrics was sought. Regarding the beta rhythm in the prefrontal cortex (PFC), "increased beta appears at the end of a trial when working memory information needs to be erased. A similar 'clear-out' function might apply during the stopping of action and the stopping of long-term memory retrieval (stopping thoughts), where increased prefrontal beta is also observed. A different apparent role for beta in the PFC occurs during the delay period of working memory tasks: it might serve to maintain the current content and/or to prevent interference from distraction. [100]" Accordingly, beta oscillations in the prefrontal region appear to serve as short-term memory executors and focus enhancers during executable tasks. In addition, the beta rhythm in the temporal lobe plays an important role in long-term memory retrieval [106]. Memory retrieval starts in the temporal lobe, passes through different parts of the neocortex, and stops in the prefrontal cortex [100]. There is always a balance in information flow in this order, even during the resting state.

Accordingly, we speculated that tPBM enables to significant neuromodulation of beta oscillations and the corresponding network connectivity globally across the scalp and regionally in several nodal/cluster regions. The significant modulation by tPBM on beta-wave connectivity in the human brain may be an underlying electrophysiological mechanism and association between tPBM and the enhancement of human cognition.

2.4.5 Comparisons to two other publications

As shown in Table 2.1, only two recent papers have reported tPBM-induced modulations of global network metrics [29] and alterations in brain connectivity between the two hemispheres [30]. It would be helpful to compare the altered graphical metrics provided in these two articles with those found in this study. Tables 2.3 and 2.4 below summarize and compare the global and local graphical metrics of the three studies, respectively.

Upon inspection of the global metrics of the network, Table 2.3 reveals that only global efficiency was altered by tPBM in all three cases, regardless of stimulation conditions. However, a more consistent agreement exists between Ref. [30] and this study with network alterations in the beta band. On the other hand, Ref. [29] showed increases in GE in the alpha and gamma bands under 40-Hz tPBM, which should result in alterations of the gamma waves (30-70 Hz).

Table 2.3 Comparisons of global graphical metrics among three studies

	CC	***Characteristic path length***	***GE***	***LE***	***Energy***	***Entropy***	***S***	***SW***
Ref. [29] (810-nm LED, 40 Hz; DMN)	increase (alpha & gamma)	increase (alpha & gamma)	increase (alpha & gamma)	increase (alpha & gamma)	-	-	-	-
Ref. [30] (850-nm LED, CW; PFC)	Decrease (beta)	-	Decrease (beta)	Decrease (beta)	Decrease (beta)	Increase (beta)	-	-
This Study (1064-nm Laser, CW; PFC)	-	-	Decrease (beta)	-	-	-	Decrease (beta)	Decrease (beta)

Table 2.4 lists several nodal network metrics for comparison with Ref. [30] and this study, because Ref. [29] did not provide results on tPBM-altered nodal metrics. Both studies observed consistent tPBM-induced alterations in beta wave connectivity between the two hemispheres [30] or in the prefrontal regions (in this study), whereas the modulated network metrics were different.

Table 2.4 Comparisons of nodal graphical metrics among three studies

	tPBM duration	***Radius of light size***	***nCC***	***nE***	***nLE***	***Eigenvector Centrality***	***BC***	***DC***
Ref. [30] (850-nm LED, CW; PFC)	2.5 min	0.67 cm	-	-	-	Yes; (beta; between two hemispheres)	-	-
This Study (1064-nm Laser, CW; PFC)	8 min	2.1 cm	Yes; (beta; frontal)	Yes; (beta; frontal)	Yes; (beta; frontal)	-	Yes; (beta; frontal)	Yes; (beta; frontal)

Such differences could be accounted for by several experimental setting parameters, including wavelengths (850 nm vs. 1064 nm), light type (LEDs vs. laser), stimulation size on the forehead (0.67 cm vs. 2.1 cm), stimulation duration (2.5 min versus 8 min) of the tPBM. We observed that the right forehead tPBM using a 1064-nm laser with larger stimulation size and longer duration created significant stimulations and alterations in nodal brain connectivity metrics, particularly in the prefrontal regions, near the stimulation site.

2.4.6 Limitations and future work

First, the international 10–10 electrode placement system in this study was not strictly followed on the human head because a clear area with 4.2 cm in diameter was needed for tPBM light delivery on the right forehead. The EEG cap was shifted 1–2 cm backward. There was a systematic shift in the electrode locations given in Figs. 2.4 and 2.6 with respect to the standard 64-electrode locations. However, the precision of EEG channel locations is not affecting the final results significantly, since we focus on the global and regional/clustered effects of tPBM. This position precision is most important when the collected scalp EEG data is being back-projected to the brain to evaluate power and connectivity modulation in specific regions of brain. Second, the power spectral and connectivity analyses were performed in the sensor space. Source space analysis can be conducted to observe specific cortical and subcortical regions in the brain affected by tPBM. Third, the current study was based on EEG signals of the tPBM-treated human brain in the resting state without the evaluation of any behavioural assessment. It is highly desirable to obtain concurrent assessments of changes in brain connectivity metrics and cognitive enhancement after tPBM. A combination of electrophysiological and behavioural measures would provide more informative and comprehensive views of the correlation and association between functional connectivity and behavioural effects of tPBM. Overall, there are few publications in the literature on how tPBM affects brain connectivity and the association between tPBM-induced network changes and cognitive improvement. It is necessary to promote and conduct more investigations in this line of work to make tPBM a non-invasive, portable, and low-cost intervention tool for healing patients with certain brain disorders as well as for healthy aging in the rapidly growing aging population.

2.5 Conclusion

In this study, we utilized three analysis steps to identify the electrophysiological effects of tPBM in a healthy human brain. First, power spectral analysis revealed that alterations in EEG spectral powers were mainly present in the alpha and beta bands of the fronto-central-parietal regions. Second, a topological approach, GTA, facilitated findings on significant modulation of the EEG beta rhythm in the information path and enhancement of the brain network complexity at the global network level during and after the stimulation. Finally, assessment of the nodal measures of the network at the regional and cluster levels confirmed that tPBM had a major effect on the frontal and parietal clusters in the beta band. The information paths were enhanced during and post tPBM in the prefrontal regions near the stimulation site. Further studies are needed to better understand the relationship between tPBM-induced alteration of brain networks and improvement in human cognition if tPBM is to be developed as a useful tool for treating patients with brain disorders and for supporting healthy aging in the aging population worldwide.

Chapter 3

Prefrontal Cortical Connectivity and Coupling of Infraslow Oscillation in the Resting Human Brain:
A Two-Channel Broadband NIRS Study

Sadra Shahdadian, Xinlong Wang, Shu Kang, Caroline Carter, Akhil Chaudhari, Hanli Liu

(This chapter is a manuscript that has been accepted for publication in Cerebral Cortex Communications)

3.1 Introduction

3.1.1 Infra-slow Oscillation of the Human Brain

The human brain plays a major role in oxygen and glucose consumption despite its relatively low weight compared to other organs [107, 108]. The high levels of consumption are due to the high metabolic activity of neurons, which is modulated by the oxygenated blood supply and cerebral metabolism [109, 110]. Many studies have focused on investigating the mechanism of cerebral metabolic activity and have found vasomotion to be a major source of metabolic and hemodynamic modulations [31-35]. Vasomotion is a spontaneous oscillation that originates from the blood vessel wall with an infra-slow oscillation (ISO) of 0.005-0.2 Hz [36, 37]. In addition, a correlation is found between the ISO of cerebral metabolic activities and human cognitive functions [38]. Furthermore, vasomotion malfunction has been observed in older adults and in patients with different diseases, such as atherosclerosis [39], cardiovascular disease [40], and Alzheimer's disease [41]. Thus, it may be beneficial to quantify and characterize cerebral metabolism in the ISO range, which may provide better insight into neurophysiological mechanisms and discover features that differ between healthy humans and patients with brain disorders.

Relaxation-contraction cycles of blood vessel walls have been shown to be the driving force for the infra-slow rhythms of cerebral hemodynamic oscillations, independent of respiration and heartbeat [32, 111-113]. Three intrinsic frequency components of infra-slow cerebral hemodynamic rhythms have been found to correspond to the specific physiological and biochemical activities of the vascular wall layers [114]. These frequency bands consist of (1) endogenic (0.005-0.02 Hz), neurogenic (0.02-0.04 Hz), and (3) myogenic (0.04-0.2 Hz) [115-117] rhythms. The endogenic band corresponds to dilation-contraction cycles in the endothelial layer affected by the release of potent vasoactive factors, such as nitric oxide (NO), free radicals, prostacyclin, endothelium-derived hyperpolarizing factor, and endothelin [118, 119]. Oscillation in releasing vasoactive ions and neurotransmitters from neurons leads to modulation of the vessel dilation-contraction cycles in the neurogenic band [120]. Rhythmic myogenic activity, on the other hand, occurs as a result of the relaxation and contraction of vascular wall smooth muscle cells [117]. Such hemodynamic ISO can be detected by different measurement modalities, such as functional magnetic resonance imaging (fMRI) [121], transcranial cerebral doppler (TCD) [122], and functional near-infrared spectroscopy (fNIRS) [38]. However, these methods are not capable of concurrently monitoring the metabolic rhythms originating in the mitochondria. As mitochondria play a major role in cerebral metabolism and vasomotion, detecting mitochondrial activity and ISO is essential important [123].

3.1.2 Exploration of the Prefrontal Cortical Connectivity and Coupling of ISO

The bilateral prefrontal connectivity of the human brain with respect to certain neurophysiological functions reflects the level at which the lateral sides of the prefrontal cortex oscillate synchronously or coherently. Therefore, a higher level of connectivity represents a bilaterally or globally driven oscillation while a lower level of connectivity denotes locally driven activity [124]. On the other hand, unilateral hemodynamic-metabolic coupling indicates how the supply demand relationship between local oxygenated hemodynamics and metabolism is regulated. Any impaired, abnormal, or diminished bilateral connectivity and/or unilateral/local coupling of the prefrontal ISO could reflect or result from neurological diseases or brain disorders. This is because prefrontal cortex activity is closely associated with human cognition; many studies have provided evidence of correlations between prefrontal cortex activity and human cognition [125-129]. Thus, it is desirable to quantify prefrontal cortical connectivity and coupling of ISO in the human brain, which may be closely associated with normal or abnormal brain states, and may be developed for clinical applications in the near future.

3.1.3 Broadband Near-infrared Spectroscopy and Resting-State Analyses

Broadband Near-infrared spectroscopy (bbNIRS) has been investigated for more than 2 decades [130-134] and accepted as a reliable tool to quantify changes of oxygenated and deoxygenated hemoglobin concentrations ([HbO] and [HHb], respectively) as well as redox-state cytochrome-c-oxidase concentration ([CCO]) based on absorption and scattering of NIR light by these chromophores [131, 135, 136]. In particular, cytochrome-c-oxidase is the terminal enzyme in the mitochondrial respiratory chain that catalyzes the reduction of oxygen for energy metabolism [137-140]. Because redox CCO has a light absorption peak at ~800 nm, bbNIRS can quantify changes in [CCO] (Δ[CCO]) and enable us to reveal the metabolic state of a tissue [131, 135, 136]. However, since the concentration of CCO is much smaller than those of HbO and HHb in living tissues, accurate estimation of changes in [CCO] requires a multispectral approach [135, 136, 141]. In the past several years, our group has successfully quantified altered redox [CCO] in response to photobiomodulation using 1-channel or 2-channel bbNIRS (2-bbNIRS) taken on the human forearm or forehead [7, 9, 12, 142].

However, most studies in the field of either fNIRS or bb-NIRS are based on time-domain analyses and are often performed under task-evoked brain states [143-145]. Numerous articles on fNIRS-derived resting-state connectivity have been based only on hemodynamic (HbO) oscillations [146-148]. Little or no report could be found on the frequency-domain analysis of bb-NIRS measurements in the resting human brain. It is also unknown whether 2-bbNIRS can facilitate characterization of prefrontal connectivity and coupling in the brain.

In the present exploratory study [42], we hypothesized that 2-bbNIRS, along with frequency-domain analysis, enables us to quantify prefrontal cortical connectivity and coupling of ISO in the resting human brain. Specifically, the features analyzed from the 2-bbNIRS time series included (1) resting-state spectral amplitude (SA) of bilateral cortical hemodynamic and metabolic (i.e., SA_{HbO_i} and SA_{CCO_i}) activities, where i represents either the left or right prefrontal region, (2) bilateral hemodynamic connectivity ($bCON_{HbO}$), (3) bilateral metabolic connectivity ($bCON_{CCO}$), and (4) coupling between cerebral hemodynamic and metabolic activities on the unilateral side ($uCOP_{HbO\text{-}CCO\_i}$) of the prefrontal cortex over the three ISO frequency bands. By the end of this exploratory study, we would support this hypothesis by presenting relatively stable and consistent values for these features in healthy young humans, revealing the translation potential of these features for future clinical applications.

3.2 Materials and Methods

3.2.1 Participants

31 healthy human subjects were recruited from the local community at the University of Texas, Arlington. They were screened using the same inclusion criteria as those used in the previous studies [7, 9]. In summary, the inclusion criteria included: either sex, any ethnic background and in an age range of 18–40 years old. The exclusion criteria included: (1) diagnosed with a

psychiatric disorder, (2) history of a neurological condition, or severe brain injury, or violent behavior, (3) have ever been institutionalized/imprisoned, (4) current intake of any medicine or drug, or (5) currently pregnant. Each participant had five visits, separated by at least 7 days. Because of the high sensitivity of bbNIRS to motion artifacts, five subjects with excessive motion during one or more of the five experiments were excluded from the data. After exclusion, a total of 26 young and healthy humans (14 males and 12 females, mean ± SD age = 22.4 ± 2.3 years) participated in the 5-visit experiments. The study protocol complied with all applicable federal guidelines and was approved by the Institutional Review Board (IRB) of the University of Texas at Arlington. Informed consent was obtained from all participants.

3.2.2 Experiment Setup and Protocol

The data analyzed in this study were obtained from single-mode, resting-state, bilateral measurements with 2-channel bbNIRS, which is one of the dual-mode (i.e., bbNIRS and EEG) modalities. Specifically, a 2-channel bbNIRS probe (Figure 1(a)) was placed bilaterally on the forehead of the participants to acquire prefrontal ISO signals of Δ[HbO] and Δ[CCO] at rest. The 2-channel system consisted of two branches of a broadband white light source (Model 3900e, Illumination Technologies, NY, USA) and two CCD array spectrometers (QEPRO, Ocean Optics Inc., Orlando, FL, USA) as light detectors (Figure 3.1(b)). The two bbNIRS recording channels were positioned symmetrically on the subject’s forehead (visual judgement). Each channel consisted of one fiber bundle for light delivery to the forehead and another for backscattered light collection from the brain tissue, with a source-detector separation of 3 cm. A 2-channel probe holder was designed and 3D printed with a flexible material to ensure comfortable and firm attachment of the fiber bundles to the forehead skin, accommodating each participant’s forehead curvature. The probe holder was fastened to each participant's forehead with hook-and-loop fasteners, and adhesive medical tape was applied to the probe-skin interface to hold the probe on the forehead more steadily (without tightening the fastener too much), thus reducing motion artifacts.

Regarding the measurement protocol, after the consent form was signed, each participant was instructed to sit comfortably on a chair, followed by a dual-mode probe placement on the participant's head firmly. Then the 2-channel bbNIRS (and EEG) started to record data at a rate of 1.5 sec per temporal point (i.e., 0.67 Hz) during the 7-min resting state while the participant kept their eyes closed without falling asleep.

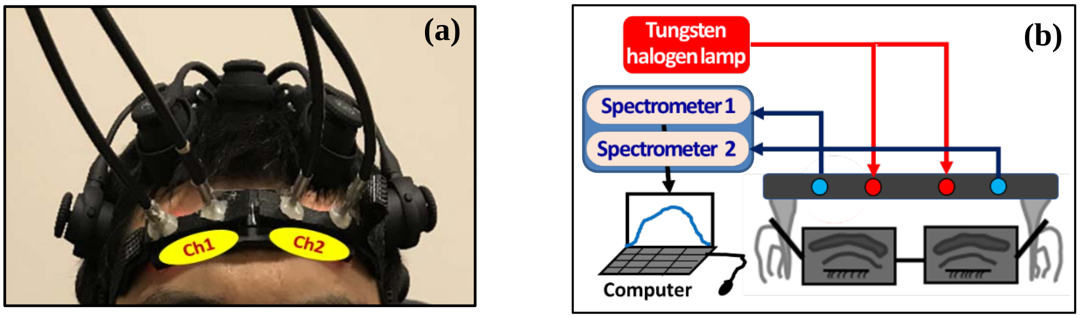

Figure 3. 1 (a) Dual-mode (bbNIRS and EEG) head probe setup, showing two separate channels with two sets of fiber bundles that were connected to (b) the 2-channel bbNIRS. While an EEG cap on the head is observable, the EEG data are not the topic/subject of this paper. The bbNIRS datasets used for this study were taken during 7-min eyes-closed conditions with the setup shown above.

3.2.2 Data Analysis

After 2-bbNIRS data acquisition, the data processing steps included both time- and frequency-domain analyses, as outlined in Figure 3.2, in five steps. Step 1 (blue boxes in Figure 3.2) was to obtain the Δ[HbO] and Δ[CCO] time series after converting the raw data to Δ[HbO] and Δ[CCO] at each time point. Step 2 (the yellow box in Figure 3.2) involved performing frequency-domain analysis using the multi-taper method that facilitated the following two steps to investigate the cerebral hemodynamic and metabolic ISO of the human prefrontal cortex in the resting state. Step

3 (the orange box) was to quantify spectral amplitudes of Δ[HbO] and Δ[CCO] (i.e., $\text{SA}_{\text{HbO\_}i}$ and $\text{SA}_{\text{CCO\_}i}$) in the endogenic, neurogenic, and myogenic (E/N/M) frequency bands measured on each lateral prefrontal site, where the subscript of "*i*" labels either "L" or "R" for the left or right forehead. Step 4 (green box) was used to perform coherence analysis and to determine (i) bilateral connectivity for Δ[HbO] and Δ[CCO] (i.e., bCON_{HbO} and bCON_{CCO}) of the human forehead and (ii) unilateral cerebral hemodynamic-metabolic coupling ($\text{uCOP}_{\text{HbO-CCO\_}i}$) for each lateral prefrontal cortex. Steps 1 – 4 were repeated for each of the 26 participants and then for five sets of measurements. Step 5: One-way ANOVA was performed to demonstrate no significant difference among the five measurements for each of the bilateral SA, bilateral connectivity, or unilateral coupling parameters (i.e., $\text{SA}_{\text{HbO\_}i}$, $\text{SA}_{\text{CCO\_}i}$, bCON_{HbO}, bCON_{CCO}, $\text{uCOP}_{\text{HbO-CCO\_}i}$) in each of the E/N/M bands.

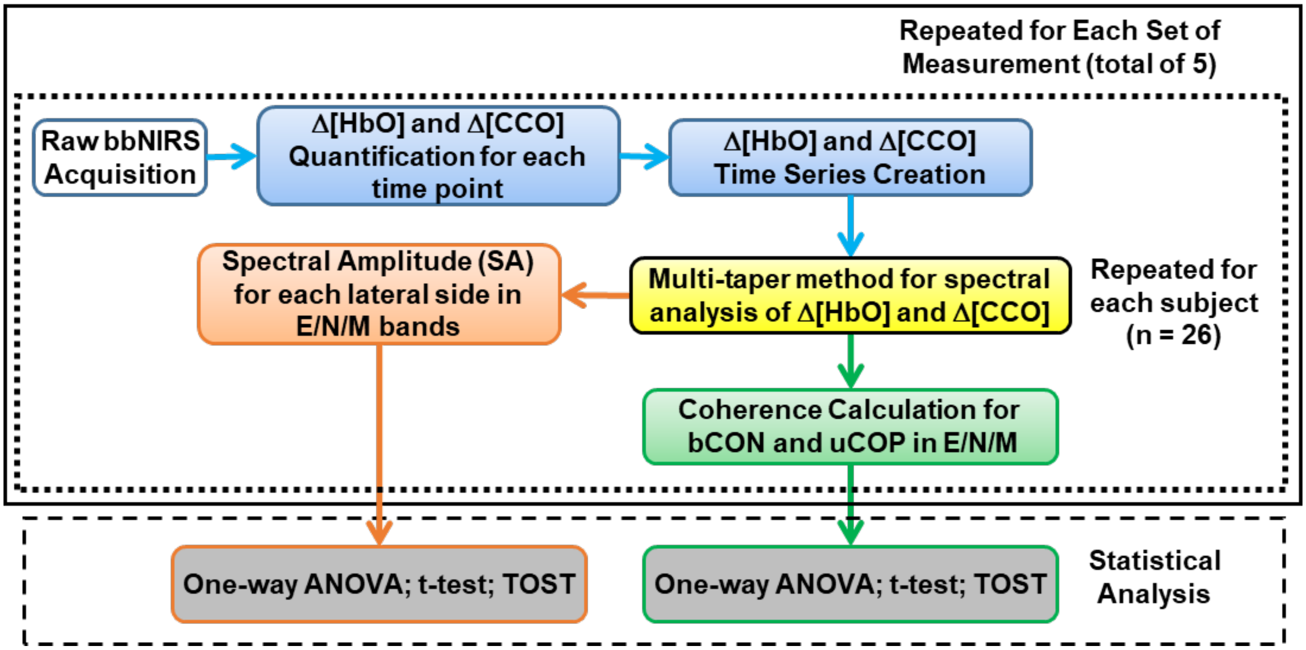

Figure 3. 2 A data processing flow chart with five steps. Step 1: Δ[HbO] and Δ[CCO] quantification at each time point and time series (blue boxes); Step 2: amplitude and phase decomposition using multi-taper method (yellow box); Step 3: quantification of spectral amplitudes (SA) for endogenic, neurogenic, and myogenic (E/N/M) frequency bands (orange box); Step 4: determination of four types of coherences for each E/N/M bands (green box). Steps 1 to 4 were repeated for each of 26 participants (outlined by the dotted box) and then for 5 sets of the measurements (outlined by the solid box). The bottom dashed box

marks Step 5, showing several statistical analyses, including one-way ANOVA, paired t-tests, and two one-sided tests (TOST) used to identify group-level features for SA and respective coherence parameters (gray box).

3.2.2.1 Step 1: Quantification of Δ[HbO] and Δ[CCO] time series

As mentioned in the Introduction, bbNIRS has been studied for more than two decades [130-134] and is well accepted as a reliable tool for quantifying cortical [HbO], [HHb], and [CCO] based on the modified Beer-Lambert law (MBL) [131, 135, 136]. Following the same approach, we selected the spectral range of 780-900 nm from the recorded optical spectrum at each time point, and quantified prefrontal Δ[HbO] and Δ[CCO] based on MBL and multiple linear regression analysis with a low-pass filter at 0.2 Hz [143]. Detailed derivations and steps can be found in Refs. [7, 142]. After repeating the concentration quantification at all recorded time points, we obtained a time series of Δ[HbO] and Δ[CCO] for the 7-min resting-state period at a sampling frequency of 0.67 Hz. The spectral range of 780-900 nm estimates the chromophore concentration with a low level of error propagated from noise [149].

3.2.2.2 Step 2: Multi-taper method for spectral analysis of Δ[HbO] and Δ[CCO]

The multi-taper method (MTM) [79, 80] is a well-known time-frequency analysis for a time series. Specifically, multiple tapers, mainly Slepian sequences, are used to taper the recorded signal in the time domain before performing the Fourier transform to provide a frequency-domain spectrum [79, 80]. This method maintains a reasonably high spectral resolution while reducing spectral noise. In this study, the MTM enabled us to decompose the amplitude and phase of the Δ[HbO] and Δ[CCO] time series obtained from both bbNIRS channels. Specifically, we utilized several functions (including “ft_freqanalysis” and “ft_connectivityanalysis”) available in the FieldTrip toolbox [76, 77] to perform MTM operations. Section B.1 in the Appendix explains the two functions of “ft_freqanalysis” and “ft_connectivityanalysis” and presents a detailed flow chart (Figure B1) to illustrate the calculations for SA.

3.2.2.3 Step 3: Quantification of SA in E/N/M Bands

One of the outputs of MTM is the power spectral density (PSD) smoothed over a given frequency range. In this study, smoothed PSDs of Δ[HbO] and Δ[CCO] over a 7-min resting period were obtained across E/N/M frequency bands. For a 7-min measurement duration, the spectral (or frequency) resolution was 1/(7 min)= 1/(7 × 60 sec)= 0.0024 Hz. Accordingly, the signal spectral power at each PSD frequency was obtained by multiplying the PSD value by the spectral resolution at the respective frequency. Next, by taking the square root of the spectral power, we were able to attain a spectrum of ISO amplitude versus frequency between 0.005 and 0.2 Hz (as selected in Step 1). Finally, we obtained the mean spectral amplitudes (SA) over each ISO band for Δ[HbO] and Δ[CCO]. The methodological steps are expressed as follows:

$$\text{amplitude}(f) = \sqrt{power(f)} = \sqrt{PSD(f)\times\Delta f} \tag{3-1}$$

$$\text{SA}_{\text{HbO}\_i} = \text{mean amplitude}(f) \text{ of } \Delta[\text{HbO}] \text{ over the } i\text{th band,} \tag{3-2}$$

$$\text{SA}_{\text{CCO}\_i} = \text{mean amplitude}(f) \text{ of } \Delta[\text{CCO}] \text{ over the } i\text{th band,} \tag{3-3}$$

where PSD(*f*), power(*f*), and amplitude(*f*) are the frequency-dependent spectra of PSD, power, and amplitude, respectively; *i* represents the *i*th band for E/N/M frequencies (i.e., *i* = E, N, M) on each side of the participant’s forehead.

3.2.2.4 Step 4: Hemodynamic and Metabolic Connectivity and Coupling by Coherence

In theory, brain connectivity measures rely on the amplitude and/or phase of the signal recorded from each channel to quantify the level at which each pair of signals interact with each other. Based on the mathematical definition of the connectivity measure, the correlation between the phases and/or amplitudes of two time series (recorded by two respective channels) can be interpreted as the functional connectivity/coupling of these time series [13, 14]. In contrast, the counterpart of the time-domain cross-correlation calculation is coherence in the frequency domain, which can be used to facilitate or quantify the cerebral connectivity in this study. The coherence coefficient is a normalized number between 0 and 1 without any unit, and is expressed as a function of frequency, ω, as follows [13]:

$$coh_{xy}(\omega) = \frac{\left|S_{xy}(\omega)\right|}{\sqrt{S_{xx}(\omega)\,S_{yy}(\omega)}} \;, \tag{3-4}$$

where S_{xx} and S_{yy} indicate the power estimates of the signals x and y, respectively, and S_{xy} represents the averaged cross-spectral density term of the two signals. These terms can be calculated using the complex values obtained from the MTM method [80, 150].

In the next step of spectral analysis, we quantified four pairs of spectral coherence for the resting-state human forehead: (1) bilateral coherence of Δ[HbO] to represent bilateral hemodynamic connectivity (bCON_{HbO}), (2) bilateral coherence of Δ[CCO] to represent bilateral metabolic connectivity of (bCON_{CCO}), (3) unilateral coherence between Δ[HbO] and Δ[CCO] on the left, and (4) right side of the forehead to designate hemodynamic-metabolic coupling on the respective prefrontal cortex (i.e., $\text{uCOP}_{\text{HbO-CCO\_L}}$ and $\text{uCOP}_{\text{HbO-CCO\_R}}$). In practice, the function of “ft_connectivityanalysis” available in the FieldTrip toolbox [76, 77] was used to facilitate these coherence spectra, followed by band averaging within each of the three (E/N/M) frequency bands of the ISO. The flow chart (Figure B1) in the Supplementary Material offers graphical steps for calculating coherence.

Step 5: Statistical Analyses for ISO features

The aforementioned steps were repeated for each of the two bbNIRS channels for all subjects during each of the five visits. Three stages of statistical analyses were performed for SA_{HbO} (or SA_{CCO}):

(1) ANOVA was performed to prove that there was no significant difference in SA_{HbO} (or SA_{CCO}) among the five measurements. This set of ANOVA tests was performed for each of the Δ[HbO] (or Δ[CCO]) metrics on the bilateral channels.

(2) A set of paired t-tests was performed to compare the bilateral values of grand-averaged SA_{HbO} (or SA_{CCO}) over five repeated measurements from all 26 participants at all three E/N/M bands.

(3) The two one-sided tests (TOST) analysis was utilized to evaluate the equivalence of the features that did not show a significant difference between bilateral values for SA_{HbO} (or SA_{CCO}). Details of the equivalence test using TOST can be found in Section B.2 of the Appendix.

After these stages of analyses, all bilaterally equivalent values of SA_{HbO} (or SA_{CCO}) at each E/N/M band were reported as features for the prefrontal hemodynamic (or metabolic) spectral amplitudes.

Similar statistical analyses of the three stages were performed on four coherence metrics that were band-averaged over all the subjects for each of the five visits. In ANOVA tests, after obtaining the bilateral connectivity indices for $bCON_{HbO}$ (or $bCON_{CCO}$) for all three E/N/M bands, a one-way ANOVA was performed to assess the similarity among the three bands, followed by Tukey's post hoc test or TOST to detect statistically different or equivalent $bCON_{HbO}$ (or $bCON_{CCO}$) indices, respectively, across the three bands. Finally, grand-averaged $uCOP_{HbO\text{-}CCO}$ indices on the two lateral (left and right) sides were compared using a set of paired t-tests for all three E/N/M bands. In case of no significant difference between the left and right $uCOP_{HbO\text{-}CCO}$ in any of the three bands, TOST was performed to test and prove the equivalence of the bilateral values of $uCOP_{HbO\text{-}CCO}$. Then, the averaged value of $uCOP_{HbO\text{-}CCO}$ was reported as a feature for prefrontal, resting-state hemodynamic-metabolic coupling.

3.3 Results

The hypothesis of this study was that bilateral hemodynamic and metabolic connectivity and unilateral coupling of the ISO in the resting human forehead can be quantified using 2-bbNIRS and may serve as measurable features reflecting the prefrontal brain state. To prove or support this, we took 7-min, resting-state, 2-bbNIRS measurements from the forehead of 26 young and healthy participants (after exclusion of five subjects). The analyzed results focused on (1) SAs, (2) bilateral coherence, and (3) unilateral coherence among four time series of Δ[HbO] and Δ[CCO] signals obtained from the prefrontal cortex.

3.3.1 Time Series of Δ[HbO] and Δ[CCO] versus Their Spectral Analysis

After fitting the MBL with the spectral data of 2-bbNIRS (Step 1), we obtained a 7-min time series of Δ[HbO] and Δ[CCO] from each lateral side of the forehead of each participant. As an example, Figures 3.3(a) and 3.3(b) show time profiles of Δ[HbO] and Δ[CCO] derived from one channel of one subject's dataset; their time series fluctuated around 0 between ± 0.3 μM and ± 0.04 μM, respectively. After performing spectral analysis (Step 2) and quantification of SA (Step 3), we obtained SA values for both Δ[HbO] and Δ[CCO], as shown in Figures 3.3(c) and (d), respectively, where the three frequency bands (E/N/M) are color-shaded. In addition, Section B.3 in the Appendix shows an example of the Δ[HbO] time series from one channel of 2-bbNIRS of a subject's dataset. This figure illustrates how different ISO waveforms in the three E/N/M bands contribute to the composition of the wideband (0.005–0.2 Hz) original signal.

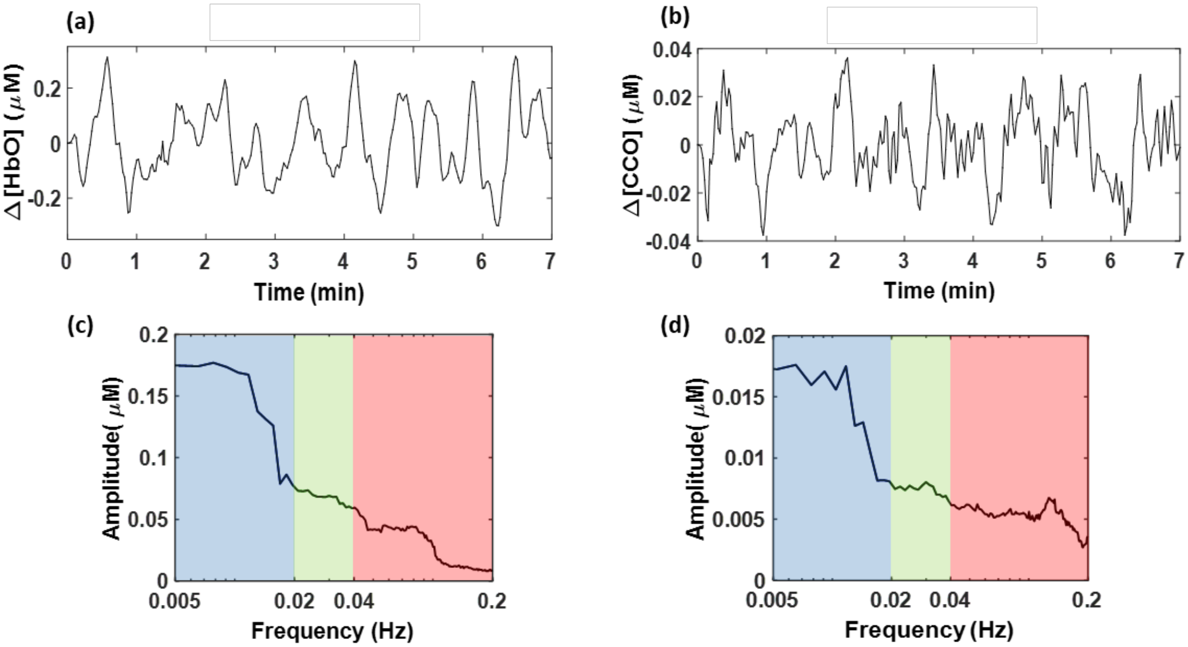

Figure 3. 3 (a) and (b) illustrate an example of time-domain representation of Δ[HbO] and Δ[CCO] signals, respectively, with a frequency band of 0.005-0.2 Hz over a period of 7 min. This set of time series was derived after processing Step 1 from one channel of the subject's dataset. (c) and (d) show the frequency-domain spectral amplitudes for Δ[HbO] and Δ[CCO], respectively, quantified using Steps 2 and 3. Blue, green, and red indicate endogenic, neurogenic, and myogenic bands, respectively.

3.3.2 ISO Spectral Amplitudes of Prefrontal Δ[HbO] and Δ[CCO] in the Resting Brain

Figures 3.4(a) and 4(c) show the SA_{HbO} and SA_{CCO} values in the E band, which are dominant over those in the other two bands. Furthermore, the paired t-test results demonstrated no significant difference in SA_{HbO} between the two prefrontal regions across all three E/N/M bands. These observations are in good agreement with those of a recent and independent study by our group [43], which utilized a completely different bbNIRS system and setup from a different cohort of participants. In addition, the data processing algorithms used to obtain the SA_{HbO} differed between the two studies. Similarly, SA_{CCO} values from both prefrontal cortices were statistically equivalent in the M band. However, the SA_{CCO} values in the left prefrontal cortex were significantly higher than those in the right prefrontal cortex in both the E- and N-bands.

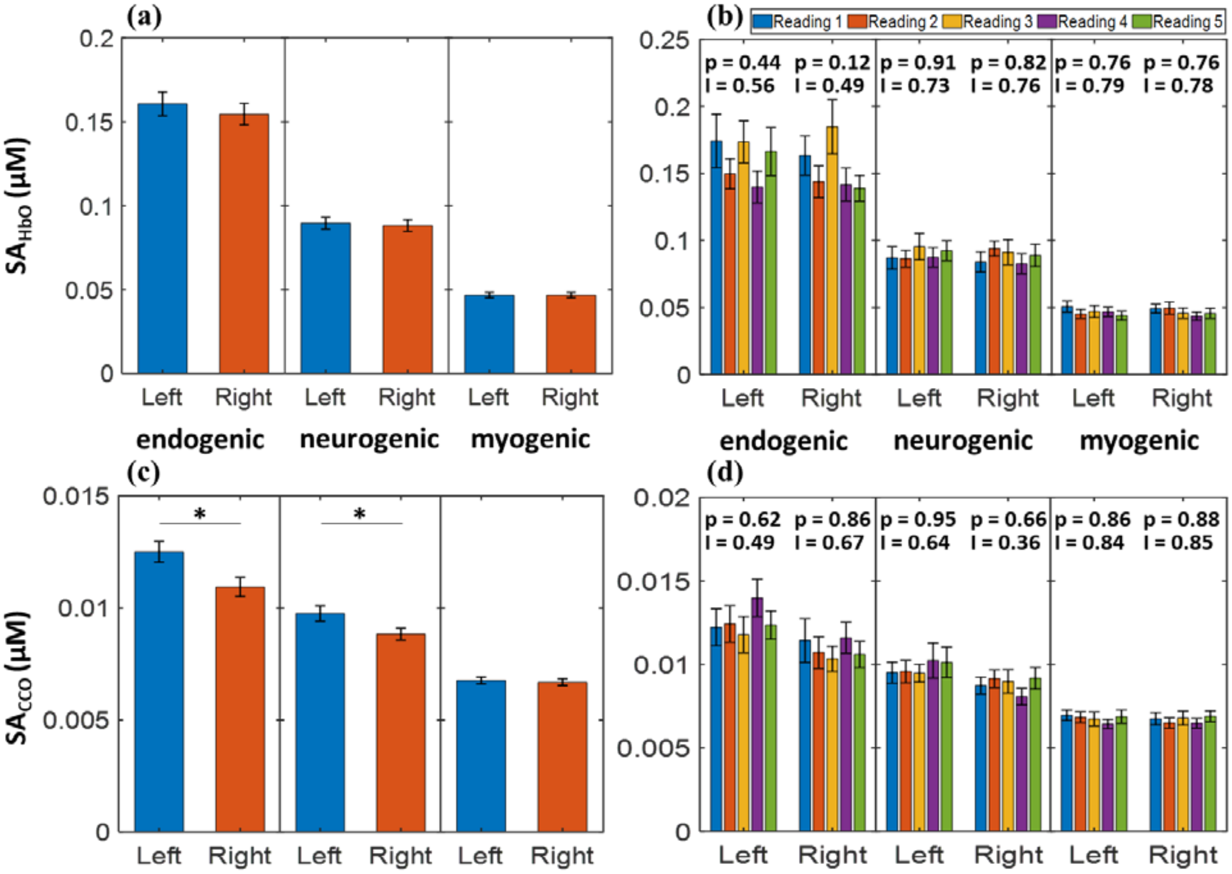

Figure 3. 4 Resting-state prefrontal SA_{HbO} (in μM) of the left and right forehead averaged over (a) a combined set of grand/total measurements (n=130) and (b) each individual set of five measurements (n=26 per set) at endogenic (E; 0.005-0.02 Hz), neurogenic (N; 0.02-0.04 Hz), and myogenic (M; 0.04-0.2 Hz) frequency bands. Similarly, resting-state prefrontal SA_{CCO} (in μM) of the left and right forehead averaged over (c) the combined set of measurements (n=130) and (d) each individual set of five measurements (n=26 per set) at E/N/M bands. p-values shown for each group of bars in (b) and (d) represent ANOVA results. All error bars are based on the standard error of the mean. *: $p<0.05$. I values represent intraclass correlation coefficients for each group.

To evaluate the consistency and stability of the 2-bbNIRS measurements, five sets of derived/quantified SA_{HbO} and SA_{CCO} values were determined and plotted in Figures 3.4(b) and 3.4(d), respectively. One-way ANOVA was performed to assess significant differences among the five measurements. The analysis outcomes showed no statistically significant differences among the five datasets for each of the three frequency bands. In addition, intraclass correlation coefficient

(ICC) was calculated and reported in this figure for the 5 repeated measurements to evaluate the reproducibility of the feature in the subject level.

Specifically, the second and third columns from the left of Table 3.1 represent the grand averages of SA_{HbO} values (as shown in Figure 3.4) over all experiments (n=130) taken from the left and right prefrontal cortices of the 26 participants across the three ISO frequency bands. The fourth and fifth columns list the p-values and p_{TOST} obtained from the paired t-tests and TOST analysis, respectively, between the left and right SA_{HbO} values. This table indicates that left and right SA_{HbO} values were statistically equivalent in each E/N/M band; thus, the bilateral average was calculated and is presented in the last column from the left. In addition, Table 3.2 shows the results of SA_{CCO} in the three E/N/M bands using the data presentation similar to Table 3.1. It is clear that the myogenic band was the only one with equivalent left and right prefrontal SA_{CCO}. Overall, four bilaterally equivalent SA values were found as ISO features to characterize prefrontal ISO of the resting human brain.

Table 3. 1 Grand averages of SA_{HbO} over all measurements (n=130) on the left and right forehead across three ISO frequency bands

Frequency band	**$SA_{HbO, left}$ (mean ± s.d.)**	**$SA_{HbO, right}$ (mean ± s.d.)**	**Left vs right t-test (p-value)**	**Left vs right TOST (p_{TOST})**	**Bilateral average SA_{HbO} (mean ± s.d.)**
Endogenic	0.16 ± 0.08	0.15 ± 0.07	0.52	< 0.01; bilaterally equivalent	**0.16 ± 0.07**
Neurogenic	0.09 ± 0.04	0.09 ± 0.04	0.76	< 0.01; bilaterally equivalent	**0.09 ± 0.04**
Myogenic	0.05 ± 0.02	0.05 ± 0.02	0.99	< 0.01; bilaterally equivalent	**0.05 ± 0.02**

Note: p-values and p_{TOST} were obtained using paired t-tests and TOST, respectively. See Section B.2 in the Supplementary Material for details on TOST.

Table 3. 2 Grand averages of SA_{CCO} over all measurements (n=130) on the left and right forehead across three ISO bands

Frequency band	$SA_{CCO, left}$ (mean ± s.d.)	$SA_{CCO, right}$ (mean ± s.d.)	Left vs right t-test (p-value)	Left vs right TOST (p_{TOST})	Bilateral average SA_{CCO} (mean ± s.d.)
Endogenic	0.013±0.005	0.011±0.005	< 0.02	0.11	Left > right
Neurogenic	0.010±0.004	0.009±0.003	< 0.04	0.08	Left > right
Myogenic	0.007±0.002	0.007±0.002	0.72	< 0.001; bilaterally equivalent	**0.007±0.002**

Note: p-values and p_{TOST} were obtained using paired t-tests and TOST, respectively. See Section B.2 in the Supplementary Material for details on TOST.

3.3.3 ISO Coherence of Prefrontal Δ[HbO] and Δ[CCO] in the Resting Human Brain

Figure 3.5(a) shows the comparisons between bilateral cerebral hemodynamic connectivity and bilateral metabolic connectivity over the three ISO bands. Paired t-tests confirmed that $bCON_{HbO}$ was significantly stronger than $bCON_{CCO}$ in all the E/N/M bands. To evaluate the significant differences in these values, both $bCON_{HbO}$ and $bCON_{CCO}$ for bilateral connectivity were calculated for each set of five measurements and are plotted separately in Figure 3.5(b). After performing a one-way ANOVA on these five datasets, we confirmed that no statistically significant difference in bilateral connectivity existed among the five datasets at all three frequency bands for both Δ[HbO] and Δ[CCO], as evidenced by the p-values in Figure 3.5(b). In addition, intraclass correlation coefficient (ICC) was calculated and reported in this figure for the 5 repeated measurements to evaluate the reproducibility of the feature in the subject level.

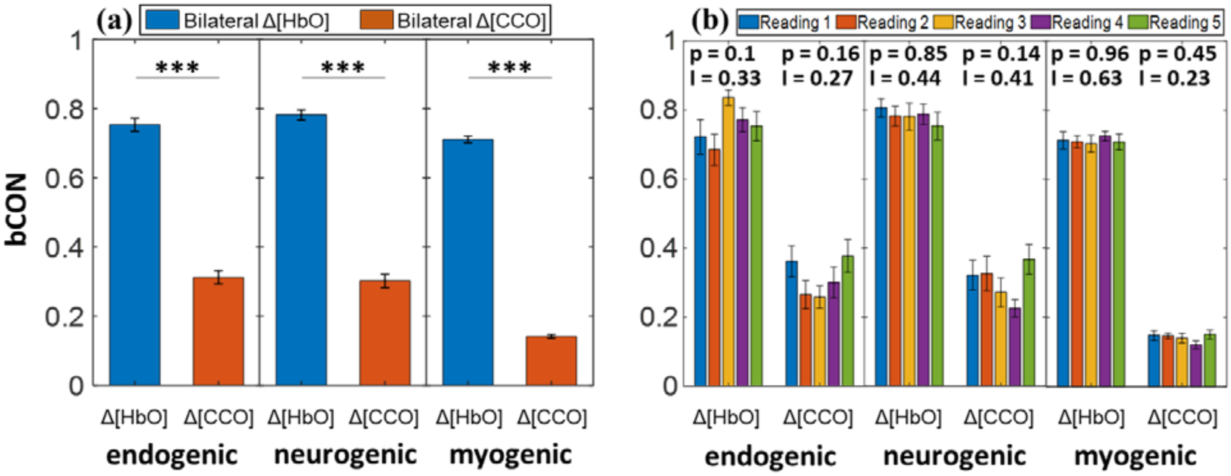

Figure 3. 5 Resting-state prefrontal bCON_{HbO} and bCON_{CCO} averaged over (a) the combined set of measurements (n=130) and (b) each separate set of five measurements (n=26 per set) over E (0.005-0.02 Hz), N (0.02-0.04 Hz), and M (0.04-0.2 Hz) bands. p-values shown on top of each group of the bars in (b) represent one-way ANOVA results. All error bars indicate the standard error of the mean. ***: $p<0.001$. I values represent intraclass correlation coefficients for each group.

Specifically, the bCON_{HbO} and bCON_{CCO} values averaged over the grand group (n=130) for all three E/N/M bands are listed in Table 3.3, with p-values obtained from one-way ANOVA (the fifth column for the left) and Tukey's post hoc test (the sixth column). A significant difference in bCON_{HbO} (or bCON_{CCO}) was observed among the three frequency bands. Next, we identified that bCON_{HbO} values at the E and N bands were not significantly different using Tukey's post hoc test and were statistically equivalent based on TOST. Therefore, these two indices were pooled to achieve an averaged connectivity value. The same statistical analysis and spectral average over the E and N bands were achieved for the bCON_{CCO} values too, as listed in the rightmost column of Table 3.3. In this case, we found two more ISO features (i.e., bilateral hemodynamic and metabolic connectivity) that may be characteristic in the resting-state prefrontal human cortices.

Table 3. 3 Resting-state prefrontal connectivity ($bCON_{HbO}$ and $bCON_{CCO}$) averaged over the grand data set (n=130) at E/N/M band

Bilateral Connectivity	Endogenic (mean±s.d.)	Neurogenic (mean±s.d.)	Myogenic (mean±s.d.)	ANOVA over three bands (p-value)	E vs N Tukey's (p-value)	E vs N TOST (p_{TOST})	E, N average (mean ± s.d.)
$bCON_{HbO}$	0.75 ± 0.20	0.78 ± 0.16	0.71 ± 0.10	< 0.003	0.35	< 0.001; laterally equivalent	**0.77 ± 0.17**
$bCON_{CCO}$	0.31 ± 0.21	0.30 ± 0.21	0.14 ± 0.06	< 0.001	0.89	<0.04; laterally equivalent	**0.31 ± 0.21**

Note: The p-values in the 5th column from the left were obtained from one-way ANOVA to compare those at the E/N/M bands. The p-values in the 6th column from the left were obtained from Tukey's post hoc test to compare bCON values averaged over the E and N bands. The p_{TOST} values were obtained from TOST.

Another set of coherence analyses was performed to determine the cerebral hemodynamic-metabolic coupling on each prefrontal side. Unilateral coupling between Δ[HbO] and Δ[CCO] indicates the level at which hemodynamic and metabolic infra-slow oscillations are synchronized and coupled. Figure 3.6(a) shows the $uCOP_{HbO-CCO}$ values derived from the right and left channels in each E/N/M band. Paired t-tests revealed that the $uCOP_{HbO-CCO}$ values between the left and right prefrontal cortices were statistically identical in the E and M bands. Figure 3.6(b) illustrates the unilateral coupling averaged over each measurement group for the five repeated measurements. A one-way ANOVA over the five readings showed no significant difference for each coupling pair on each lateral side, as evidenced by the p-values given at the top of Figure 3.6(b). In addition, intraclass correlation coefficient (ICC) was calculated and reported in the figure 3.6(b) for the 5 repeated measurements to evaluate the reproducibility of the feature in the subject level. In the neurogenic band, the $uCOP_{HbO-CCO}$ value in the left prefrontal region was significantly higher than that on the right side, indicating an intrinsic lateral difference in neurogenic oscillation in resting-state hemodynamic-metabolic coupling.

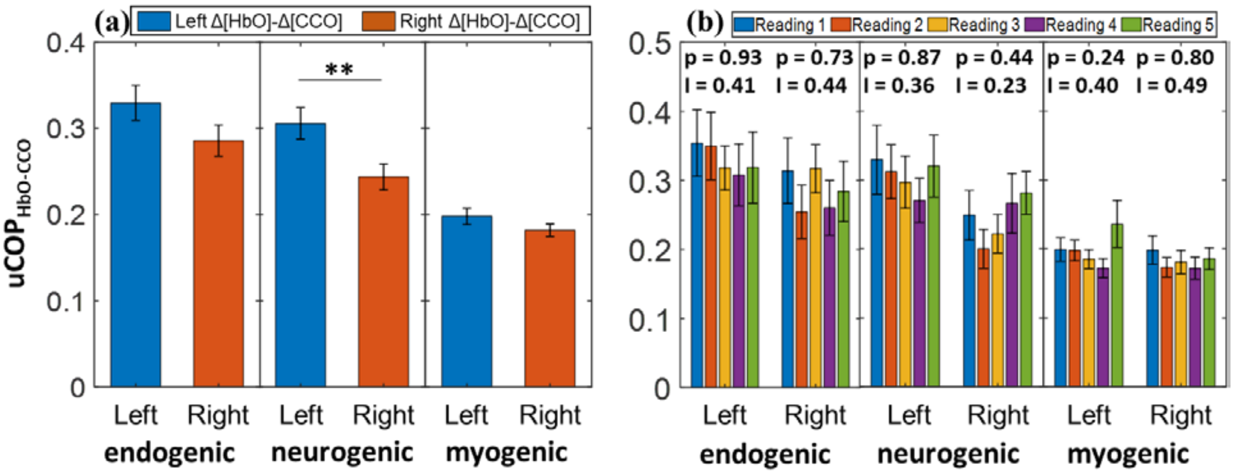

Figure 3. 6 Left and right resting-state prefrontal uCOP$_{HbO-CCO}$ obtained from (a) combined grand group (n=130) and (b) separate groups (n=26 each) over endogenic (0.005-0.02 Hz), neurogenic (0.02-0.04 Hz), and myogenic (0.04-0.2 Hz) frequency bands. p-values above each group of bars in (b) represent results from ANOVA test. The error bars indicate the standard error of the mean. **: $p < 0.01$. I values represent intraclass correlation coefficients for each group.

Table 3.4 lists the uCOP$_{HbO-CCO}$ values over the left and right prefrontal cortices across the three ISO frequency bands averaged over the grand set of experiments (n=130). P-values obtained from the paired t-test for uCOP$_{HbO-CCO, left}$ vs. uCOP$_{HbO-CCO, right}$ are reported in the fourth column from the left of Table 3.4. In the case of no significant difference in uCOP$_{HbO-CCO}$ between the left and right channels in the endogenic and myogenic bands, TOST for equivalence tests were perfomed with the p_{TOST} values reported in Table 3.4. Accordingly, the bilateral average of uCOP$_{HbO-CCO}$ was calculated and represented in the rightmost column. These bilaterally averaged uCOP$_{HbO-CCO}$ values at the E and M bands are the 7th and 8th features that we identified in this study as potential biomarkers for characterizing brain disorders in the future.

Table 3. 4 Prefrontal $uCOP_{HbO\text{-}CCO}$ values on the left and right cortical regions averaged over the grand set of measurements (n=130) at each of the E/N/M bands

Frequency band	**$uCOP_{HbO\text{-}CCO,left}$ (mean ± s.d.)**	**$uCOP_{HbO\text{-}CCO,right}$ (mean ± s.d.)**	**Left vs right t-test (p-value)**	**Left vs right TOST (p_{TOST})**	**Bilateral average (mean ± s.d.)**
Endogenic	0.33 ± 0.22	0.29 ± 0.20	0.11	0.02; laterally equivalent	**0.31 ± 0.21**
Neurogenic	0.31 ± 0.20	0.24 ± 0.17	< 0.01	0.7	Left > right
Myogenic	0.20 ± 0.10	0.18 ± 0.08	0.18	0.04; laterally equivalent	**0.19 ± 0.09**

Note: p-values and p_{TOST} were obtained from paired t-tests and TOST, respectively, between the left and right $uCOP_{HbO\text{-}CCO}$.

3.4 Discussion

NIRS-based methods have been demonstrated and reported as well-known, non-invasive approaches to monitor the metabolic and hemodynamic activity of the human brain, and thus having great potential for clinical applications [136, 151, 152]. Because NIRS quantifies only changes in cerebral hemodynamics, it is not applicable in clinical practice for disease diagnosis or monitoring when the human brain is in a resting state. For instance, diffuse correlation spectroscopy and functional NIRS only detect the relative blood flow index and relative changes in hemoglobin concentration, respectively [153].

To address this weakness of NIRS, we developed a frequency-domain analysis to determine the spectral amplitudes (SA) and coherence indices for each ISO time series on both sides of the prefrontal cortex. While both the Δ[HbO] and Δ[CCO] time series in the resting brain expressed changes with respect to a baseline point, each SA of the oscillation would be an absolute value, in μM, and signified the respective oscillation amplitude. Because the analysis was performed in the frequency domain, SA values in the E/N/M bands denoted oscillation magnitudes of HbO and

CCO at the three respective rhythms. In addition, coherence indices are absolute values in the range of 0 to 1, regardless of the unit. It represents the degree of oscillatory similarity between the two neurophysiological rhythms. Accordingly, we developed and demonstrated a low-cost, portable, 2-channel bbNIRS system to record cerebral hemodynamic and metabolic ISO activity over the prefrontal cortex of healthy young humans with a relatively large sample size (n=26). The recorded signals were analyzed using a frequency-domain approach to quantify the spectral amplitude and connectivity/coupling of ISO in the resting human brain. As discussed below, this study enabled us to prove and support our hypothesis by achieving absolute quantification of ISO-resolved hemodynamics and metabolism in the resting-state prefrontal human cortices. The quantified metrics were shown to be relatively stable and thus may have great potential to be developed as biomarkers for the characterization, diagnosis, and monitoring of certain brain disorders.

3.4.1 ISO Spectral Amplitudes of Prefrontal Δ[HbO] and Δ[CCO] as Brain-state Features

The ISO (0.005-0.2 Hz) consists of three distinct frequency components: endogenic (0.005-0.02 Hz), neurogenic (0.02-0.04 Hz), and myogenic (0.04-0.2 Hz). Each frequency band is associated with a specific neurophysiological activity in the healthy human brain [115-117, 154]. Thus, abnormal brain activity and neurological disorders in the human brain are associated with impaired or irregular patterns of cerebral hemodynamic and metabolic ISOs. Several studies have reported a relationship between ISO impairment and cardiovascular disease, Alzheimer’s disease, hypertension, and stroke [40, 41, 119].

In this study, we quantified ISO-resolved spectral amplitudes of prefrontal oxygenated hemoglobin (SA_{HbO}) and oxidized cytochrome c oxidase (SA_{CCO}) in healthy young humans. Next, we demonstrated that the SA_{HbO} and SA_{CCO} values averaged over 26 participants with five different repeated measurements were relatively stable and consistent, as evidenced by the ANOVA results shown in Figure 3.4(b). Furthermore, as shown in Figure 3.4(a) and Table 3.1, the average SA_{HbO} values over the two lateral sides of the prefrontal cortex were statistically equivalent, indicating similar levels of hemodynamic oscillation in the bilateral prefrontal cortices in all vasomotion-derived ISO (i.e., E/N/M) bands. Thus, a set of standard prefrontal SA_{HbO} values for each of the three ISO bands can be established and further examined as features that characterize abnormal brain functions. As shown in Figure 3.4(c) and Table 3.2, identical or equivalent levels of grand-averaged SA_{CCO} between the two prefrontal cortices in the myogenic band are unambiguous, implying that this metric can be considered another potential prefrontal feature.

It is worth noting that the grand-averaged SA_{CCO} indices were significantly larger on the left than on the right prefrontal side in both the E- and N-bands. This observation may imply higher metabolic activity in endogenic and neurogenic rhythms on the left side than on the right side of the resting prefrontal cortex. As reported by [155], the dominant source of resting-state lateralization in human brain activity is the default mode network (DMN), which is associated with internal thoughts. The study [155] provided evidence that the DMN is predominantly active in the left prefrontal cortex in the resting state, especially in right-handed participants. The implication of our observation matched well with the results of Liu et al. (2009) because most of our participants were right-handed and would give rise to higher anterior default-mode activity in the left prefrontal cortex [155, 156]. Furthermore, as illustrated in Figures 3.4(a) and 3.4(c), the endogenic band had higher values for SA_{HbO} and SA_{CCO} than those of the other two bands. This phenomenon has also been reported in other studies that have used different NIRS systems and analysis algorithms as well [35, 124, 157].

3.4.2 Cerebral Hemodynamic and Metabolic ISO Connectivity/Coupling as Features

As shown in Figure 3.5(a) and Table 3.3, robust bilateral connectivity of prefrontal hemodynamics ($bCON_{HbO}$) was identified over the E/N frequency bands in 26 young healthy human subjects at rest, over five repeated measurements. This high level or index of connectivity may imply synchronized hemodynamic activity mediated by endothelial cells and inter-neurons on lateral prefrontal regions [158-160]. In contrast, $bCON_{CCO}$ showed a significantly lower level of bilateral functional connectivity than $bCON_{HbO}$. A lower level of $bCON_{CCO}$ can be expected because unilateral [CCO] activity is locally driven by oxygen consumption and/or mitochondrial metabolism within neurons, has specific functions distinct from those of the other lateral prefrontal cortex, and has less need to link to the other side. Similar to $bCON_{HbO}$, $bCON_{CCO}$ was statistically identical over the E and N frequency bands. These observations are in good agreement with those of a recent study by our group, which had a smaller sample size and utilized a different 2-bbNIRS setup and analysis methods [43]. Furthermore, Figure 3.5(b) illustrates the ANOVA-driven results with non-significant differences among the $bCON_{HbO}$ (or $bCON_{CCO}$) values over 130 measurements. These high stabilities suggest and support the possibility of using these metrics as new neurophysiological features to characterize the human brain state.

As the final metric, the unilateral hemodynamic-metabolic coupling ($uCOP_{HbO\text{-}CCO}$) in the right and left channels is plotted in Figure 3.6(a). As shown in this figure and reported in Table 3.4, no significant difference in $uCOP_{HbO\text{-}CCO}$ between the two lateral sides existed at both the E and M bands; thus, bilaterally pooled coupling indices at both E/M bands could be achieved. Similar to the other metrics shown above, Figure 3.6(b) illustrates the ANOVA-driven results of the statistically non-significant $uCOP_{HbO\text{-}CCO}$ values/indices bilaterally over 130 measurements in the E and M bands. Thus, prefrontal $uCOP_{HbO\text{-}CCO}$ in the E and M bands can be included and tested as resting-state features in future clinical applications.

In contrast, the neurogenic component of $uCOP_{HbO\text{-}CCO}$ was significantly higher in the left prefrontal cortex than in the right prefrontal cortex. This observation may imply a higher vascular-metabolic interactivity on the left prefrontal cortex than on its contralateral side. Given that most of our participants were right-handed, higher hemodynamic-metabolic coupling in the left prefrontal cortex would be expected [155, 156].

As mentioned in the Introduction, relaxation-contraction cycles of blood vessel walls are expected to be the driving force for the ISO rhythms of cerebral hemodynamics. However, the driving force of the ISO for CCO is unclear. A recent study using fMRI and PET demonstrated a strong correlation between slow oscillations (0.01-0.1 Hz) of hemodynamics and metabolism in the brain [161]. Specifically, the authors concluded that metabolic demand for glucose and oxygen regulates low-frequency hemodynamic fluctuations. Because of the strong correlation and thus close coupling between HbO and CCO constituents, we speculated that the three E/N/M oscillations originating from slow vasomotion may be passed or translated to mitochondrial (CCO) oscillations at the E/N/M rhythms.

3.4.3 Eight Measurable Features of Prefrontal ISO

In Section 3.3, we confirmed our hypothesis that prefrontal cortical connectivity and coupling of the ISO can be quantified using 2-bbNIRS as features that reflect the brain state. Specifically, through the aforementioned content, we demonstrated several stable or consistent metrics based on prefrontal bilateral connectivity and unilateral coupling of ISO. Based on the analyses and discussions given in Sections 3.4.1 and 3.4.2, we list eight metrics as measurable features in Table 3.5. These features can be further studied and validated using a larger sample size of both healthy human participants and patients with certain brain disorders. In addition, the ICC values for different features demonstrated that the subject-level reproducibility needs to be improved and more robust methodology must be obtained by modifying the current method.

Table 3. 5 Measurable ISO features for characterization of the prefrontal human brain at rest

ISO features (frequency band)	**Average over two lateral sides (μM)**
SA_{HbO} (E)	0.16±0.07
SA_{HbO} (N)	0.09±0.04
SA_{HbO} (M)	0.05±0.02
SA_{CCO} (M)	0.007±0.002
ISO features (frequency band)	**connectivity between two lateral sides**
bCON_{HbO} (E/N)	0.77±0.20
bCON_{CCO} (E/N)	0.31±0.18
ISO features (frequency band)	**Average over two lateral sides**
$\text{uCOP}_{\text{HbO-CCO}}$ (E)	0.31±0.21
$\text{uCOP}_{\text{HbO-CCO}}$ (M)	0.19 ± 0.09

3.4.4 Limitations

First, the relatively low sampling frequency and short data collection duration (i.e., 7-min) prevented us from achieving high-frequency resolution, which may have led to low accuracy in spectral amplitude and coherence calculations in the low-frequency range, especially in the endogenic band. It is suggested to have a longer measurement duration, for example, 10 min or longer. Second, our bbNIRS system was sensitive to motion; the eyes-closed resting-state protocol may have caused sleepiness in the participants during the measurements. Finally, our quantified results or metrics may be contaminated by the extracranial layers of the human head. It is known that fNIRS signals obtained over the scalp of human participants are contaminated by extracranial layers, namely, the human scalp and skull. To minimize this potential confounding factor, additional optical channels of fNIRS with a short source-detector (S-D) separation (commonly ~0.8-1.2 cm) have been used for systemic noise removal in task-evoked hemodynamic studies

[162-166], where a cortical region was activated by stimulating tasks. However, most fNIRS-based studies for quantifying resting-state functional connectivity (RSFC) have not developed an appropriate methodology to remove this confounding effect [147, 148]. It is reported only recently that RSFC can be quantified more accurately with a short S-D reading correction than without correction [167].

3.4.5 Future work

In future work, to enable a longer-period and less-artifact recording from the human brain, modifications or improvements are needed in the bbNIRS setup, measurement protocol, and computational methods to reduce movement artifacts and systemic/physiological noises. In addition, it is necessary to consider the implementation of short-distance channels in bbNIRS to remove the possible contamination of extracranial layers from the determined/interpreted results.

The current study included only healthy controls without any disease-related patients; thus, it was an exploratory study [42]. While we believe that the identified ISO features are good neurological representations of the human brain, proof-of-principle or confirmatory research must be conducted for these features to become biomarkers of neurological diseases. Such studies include two parts. First, the features need to be stable, reliable, and with known or tested dependence on age, sex, and brain state. All of these quantifications need to be obtained using a statistically large sample size of healthy controls. Second, the features must be efficient in significantly classifying controls and patients with selected neurological disorders. Third, since the final verified biomarkers will be used to identify physiological disorders in individual subjects, more robust methodology needs to be developed to obtain consistent biomarkers with high reproducibility for each subject.

In addition, the observed differences between left and right prefrontal cortices in features such as SA_{CCO} and $uCOP_{HbO\text{-}CCO}$ needs to be further investigated to understand the physiological and functional mechanism behind these features in different locations of PFC.

3.5. Conclusion

In this study, we hypothesized that 2-bbNIRS, along with frequency-domain analysis, enables the quantification of prefrontal cortical connectivity and coupling of ISO in the resting human brain. To test this hypothesis, we implemented 2-channel bbNIRS and performed bilateral, prefrontal, 7-min measurements in an eyes-closed resting state in vivo from 26 young and healthy participants, repeated 5 times over 5 weeks. The measured time series were analyzed using a frequency-domain approach to detect cerebral hemodynamic and metabolic ISO in three endogenic, neurogenic, and myogenic frequency bands at rest. Specifically, coherence analysis facilitated the quantification of bilateral connectivity and unilateral hemodynamic-metabolic coupling in the human prefrontal regions. Accordingly, we identified eight stable resting-state ISO-specific metrics or features, including bilaterally averaged SA_{HbO} in all three bands, bilaterally averaged SA_{CCO} in the M band only, and bilaterally connected network metrics for both $bCON_{HbO}$ and $bCON_{CCO}$, each of which were statistically identical in the E and N frequency bands, respectively. The last two features were the bilaterally averaged coupling indices of $uCOP_{HbO\text{-}CCO}$ over the E- and M-bands, given that the coupling indices were statistically equivalent for both bands. All eight metrics as features showed a statistically stable level for 130 measurements. In short, this exploratory study developed a quick, low-cost, and effective methodology for exploring several prefrontal cortical connectivity and coupling features in the resting, healthy, and young human brains. The framework reported in this paper has demonstrated the potential of ISO features to be translatable for future clinical applications, while further confirmatory studies are needed before these features become effective biomarkers to identify certain neurological disorders.

3.6. Effect of Gender on Measurable Features of Prefrontal ISO

After separating the female and male groups, the proposed measurable features were compared between these groups using paired t-test and TOST. The features with similar value between male and female groups are represented in table 3.6.

Table 3. 6 Measurable ISO features for characterization of the prefrontal human brain at rest with similar values between male and female groups (the reported values are average of all measurements, including male and female subjects)

ISO features (frequency band)	**Average over two lateral sides (μM)**
SA_{HbO} (E)	0.16±0.07
ISO features (frequency band)	**connectivity between two lateral sides**
$bCON_{HbO}$ (E/N)	0.77±0.20
$bCON_{CCO}$ (E/N)	0.31±0.18
ISO features (frequency band)	**Average over two lateral sides**
$uCOP_{HbO-CCO}$ (E)	0.31±0.21
$uCOP_{HbO-CCO}$ (M)	0.19 ± 0.09

Chapter 4

Wavelength- and Site-Specific Effects of Prefrontal Photobiomodulation in vivo on Bilateral Metabolic Connectivity and Unilateral Metabolic-Hemodynamic Coupling in Humans

Sadra Shahdadian, Xinlong Wang, Shu Kang, Caroline Carter, Akhil Chaudhari, Hanli Liu

(This chapter is a manuscript that is ready to be submitted soon)

4.1 Introduction

The central nervous system, and in particular, the brain, is one of the dominant consumers of oxygen and glucose in the human body due to comparably high levels of metabolism even at rest. Furthermore, neural oxidative respiration, which is closely related to the level of the oxygen supply, modulates the energy metabolism in the neurons. Furthermore, previous studies have demonstrated the role of intrinsic vascular wall rhythmic relaxation-contraction (i.e., vasomotion) in human cerebral metabolic and hemodynamic activity. These spontaneous infra-slow oscillations (ISO), which are dominant in frequencies between 0.005 and 0.2 Hz, have been related to different human brain functions such as cognitive function. In addition, disturbances in vasomotion have been associated with aging and neurological disorders and diseases such as atherosclerosis [39], cardiovascular disease [40], and Alzheimer’s Disease [41]. In other studies published by our group [43, 44], we have shown that the vasomotion and its characteristics over the prefrontal cortex in rest can be quantified as biomarkers for healthy humans.

The infra-slow vasomotion, which is independent of respiration and heartbeat, consists of three distinct physiologically/biochemically-sourced components. Briefly, oscillation in releasing potent vasoactive factors, such as nitric oxide (NO), free radicals, prostacyclin, endothelium-derived hyperpolarizing factor, and endothelin lead to rhythmic physiological activities in the endogenic frequency band (0.005-0.02 Hz) which corresponds to relaxation-contraction cycles in the endothelial layer of the vascular wall. The neurogenic component (0.02-0.04 Hz), on the other hand, is sourced in released vasoactive ions and neurotransmitters from neurons, and myogenic activity (0.04-0.2 Hz), is representing the dilation-contraction of the smooth muscle cells on the vessel wall [117].

Functional Near-Infrared Spectroscopy (fNIRS) [38], functional Magnetic Resonance Imaging (fMRI) [121], and transcranial cerebral doppler (TCD) [122] are the common methods for detecting the hemodynamic ISO. Nevertheless, a better understanding of the mechanism behind human cerebral metabolism requires sophisticated methods of simultaneous monitoring of hemodynamic and metabolic activity in the region of interest. Mitochondrial activity and its oscillations can be quantified as a direct method to monitor metabolic ISO [123]. The metabolic state of living tissue can be detected by the concentration of redox-state cytochrome c oxidase (CCO) which is the terminal enzyme in the mitochondrial respiratory chain [137-140].

Previous studies have demonstrated the capability of broadband near-infrared spectroscopy (bbNIRS) in the detection and quantification of changes in concentration of oxygenated hemoglobin (i.e., Δ[HbO]), deoxygenated hemoglobin (i.e., Δ[HHb]), and redox-state cytochrome c oxidase (i.e., Δ[CCO]). The concentration quantification in this method is based on the absorption and scattering characteristics of these chromophores in the living tissue [130-134]. Due to the lower concentration of Δ[CCO] in comparison to Δ[HbO] and Δ[HHb], multiple wavelengths are required in the NIRS system to optimally quantify the changes in absorption and scattering characteristics of the tissue [135, 136, 141].

Transcranial photobiomodulation (tPBM), as a non-invasive method of neuromodulation [47, 168], is shown to alter cerebral hemodynamic and metabolic states [7, 9, 169]. This method in which a low-intensity laser or light-emitting diode (LED) is employed to deliver light to the human brain, is shown to improve human cognitive activity or treat different neurological disorders [2, 47, 168]. Previous studies demonstrated the dose-dependent nature of tPBM in the modulation of Δ[HbO] and Δ[CCO], especially in the human prefrontal cortex [7, 9, 169]. Furthermore, 1064 nm tPBM delivered to the right prefrontal cortex can alter the brain's hemodynamic, metabolic, electrophysiological functional connectivity at rest [43, 105, 170].

Our group recently introduced a set of hemodynamic and metabolic characteristics quantified by frequency-domain spectral amplitude and connectivity analysis of hemodynamic and metabolic ISO activity of prefrontal cortex, assessed by dual-channel bbNIRS setup [43]. These metrics are (1) bilateral hemodynamic (i.e., [HbO]) connectivity, (2) bilateral metabolic (i.e., [CCO]) connectivity, (3) unilateral hemodynamic-metabolic coupling on the left and (4) right side of the prefrontal cortex. In addition, we have demonstrated that these constant and highly reproducible characteristics can be considered potential biomarkers to identify neurological disorders and diseases [44]. Furthermore, we have shown distinct alterations in these metrics as well as Δ[HbO] and Δ[CCO] ISO spectral amplitudes across all three frequency bands in response to 1064-nm tPBM. Modulation of Δ[HbO] and Δ[CCO] in response to tPBM is also demonstrated to be wavelength-dependent in other studies [12]. However, no behavioral or physiological alteration is reported in response to left prefrontal tPBM. Thus, it would be beneficial to investigate the effect of the laser's wavelength and stimulation site on the alteration of the proposed metrics.

In this study, young healthy human participants were at rest while Δ[HbO] and Δ[CCO] time series with a sampling frequency of 0.67 Hz were acquired using a 2-bbNIRS system from two sides of the prefrontal cortex in pre- and post-tPBM. These time series were then analyzed to quantify the amplitude and coherence of hemodynamic and metabolic ISO over three frequency bands. In the first set of analyses, we assessed the spectral amplitude of hemodynamic and metabolic activity (SA_{HbO} and SA_{CCO}) over the three ISO frequency bands. Then, four physiological metrics were used to characterize the connectivity/coupling between each pair of signals. These measures include (1) bilateral hemodynamic connectivity ($bCON_{HbO}$), (2) bilateral metabolic connectivity ($bCON_{CCO}$), (3) coupling between cerebral hemodynamic and metabolic activities on the ipsilateral side to the stimulation ($uCOP_{Ipsi}$), and (4) coupling between cerebral hemodynamic and metabolic activities on the contralateral side to the stimulation ($uCOP_{Contra}$), of the prefrontal cortex over the three ISO frequency bands. Five separate visits with different conditions were used for each participant including 8 minutes of (1) Right prefrontal 800-nm laser, (2) Right prefrontal 850-nm laser, (3) Right prefrontal sham, (4) Left prefrontal 800-nm laser, (5) Left prefrontal sham.

In the end, we would support the hypothesis that hemodynamic and metabolic ISO is significantly modulated by tPBM. This modulation is distinct for each frequency band, can be local or bilateral/global, and in some cases is closely related to the wavelength and stimulation location. These observations can be beneficial for further investigation of the mechanism behind cerebral metabolism as well as wavelength- or location-specific cognitive function improvement or treatment of neurological disorder/disease based on the modulated metric and frequency band.

4.2 Materials and Methods

4.2.1 Participants

The dataset used for this study was the same as our previous study (i.e., chapter 3) [44]. 31 healthy human participants were recruited from the local community of the University of Texas at

Arlington. They were screened by the same inclusion criteria as those in Wang et al. [142, 171]. Since bbNIRS system was highly sensitive to motion artifacts, 5 subjects with excessive motion during the experiment were excluded from the analyzed data. After exclusion, a total of 26 young healthy humans (14 males and 12 females, mean ± SD age = 22.4 ± 2.3 years) participated in 5 visits separated by at least 7 days to minimize post-tPBM residual effects. Each participant was subject to (1) Right prefrontal 800-nm tPBM (R800), (2) Right prefrontal 850-nm tPBM (R850), (3) Right prefrontal sham (RS), (4) Left prefrontal 800-nm tPBM (L800), (5) Left prefrontal sham (LS) stimulation and the sequence of these five experiments were randomly assigned to each subject. The Institutional Review Board of the University of Texas at Arlington approved all experimental procedures. All measurements were conducted with informed consent from each participant.

4.2.2 Experiment Setup and Protocol

The original dataset consists of a dual-mode dataset (i.e., bbNIRS and EEG). However, in this study, we used the bbNIRS section of the dataset. The dual-channel bbNIRS system, as described in our previous study [44] was assembled and used to measure the changes in the broadband optical spectrum on the bilateral prefrontal locations of the participants under pre tPBM/sham stimulation (resting-state) and post tPBM/sham stimulations. Δ[HbO] and Δ[CCO] were then quantified based on the absorption and scattering coefficients of major chromophores in the tissue. The experimental setup including the dual-mode bbNIRS and EEG is shown in Figure 4.1(a). Two separate bbNIRS channels, each with a 3-cm source-detector separation, were placed on the subject's forehead before and after tPBM/sham was delivered to the prefrontal location. The bbNIRS holder and fibers were removed during the stimulation period. In the case of right prefrontal stimulation, the right channel (Ch1 in figure 4.1(a)) is the ipsilateral channel and the left channel (Ch2 in figure 4.1(a)) is the contralateral channel and vice versa for the left prefrontal stimulation. This setup enabled us to simultaneously measure the optical spectrum in both ipsilateral and contralateral to the stimulation side. For the detailed setup information see figure 4.1(b) and [44].

The experimental protocol for tPBM and sham experiments is shown in Figure 4.1(c). The total measurement/recording time was 22 minutes, including a 7-min pre-stimulation (rest), an 8-min randomized tPBM/sham, and a 7-min post-stimulation period. The participants were asked to comfortably sit on a sofa chair. Also, they were asked to close their eyes during the whole experimental procedure without falling asleep. For eye protection, participants and experimenters wore a pair of laser-protection goggles during both tPBM and sham stimulation.

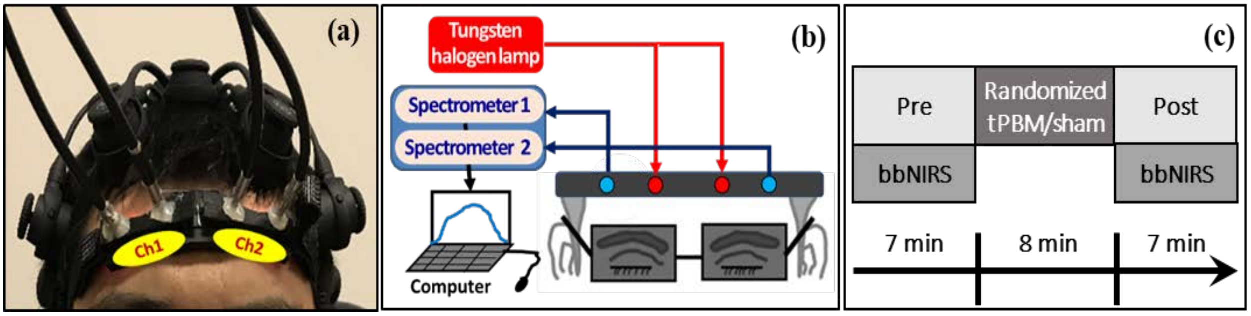

Figure 4. 1 (a) Experiment setup including two channels of bbNIRS on the lateral forehead and EEG cap. The electrophysiological data collected by EEG is not used in this paper. (b) 2-bbNIRS light source, spectrometer, and bundle setup illustration. (c) Protocol for this study consists of 5 visits with 7-minute eyes-closed pre-stimulation, 8 minutes of randomized tPBM (R800, L800, or R850) or sham (RS or LS), and 7-minute post-stimulation. The bbNIRS data is collected pre- and post-stimulation.

In this study, the device/hardware and dosage of tPBM were the same as those published previously [12]. 800 and 850 nm laser parameters for active tPBM and sham are presented in Table 4.1. A sham measurement was performed with the laser device turned on but set to 0.1 W for 8 minutes of stimulation while the laser aperture was sealed with a black-color cap. A power meter was used to confirm that the real output power in presence of the cap was zero.

Table 4. 1 Laser stimulation parameters for active tPBM and sham

Stimulation	**Beam Diameter (mm)**	**Power density (W/cm^2)**	**Delivered Power (W)**	**Time (min)**	**Total Dose (J)**
tPBM (800nm/850nm)	42	0.25	3.5	8	1680
Sham	42	0	0	8	0

4.2.3 Data Analysis

Each 7-minute data collection period consists of 280 time points (i.e., 0.67 Hz) with an optical spectrum recorded in each time point. The recorded spectrum wavelength was 740-1100 nm. However, previous studies have shown that the 780-900 nm band is sufficient to estimate the chromophores' concentration efficiently with a relatively low level of error propagated from noise [172]. Thus, Modified Beer-Lambert law was used in the wavelength of 780-900 nm to estimate Δ[HbO] and Δ[CCO] for each time point [58].

In this study, our main interest was to investigate photobiomodulated prefrontal hemodynamic and metabolic activities in comparison to the baseline. As we demonstrated in our previous study, resting-state hemodynamic and metabolic characteristics (obtained from the pre-stimulation period) investigated in this study are relatively constant among groups of healthy humans. Therefore, the post-stimulation ISO Δ[HbO] and Δ[CCO] metrics can represent the physiological effects of tPBM.

A set of frequency analyses were performed to quantify prefrontal hemodynamic and metabolic ISO activity. As the first step, Δ[HbO] and Δ[CCO] ISO amplitudes (i.e., SA_{HbO}, SA_{CCO}) were calculated on lateral sides over three frequency bands (E/N/M). The second analysis was to estimate the coherence between pairs of $\Delta[HbO]_{right}$, $\Delta[HbO]_{left}$, $\Delta[CCO]_{right}$, and $\Delta[CCO]_{left}$ time series. The physiologically interpretable pairs of these signals are bilateral hemodynamic connectivity ($\mathrm{bCON_{HbO}}$), bilateral metabolic connectivity ($\mathrm{bCON_{CCO}}$), unilateral hemodynamic-metabolic coupling ipsilateral ($\mathrm{uCO_{Ipsi}}$) or contralateral ($\mathrm{uCOP_{Contra}}$) to stimulation.

4.2.3.1 Amplitude and Phase Decomposition

The first set of ISO metrics investigated in this study is the pre- and post-stimulation spectral amplitudes of Δ[HbO] and Δ[CCO] time series. To extract the amplitude and phase of each signal, we used the multi-taper method fast Fourier transform (mtm-fft). In this method, to obtain a frequency spectrum with relatively high resolution and low noise, Slepian sequences were used to taper time series in the time domain followed by the Fourier transform [79, 80]. The decomposed amplitude and phase in this step can be represented as a complex number [13, 15] which was used in the connectivity quantification (see section 4.2.3.2).

To assess the tPBM-induced modulations in hemodynamic and metabolic rhythms, we normalized the post-stimulation amplitudes in respect to pre-stimulation amplitudes by subtracting and dividing the respective 7-min baseline values:

$$\Delta SA_{c,i,j} = \frac{SA_{c,i,j,post} - SA_{c,i,j,pre}}{SA_{c,i,j,pre}} \times 100\% \tag{4-1}$$

Where c denotes the chromophore, namely, HbO and CCO, i represents the frequency band including endogenic (E), neurogenic (N), and myogenic (M) bands, j indicates the stimulation condition, namely, R800, L800, R850, RS, LS, and $SA_{c,i,j,pre}$ and $SA_{c,i,j,post}$ denote the amplitude during the 7-min baseline/pre-stimulation and 7-min post-stimulation period, respectively. Finally, $\Delta SA_{c,i,j}$, is the normalized change in ISO amplitude at each of three frequency bands for different stimulation conditions in percentage. This process was repeated for all four signals of Δ[HbO] and Δ[CCO] on lateral sides. Furthermore, the $\Delta SA_{c,i,j}$ values for 3 tPBM conditions were sham subtracted by subtracting the sham amplitude value (i.e., $\Delta SA_{c,i,sham}$) from the corresponding tPBM (i.e., $\Delta SA_{c,i,tPBM}$) on the corresponding side:

$$\Delta SA_{c,i,ss} = \Delta SA_{c,i,tPBM} - \Delta SA_{c,i,sham} \tag{4-2}$$

The sham-subtracted spectral amplitudes of Δ[HbO] and Δ[CCO] on lateral sides were then tested with a one-sample t-test for each stimulation condition to identify the significant effects of tPBM in each frequency band separately. It is worth noting that one-sample t-test for comparison between sham-subtracted values of tPBM and zero is equivalent to paired t-test for comparison between tPBM and sham group.

4.2.3.2 Hemodynamic and Metabolic Connectivity/Coupling Quantification

Connectivity measures, in principle, express the level by which two signals oscillate synchronously. Different methods are introduced focusing on the amplitude and/or phase of the signals [13, 14]. One of the widely used connectivity measures is coherence, a phase-based frequency-domain analysis that is quantified as a normalized value between 0 and 1. The mathematical representation of coherence for a specific frequency of ω is [13]:

$$coh_{xy}(\omega) = \frac{\left|S_{xy}(\omega)\right|}{\sqrt{S_{xx}(\omega)S_{yy}(\omega)}}, \tag{4-3}$$

where S_{xx} and S_{yy} are the power estimates of signals x and y, and S_{xy} is the averaged cross-spectral density of two time series. These terms are calculated using the complex values obtained from the mtm-fft method (see section 4.2.3.1 and Appendix B.2).

In this study, we quantified the coherence in two time segments separately; namely, baseline (i.e., pre-stimulation) and post-stimulation. The coherence studied in pairs of signals include: (1) $\Delta[HbO]_{Ipsi}$-$\Delta[HbO]_{Contra}$ (i.e. bilateral hemodynamic connectivity, $bCON_{HbO}$), (2) $\Delta[CCO]_{Ipsi}$-

$\Delta[\mathrm{CCO}]_{\mathrm{Contra}}$ (i.e. bilateral metabolic connectivity, $\mathrm{bCON}_{\mathrm{CCO}}$), (3) $\Delta[\mathrm{HbO}]_{\mathrm{Ipsi}}$-$\Delta[\mathrm{CCO}]_{\mathrm{Ipsi}}$ (i.e. ipsilateral prefrontal hemodynamic-metabolic coupling, $\mathrm{uCOP}_{\mathrm{Ipsi}}$), and (4) $\Delta[\mathrm{HbO}]_{\mathrm{Contra}}$-$\Delta[\mathrm{CCO}]_{\mathrm{Contra}}$, (i.e. contralateral prefrontal hemodynamic-metabolic coupling, $\mathrm{uCOP}_{\mathrm{Contra}}$). The obtained values were then divided into the three ISO frequency bands (E/N/M). The tPBM/sham-induced changes in coherence values can be identified by baseline normalization. In this method, since the baseline coherence in some cases are close to zero, the division in the normalization process is not practical. Therefore, the baseline subtraction approach was used for coherence indices (*COH*), as:

$$\Delta COH_{i,j} = COH_{i,j,post} - \mathrm{COH}_{i,j,pre} \tag{4-4}$$

where *i* represents the frequency band including endogenic (E), neurogenic (N), and myogenic (M) bands, *j* indicates the stimulation condition, and $COH_{i,j,pre}$ and $COH_{i,j,post}$ denote the coherence during the 7-min baseline/pre-stimulation and 7-min post-stimulation period, respectively. Finally, $\Delta COH_{i,j}$, is the baseline-subtracted change in ISO coherence at each of three frequency bands for different stimulation conditions. This process was repeated for all four coherence indices between bilateral Δ[HbO], bilateral Δ[CCO], and unilateral Δ[HbO]-Δ[CCO] on lateral sides of the prefrontal cortex. Furthermore, the $\Delta COH_{i,j}$ values for 3 tPBM conditions (i.e., R800, L800, and R850) were sham subtracted by subtracting the sham amplitude value (i.e., $\Delta COH_{i,sham}$) from the corresponding tPBM (i.e., $\Delta COH_{i,tPBM}$) on the corresponding side:

$$\Delta COH_{i,ss} = \Delta COH_{i,tPBM} - \Delta \mathrm{COH}_{i,sham} \tag{4-5}$$

As mentioned above, computed coherence (COH) can be categorized as either bilateral connectivity (bCON) or unilateral coupling (uCOP). The sham-subtracted coherence values were then tested with one-sample t-tests for each stimulation condition to identify the significant effects of tPBM in each frequency band separately.

4.2 Results

This study hypothesized that prefrontal tPBM can alter the spectral amplitude of cortical ISO as well as bilateral hemodynamic and metabolic connectivity and their unilateral coupling of hemodynamic and metabolic rhythms in the resting human forehead. To support this hypothesis, we recruited 26 young and healthy participants (after the exclusion of 5 subjects). The experiment consisted of 5 separate visits, three for active tPBM (i.e., R800, L800, R850) and two for sham stimulation (i.e., RS and LS). During all visits, we took 2-bbNIRS readings during the 7-min pre- and 7-min post-stimulation. ISO amplitude and connectivity/coupling indices were quantified and the changes in response to different laser wavelengths and stimulation sites were studied for each condition.

4.2.3 tPBM-induced Alterations in Spectral Amplitude of Δ[HbO] and Δ[CCO] ISO

As the first step, hemodynamic and metabolic ISO amplitudes in 7-minute pre- and 7-minute post-stimulation temporal segments were calculated for all five stimulation conditions separately. Then, the tPBM-induced changes in Δ[HbO] and Δ[CCO] ($\Delta SA_{c,i,j}$) were computed for five stimulation conditions (see equation (4-1)). Moreover, to better compare the effects of tPBM on amplitude measures, the sham-subtracted values ($\Delta SA_{c,i,ss}$) were quantified over the three ISO bands (E/N/M) as described in equation (4-2).

Figure 4.2(a) shows that compared to sham, all tPBM conditions significantly enhanced ΔSA_{HbO} in the endogenic band, in the prefrontal cortex ipsilateral to the stimulation site. A similar effect was reported in a recent study using a 1064-nm laser [43]. However, the 800-nm tPBM delivered to the right forehead (R800) was the only stimulation with a contralateral effect on ΔSA_{HbO} in this frequency component. Wavelength- and location-dependent modulation of ΔSA_{HbO} is evident in N and M bands as R850 and L800 are the only stimulations with a significant effect on this metric. In addition, as illustrated in figure 4.2(b), the common effect of different tPBM conditions on ΔSA_{CCO} is the decrease of metabolic activity amplitude in the E band on the contralateral side of the stimulation. Furthermore, similar to ΔSA_{HbO}, tPBM-induced ΔSA_{CCO} was wavelength- and location-dependent. This figure shows how an 850-nm laser delivered to the right prefrontal cortex modulated ΔSA_{CCO} in the ipsilateral prefrontal cortex over E and M bands and in the contralateral prefrontal cortex over the N band.

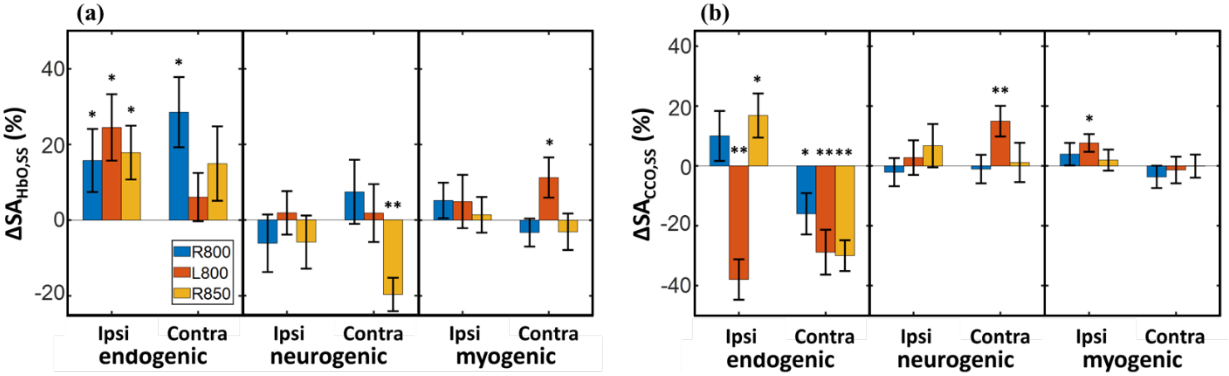

Figure 4. 2 Sham-subtracted tPBM-induced (a) $SA_{HbO,SS}$ and (b) $SA_{CCO,SS}$ (in percent) over the ipsilateral and contralateral sides of the prefrontal cortex for different tPBM conditions, namely, R800, L800, R850 at endogenic (E; 0.005-0.02 Hz), neurogenic (N; 0.02-0.04 Hz), and myogenic (M; 0.04-0.2 Hz) frequency bands. Error bars represent the standard error of the mean (n=26). *: $p<0.05$, **: $p<0.01$ obtained from one-sample t-test.

4.2.4 tPBM-induced Alterations in ISO Coherence of Prefrontal Δ[HbO] and Δ[CCO]

To assess the tPBM-induced alterations in cerebral hemodynamic or metabolic connectivity and hemodynamic-metabolic coupling, as described in 2.3.2, the coherence method was utilized. COH values were calculated for 7-min pre- and post-stimulation periods for all 5 tPBM/sham conditions over three ISO components separately. The stimulation-induced relative change in coherence indices ($\Delta COH_{i,j}$) was then obtained by baseline normalization as described in equation (4-4).

Finally, to evaluate the effect of tPBM on the connectivity and coupling in comparison to the sham stimulation these values were sham-subtracted by the corresponding sham location (see equation (4-5)). The sham-subtracted indices were then tested using one-sample t-tests to distinguish statistically significant effects of different stimulation wavelengths and locations. Coherence indices (COH) can be interpreted as different connectivity/coupling metrics according to the pair of time series that have been examined. As elaborated in 2.3.2, these metrics are: (1) bilateral hemodynamic connectivity ($bCON_{HbO}$), (2) bilateral metabolic connectivity ($bCON_{CCO}$), (3) ipsilateral hemodynamic-metabolic coupling ($uCOP_{Ipsi}$), and (4) contralateral hemodynamic-metabolic coupling ($uCOP_{Contra}$)

According to figures 4.3(a) and (b), 800-nm laser illumination on the right prefrontal cortex is the only stimulation affecting both hemodynamic and metabolic bilateral connectivity by increasing $bCON_{HbO}$ and $bCON_{CCO}$ significantly over the E band. In the case of $bCON_{HbO}$, as illustrated in figure 4.3(a), all tPBM conditions induce a desynchronization between bilateral hemodynamic activities in the M component of ISO. On the other hand, all three tPBM conditions lead to desynchronization of bilateral metabolism in the N frequency band (see figure 4.3(b)). Furthermore, the M band is the frequency band where the effect of the wavelength and location of tPBM on $bCON_{CCO}$ is evident. In this ISO component, Right and left 800 nm stimulation showed opposite effects on $bCON_{CCO}$. The R800 resulted in a decrease in bilateral metabolic connectivity; whereas the L800 boosted this connectivity. On the contrary to 800 nm, 850 nm laser did not induce any alterations to this metric.

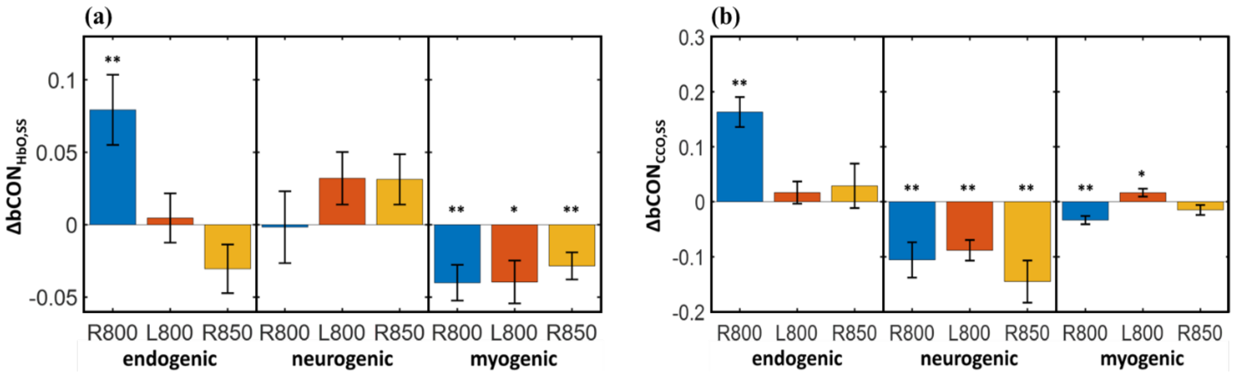

Figure 4. 3 Sham-subtracted tPBM-induced prefrontal (a) $bCON_{HbO,SS}$ and (b) $bCON_{CCO,SS}$ for different tPBM conditions, namely, R800, L800, R850 at endogenic (E; 0.005-0.02 Hz), neurogenic (N; 0.02-0.04 Hz), and myogenic (M; 0.04-0.2 Hz) frequency bands. Error bars represent the standard error of the mean (n=26). *: $p<0.05$, **: $p<0.01$ obtained from one-sample t-test.

Sham-subtracted unilateral hemodynamic-metabolic coupling on ipsilateral and contralateral sides of the prefrontal cortex (i.e., $uCOP_{Ipsi,SS}$ and $uCOP_{Contra,SS}$, respectively) were another set of metrics examined in this study. As shown in Figures 4.4(a) and (b), different stimulation conditions only affected this metric in the prefrontal cortex ipsilateral to the stimulation site. Figure 4.4(a) reveals the fact that the ipsilateral increase in endogenic hemodynamic-metabolic coupling was independent of the wavelength and stimulation site. Moreover, 800nm laser on either side of the prefrontal cortex enhanced the $uCOP_{Ipsi,SS}$ in the M frequency band; whereas, this metric was not altered by R850 laser illumination. Another metric in which the location- and wavelength-dependence of tPBM is evident, is the N band of $uCOP_{Ipsi,SS}$ where R850 tPBM led to no significant alteration in this metric while right and left 800nm tPBM resulted in opposite modulation of this metric. In this sub-band, R800 induced an increase in the ipsilateral coupling; however, L800 tPBM decoupled ipsilateral hemodynamic-metabolic activities.

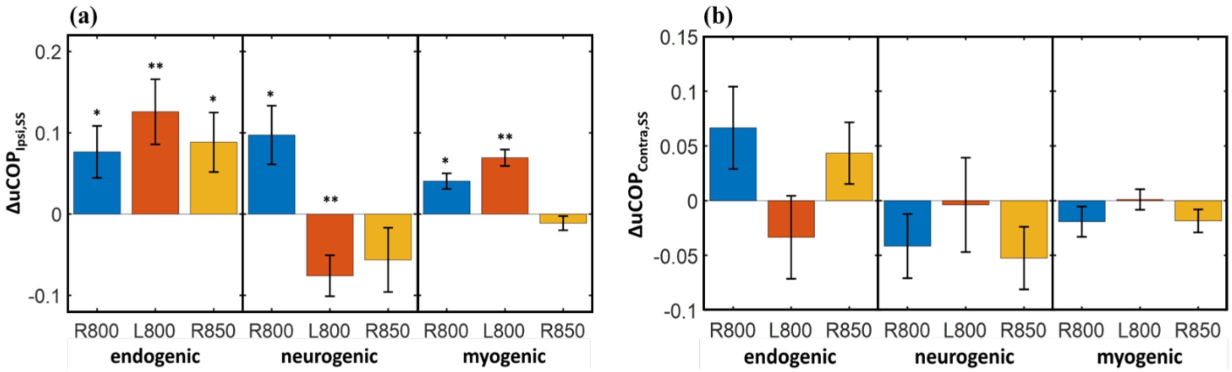

Figure 4. 4 Sham-subtracted tPBM-induced prefrontal (a) $uCOP_{Ipsi,SS}$ and (b) $bCON_{Contra,SS}$ for different tPBM conditions, namely, R800, L800, R850 at endogenic (E; 0.005-0.02 Hz), neurogenic (N; 0.02-0.04 Hz), and myogenic (M; 0.04-0.2 Hz) frequency bands. Error bars represent the standard error of the mean (n=26). *: $p<0.05$, **: $p<0.01$ obtained from one-sample t-test.

4.3 Discussions

NIRS-based methods, as widely-adopted low cost and non-invasive methods of monitoring the hemodynamic and metabolic states of the human brain [136, 151, 152], have faced a limitation in resting-state experiments due to their nature of measuring the relative changes of the chromophores' concentration in the tissue [173]. However, our group recently developed a dual-channel bbNIRS system and computational methodology measuring resting-state bilateral prefrontal metabolic and hemodynamic ISO spectral amplitude and connectivity/coupling as quantifiable absolute values. In previously reported studies, we have shown how these metrics are stable and reproducible among young healthy humans leading to a great potential framework for resting-state bbNIRS studies detecting early-stage neurophysiological disorders [43, 44].

In section 4.2, we demonstrated several hemodynamic and metabolic metrics to quantify prefrontal spectral amplitude, bilateral connectivity, and unilateral coupling of cerebral ISO in the resting human brain. In this section, we would discuss the reported results in section 4.3 regarding the effects of prefrontal tPBM with different wavelengths and stimulation sites on the metrics over lateral prefrontal cortices.

4.3.3 Alterations in ISO Prefrontal SA_{HbO} and SA_{CCO} in Response to Different tPBM Conditions

The significant increase in oxyhemoglobin ISO spectral amplitude (SA_{HbO}) over the endogenic band in response to all three tPBM conditions (figure 4.2(a)) ipsilateral to stimulation, implies that tPBM can significantly excite cerebral hemodynamic activity originated in endothelial oscillations over the stimulation site. This observation, which is independent of laser wavelength and location is in great agreement with several studies showing an increase in Δ[HbO] and its ISO spectral amplitude during and after tPBM with various laser/LED wavelengths and tissues [9, 12, 43, 170, 174]. We have also shown in another study that the upregulation of SA_{HbO} in the endogenic band is because tPBM (specifically 1064nm laser) releases nitric oxide (NO) leading to vessel dilation [175] which seems to be the case for all examined wavelengths and locations in this study. As illustrated in this figure, different stimulation conditions tend to alter contralateral prefrontal cortex SA_{HbO} differently. Specifically, R800 and R850 excited the contralateral cerebral hemodynamic activity sourced in vascular endothelial and smooth muscle cells oscillations, respectively; whereas, L800 inhibited the contralateral hemodynamic activity sourced in inter-neurons oscillations. These observations can be another step towards understanding the mechanism behind different photobiomodulation conditions, especially in cortical regions.

As shown in figure 4.2(b), the other common effect of various tPBM conditions; namely, R800, L800, and R850, was the inhibition of metabolic ISO activity (measured by SA_{CCO}) over the contralateral prefrontal cortex sourced in endothelial cells oscillations. This phenomenon, which was observed in this study for the first time, implies that despite the significantly different behavior of these stimulation conditions over the illumination site, they alter the contralateral metabolic ISO spectral amplitude relatively identically. The outstanding tPBM condition in this figure/metric is the L800. This condition is the only tPBM altering SA_{CCO} from inter-neurons and smooth muscles oscillations where an increase in this metric is evident over ipsilateral and contralateral sites, respectively. On the other hand, the inhibitory effect of this type of tPBM is noticeable in the E band. Finally, the only modulation induced by R850 is the increase in this metric based on vascular endothelial oscillations ipsilateral to the stimulation site. These observations and in particular, the difference between R800 and L800, imply a location-dependent nature of tPBM. Moreover, it reveals the need for a more in-depth study of the laser modulation mechanism behind different wavelengths and stimulation locations. To the best of our knowledge, the cognitive effects of prefrontal tPBM are only reported from right prefrontal stimulation and no significant behavioral effect is reported from left prefrontal stimulation to this date.

It is noteworthy that the effects reported in this paper are based on the temporally averaged metrics of the 7-min post-stimulation compared to 7-min pre-stimulation periods. As reported in other studies, different laser/LED-based tPBM methods have various temporal effects on the hemodynamic and metabolic activities during and post-stimulation. For instance, Pruitt et al. [12] reported a decrease/recovery in upregulated Δ[CCO] immediately after 1064 nm and 850 nm tPBM stop. Thus, the lack of alteration in any of the metrics reported in this study should not be extrapolated to a lack of excitement/inhibition of that activity during stimulation.

4.3.4 Alterations in ISO Prefrontal bCON and uCOP in Response to Different tPBM Conditions

Bilateral connectivity represents the level of synchronization or coherence of oscillations in the concentration of a specific chromophore (i.e., Δ[HbO] or Δ[CCO]) over lateral prefrontal cortices. This functional connectivity reflects whether cerebral activity (i.e., hemodynamic or metabolic) is mainly driven bilaterally/globally or locally [124]. Moreover, a change in this metric in response to a neurological disorder or stimulation can imply how this regulation is disturbed or boosted. In addition, unilateral coupling between hemodynamic and metabolic activities on the same lateral side denotes how the demand (measured by Δ[CCO]) and supply (measured by Δ[HbO]) is regulated in that specific region. Previous studies from our group have revealed a remarkably stable level of this metric in young healthy adults. However, similar to bilateral connectivity, it might be disturbed as a result of irregularities in the supply-demand relationship which leads to neurological impairment. The prefrontal cortex is shown to be closely associated with cognitive functions; thus, many cognitive impairments or disorders are sourced from neurological malfunctioning of this cortical region [125-129].

As shown in figures 4.3(a) and (b), an 800-nm laser delivered to the right prefrontal cortex is the only condition increasing bilateral hemodynamic ($bCON_{HbO}$) as well as metabolic ($bCON_{CCO}$) connectivity in the endogenic band. This enhancement of bilaterally/globally driven hemodynamic and metabolic activity, which was not reported in the study with 1064-nm right prefrontal tPBM [43], is another indication of wavelength- and location-specific effects of tPBM. On the other hand, as illustrated in figure 4.3(a), all three stimulation conditions induce a reduction/desynchronization in bilateral hemodynamic connectivity in the myogenic band. This phenomenon is in agreement with the 1064-nm tPBM [43] indicating a more locally-driven hemodynamic ISO originated from vascular smooth muscle cells oscillations in response to tPBM (independent of wavelength and location). In addition, the same effect is observed in the neurogenic band of $bCON_{CCO}$. This desynchronization is supported by the locally-driven nature of photo-oxidation of CCO in mitochondria [176-178], especially in axon terminals of the cortical neurons where the release of neurotransmitters modulates the oscillation in the neurogenic band. Another indication of the location-related effect of tPBM is the myogenic band of $bCON_{CCO}$ where the right and left 800-

nm lasers resulted in opposite modulation of bilateral metabolic connectivity. In other words, the right 800-nm laser desynchronized the smooth muscle-sourced oscillations of Δ[CCO] and perturbed it towards more locally-driven (more segregated) activity; whereas, the left 800-nm laser boosted the integration of bilateral metabolic activities over prefrontal cortices. This phenomenon can be a result of the information flow direction in resting-state networks. The relationship between tPBM location and modulation is beyond our current knowledge about the tPBM mechanism and requires further investigation.

As the final metric, unilateral hemodynamic-metabolic coupling was only photobiomodulated on the ipsilateral side and no significant changes were observed on the contralateral side of the prefrontal cortex (see figures 4.4(a) and (b)). $uCOP_{Ipsi}$ shows an increase in the endogenic component of ISO indicating an enhanced and more robust oxygen supply-demand relationship in the mitochondrial ATP synthesis cycle mediated by endothelial oscillations. Right and left 800-nm tPBM show the same upregulation of the coupling sourced from vascular smooth muscle oscillations. However, the right 850-nm laser does not modulate the coupling in this frequency band. Finally, another indication of the location-related effect of tPBM is the neurogenic band of $uCOP_{Ipsi}$ where the right and left 800-nm lasers resulted in opposite modulation of unilateral hemodynamic-metabolic coupling. Specifically, the right 800-nm laser boosted the coupling in neurotransmitter-driven oscillations of Δ[HbO] and Δ[CCO]; whereas, the left 800-nm laser decoupled these two activities.

4.3.5 Application of Different tPBM Conditions

Studies have shown that each ISO frequency component is associated with a specific neurophysiological activity in the healthy human brain [115-117, 154]. Therefore, an impaired or diminished infra-slow activity in cerebral hemodynamic and metabolic functions can be identified as a potential indicator for neurological or metabolic disorders. Several studies have shown the relation between this impairment and cardiovascular disease, Alzheimer’s disease, hypertension, and stroke [40, 41, 119].

As suggested by our group in previous studies [43, 44], the proposed resting-state metrics are very stable with a high reproducibility among young, healthy humans. These spectral amplitudes and connectivity/coupling metrics have been suggested as biomarkers for neurophysiological disorders and ongoing studies are focusing on the assessment of these parameters as a framework for early-stage diagnosis of diseases. The abundance of metrics investigated in separate physiologically distinct frequency bands enables us to identify the source of the hemodynamic and/or metabolic impairment in resting-state humans non-invasively. Furthermore, as discussed above, they help to better understand the mechanism behind different types of tPBM. As the ultimate goal, these demonstrated metrics can be utilized to associate the potential tPBM-based treatment to neurological impairment or disorder based on the disease-specific deficiencies in amplitude and connectivity/coupling of hemodynamic and metabolic ISO component.

4.3.6 Limitations and Future Work

First, to obtain sufficient space on the participants’ forehead for the 42-mm diameter laser, we had to remove the bbNIRS holder during the stimulation. Therefore, it took a few minutes (< 5 minutes) to set up the bbNIRS holder and the frontal channels of the EEG cap on the forehead after stimulation and we might have missed some information. Second, we monitored the participants’ movement and EEG signal during measurement for sleepiness and they were asked if they felt drowsy and the excessive sleepy subjects’ data were excluded as outliers. However, the eyes-closed resting state may have caused sleepiness in all subjects, especially in the post-stimulation period. The bbNIRS system used in this study was sensitive to motion and sleepiness may have caused some unintentional movements. Last, our quantified metrics may be potentially contaminated by extracranial layers of the human head, namely, the scalp and skull. Extra short source-detector (S-D) separation channels have been used in task-evoked hemodynamic studies [162-166] to minimize this potential confounding factor. However, no applicable methodology to remove this contaminating noise in fNIRS-based resting-state studies was developed until a recent report [167].

As for future work, modifications in protocol, bbNIRS system, and the developed algorithm are needed to minimize the abovementioned artifacts and noises, especially motion artifacts and extracranial layers contaminations.

4.4 Conclusion

In this study, we hypothesized that the tPBM-induced alterations in the bilateral prefrontal neurophysiological states can be monitored and quantified by the spectral amplitudes of hemodynamic and metabolic activity ipsilateral and contralateral to the stimulation site, bilateral hemodynamic and metabolic connectivity, and unilateral hemodynamic-metabolic coupling ipsilateral and contralateral to the stimulation site. To assess this hypothesis, we implemented 2-channel bbNIRS measurements including 7-min pre- and 7-min post-stimulation at eyes-closed resting state from 26 young healthy participants. The measurement was repeated 5 times for all participants over 5 weeks with different 8-min stimulation conditions, namely, (1) Right prefrontal 800-nm tPBM, (2) Right prefrontal 850-nm tPBM, (3) Right prefrontal sham, (4) Left prefrontal 800-nm tPBM, (5) Left prefrontal sham stimulation.

The 7-min post-stimulation dual-channel bbNIRS measurements enabled us to identify the wavelength- and location-independent tPBM-induced alterations such as (1) excitement of ipsilateral hemodynamic spectral amplitude in E band, (2) inhibition of contralateral metabolic spectral amplitude in E band, (3) decrease of bilateral hemodynamic connectivity in M band, (4) decrease of bilateral metabolic connectivity in N band, and (5) increase of unilateral hemodynamic-metabolic coupling in E band. Furthermore, the reported observations reveal that despite high levels of similarities among different tPBM conditions, there still are differences in some details regarding the wavelength and stimulation site.

Chapter 5

Prefrontal transcranial photobiomodulation alters the physiological network in the prefrontal cortex of healthy adults; *A directed neurovascular, neurometabolic, and metabolic-vascular coupling analysis*

Sadra Shahdadian, Xinlong Wang, Shu Kang, Caroline Carter, Akhil Chaudhari, Hanli Liu[*]

(This chapter is a manuscript to be submitted soon)

5.1 Introduction

Neuronal and vascular activities in the central nervous system (CNS) interact with each other bi-directionally. This interaction, which is mainly observed in dynamic changes in these activities, is referred to as neurovascular coupling (NVC) [179, 180]. The mechanism behind NVC is not fully understood; however, studies have shown that it is mediated by the hemodynamic supply and metabolic demand of oxygen and glucose. In addition, the spontaneous fluctuation in the vasculature wall (i.e., vasomotion) is thought to play a significant role in regulating metabolic and hemodynamic activities by utilizing the chemical and mechanical effects of different regulatory components of the CNS. These components are (1) the endothelial layer of cerebral vasculature and astrocyte glial cells as a part of the blood-brain barrier (BBB), (2) neurons, and (3) smooth muscles on the blood vessel wall [23]. These components were shown to have a modulatory effect in the infra-slow oscillations (ISO, i.e., 0.005-0.2 Hz) of hemodynamic, metabolic, and electrophysiological activities of the cerebral tissue. Three intrinsic frequency components of the infra-slow cerebral hemodynamic rhythms have been found in correspondence to specific physiological/biochemical activity of vascular wall layers [114]. These frequency bands consist of (1) endogenic (0.005-0.02 Hz), neurogenic (0.02-0.04 Hz), and (3) myogenic (0.04-0.2 Hz) [115-

117] rhythms. The endogenic band corresponds to the dilation-contraction cycles in the endothelial layer affected by releasing potent vasoactive factors, such as nitric oxide (NO), free radicals, prostacyclin, endothelium-derived hyperpolarizing factor, and endothelin [118, 119]. Oscillation in releasing vasoactive ions and neurotransmitters from neurons leads to modulation of the vessel dilation-contraction cycles in the neurogenic band [120]. Rhythmic myogenic activity, on the other hand, occurs as a result of the relaxation and contraction of the vascular wall smooth muscle cells [117]. In addition, disturbances in vasomotion have been associated with aging and neurological disorders and diseases such as atherosclerosis [39], cardiovascular disease [40], and Alzheimer's Disease [41]. In other studies published by our group [43, 44], we have shown that vasomotion and its characteristics over the prefrontal cortex at rest are stable and reproducible for young healthy humans.

To assess the coupling between different physiological activities of the brain, a multimodal combination of distinct neuroimaging techniques must be utilized. For instance, electroencephalography (EEG) and magnetoencephalography (MEG) for electrophysiological activity, functional magnetic resonance spectroscopy (fMRI), and functional near-infrared spectroscopy (fNIRS) for hemodynamic activity, and fluorodeoxyglucose positron emission tomography (FDG-PET) and broadband near-infrared spectroscopy (bbNIRS) for metabolic activity. Each of the modalities mentioned above has advantages and limitations. Thus, researchers tend to assemble a low-cost and portable multi-modal combination with adequate temporal, spatial, and spectral resolution.

EEG, as a portable, low-cost neuroimaging technique, is widely used in clinical practice and research studies and can collect electrophysiological signals of the brain with a very high temporal and spectral resolution. In addition, bbNIRS as a more recently developed technique enables researchers to monitor hemodynamic and metabolic activities simultaneously as indirect measures of brain activity. This method utilizes distinct absorption and scattering characteristics of oxygenated hemoglobin (i.e., Δ[HbO]), deoxygenated hemoglobin (i.e., Δ[HHb]), and redox-state cytochrome c oxidase (i.e., Δ[CCO]) to quantify the changes in concentration of these chromophores in the living tissue [130-134]. Studies have demonstrated the requirement of a broadband NIRS system due to the lower concentration of Δ[CCO] in comparison to Δ[HbO] and Δ[HHb] [135, 136, 141, 172]. The relatively slow fluctuations of these metrics help to collect the data with very low-cost NIRS-based equipment even in clinical setups. Investigation of the intertwined behavior of hemodynamic and metabolic ISO activities can be facilitated by assessment of metabolic-vascular coupling (MVC), and utilizing EEG and bbNIRS in parallel opens the door to the assessment of neurometabolic coupling (NMC). Although these different metrics can be assessed separately, they can be observed as a semi-complex physiological network of a specific region in the cerebral cortex where electrophysiological (here, the beta band of EEG), hemodynamic, and metabolic activity are the nodes, and these coupling metrics are the links between them. Furthermore, the topographical functional connectivity of the same physiological ISO activity on different regions of the cerebral cortex can reveal the level by which the neuronal activity, hemodynamics, and metabolism of these regions are correlated.

Topographical connectivity and physiological coupling of two or more time-series can be investigated by directed (effective) or undirected (functional) connectivity measures. Strong uni-directional connectivity between two signals implies an effective relationship from one signal to the other. Several bivariate and multivariate algorithms are developed to unveil the effective connectivity between nodes in a network. It is noteworthy that bivariate measures of connectivity such as cross-correlation, coherence, and Granger causality (GC) only determine the connectivity between an isolated pair of signals from the network at a time; whereas, multivariate measures such as directed transfer function (DTF) and partial directed coherence (PDC) account for the whole multivariate structure of a network using multivariate autoregressive model (MVAR). Due to the shortcomings and pitfalls of each method, more robust methods have been developed such as generalized partial directed coherence (GPDC).

Several non-invasive neural modulations such as transcranial photobiomodulation (tPBM) are shown to alter cerebral electrophysiological, hemodynamic, and metabolic activity of the human brain separately [7, 9, 169]. In addition, improvement in cognitive activity and treatment of different neurological disorders have been reported during and after the employment of low-intensity light-emitting diode (LED) or laser on the human brain, especially on the prefrontal cortex [2, 7, 9, 47, 168, 169]. Furthermore, it is shown that tPBM with different wavelengths and locations can alter the brain's hemodynamic, metabolic, and electrophysiological functional connectivity and MVC at rest [43, 105, 170, 181].

In this study, a dual-mode setup (EEG and bbNIRS) was utilized to assess the topographical effective connectivity between lateral prefrontal hemodynamic and metabolic ISO to identify any directionality between these activities in young healthy human adults at rest. In addition, local HMC was quantified to determine the effective coupling between hemodynamic and metabolic ISO. Furthermore, we constructed two local physiological networks on the lateral prefrontal cortices consisting of a beta band of EEG, Δ[HbO], Δ[CCO] as nodes, and NVC, NMC, and MVC as links. Finally, we quantified the tPBM-induced changes in the abovementioned networks and investigated any possible alterations in information flow among these nodes.

In the end, the results would support the hypothesis that resting-state interactions between electrophysiological, hemodynamic, and metabolic ISO is mostly bi-directionally balanced and they can be significantly altered by tPBM. This modulation can be local or bilateral/global. These observations can be beneficial for further investigation of the mechanism behind NVC, NMC, and MVC as well as location-specific cognitive function improvement or treatment of neurological disorders/diseases based on the modulated metrics.

5.2 Materials and Methods

The dataset used for this study was the same as our previous study (i.e., chapter 3) [44]. 26 healthy human participants were recruited from the local community of the University of Texas at Arlington. They were screened by the same inclusion/exclusion criteria as those in Wang et al. [142, 171]. 4 subjects with excessive motion during the experiment were excluded from the analyzed data. After exclusion, a total of 22 young healthy humans (14 males and 8 females, mean ± SD age = 22.6 ± 2.7 years) participated in 5 visits separated by at least 7 days. In two of these 5 visits, each participant was subject to either left prefrontal 800-nm tPBM (L800) or left prefrontal sham (LS) stimulation and the sequence of these two among the whole 5-visit experiments were randomly assigned to each subject. The Institutional Review Board of the University of Texas at Arlington approved all experimental procedures. All measurements were conducted with informed consent from each participant.

5.2.1 Experiment Setup and Protocol

The dataset consists of a dual-mode dataset, namely, a 2-channel bbNIRS and 19-channel EEG systems. The dual-channel bbNIRS system, as described in our previous study was assembled and used to measure the changes in the broadband optical spectrum on the bilateral prefrontal locations of the participants under pre-tPBM/sham stimulation (resting-state) and post-tPBM/sham stimulations. Δ[HbO] and Δ[CCO] were then quantified based on the absorption and scattering coefficients of major chromophores in the tissue. The experimental setup including the dual-mode bbNIRS and EEG is shown in Figure 5.1(a). Two separate bbNIRS channels, each with a 3-cm source-detector separation, were placed on the subject's forehead before and after tPBM/sham was delivered to the prefrontal location. In the case of left prefrontal stimulation, the left channel (bbNIRS Ch2 and EEG channel Fp1 in figure 5.1(a)) is the ipsilateral channel and the right channel (bbNIRS Ch1 and EEG channel Fp2 in figure 5.1(a)) is the contralateral channel or the left prefrontal stimulation. This setup enabled us to simultaneously measure the optical spectrum in both ipsilateral and contralateral to the stimulation side. For the detailed setup and information see figure 5.1(b).

EEG data were collected during the entire experiment using a 19-channel dry EEG instrument (Quick-20, CGX – Cognionics, CA, US). Each subject wore an EEG cap with 19 electrodes positioned according to the standard 10-20 EEG electrode placement [68]. The recorded EEG time series were directed to a laptop computer via a wireless connection.

The experimental protocol for tPBM and sham experiments is shown in Figure 5.1(c). The total measurement time was 22 minutes, including a 7-min pre-stimulation (rest), an 8-min randomized tPBM/sham, and a 7-min post-stimulation period. The participants were asked to comfortably sit on a sofa chair. Also, they were asked to close their eyes during the whole experimental procedure without falling asleep. For eye protection, participants and experimenters wore a pair of laser-protection goggles during both tPBM and sham stimulation. The bbNIRS holder and fibers were removed and the EEG channels Fp1 and Fp2 were displaced during the stimulation period and were positioned back in place for the post-stimulation period.

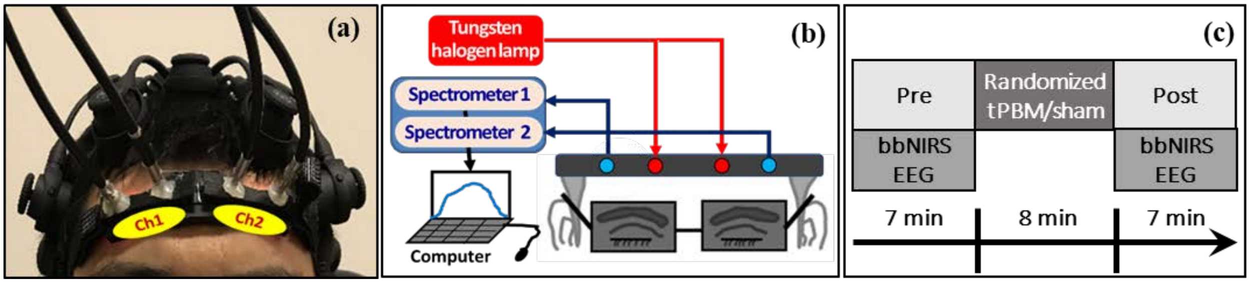

Figure 5. 1 (a) Experiment setup including two channels of bbNIRS on the lateral forehead and EEG cap. The electrophysiological data collected by EEG is not used in this paper. (b) 2-bbNIRS light source, spectrometer, and bundle setup illustration. (c) Protocol for this study consists of 5 visits with 7-minute eyes-closed pre-stimulation, and in two visits followed by 8 minutes of randomized tPBM (L800) or sham (LS), and 7-minute post-stimulation. The bbNIRS and EEG data are collected pre- and post-stimulation.

In this study, the device/hardware and dosage of tPBM were the same as those published previously [12]. 800 nm laser with a beam diameter of 42 mm and power density of 0.25 W/cm^2 was utilized for 8 minutes to provide a total dose of 1680 J. A sham measurement was performed with the laser device turned on but set to 0.1 W for 8 minutes of stimulation while the laser aperture was sealed with a black-color cap. A power meter was used to confirm that the real output power in presence of the cap was zero.

5.2.2 Overview of data processing steps

Several steps are required to quantify the topographical connectivity and physiological coupling of the recorded biological signals. Because the data processing and analysis procedures included multiple steps in this study, we outline a flow chart of these steps in figure 5.2 to better guide the reader through them easily. In summary, these steps consist of (1) bbNIRS raw spectral data preprocessing and quantification of Δ[HbO] and Δ[CCO] time series, (2) EEG data preprocessing, (3) EEG data down-sampling, (4) Topographical (i.e., bilateral) directed hemodynamic and metabolic connectivity calculation, (5) Neurovascular, neurometabolic, and metabolic-vascular coupling quantification and physiological network construction, (6) tPBM-induced modulations in connectivity, coupling, and physiological network.

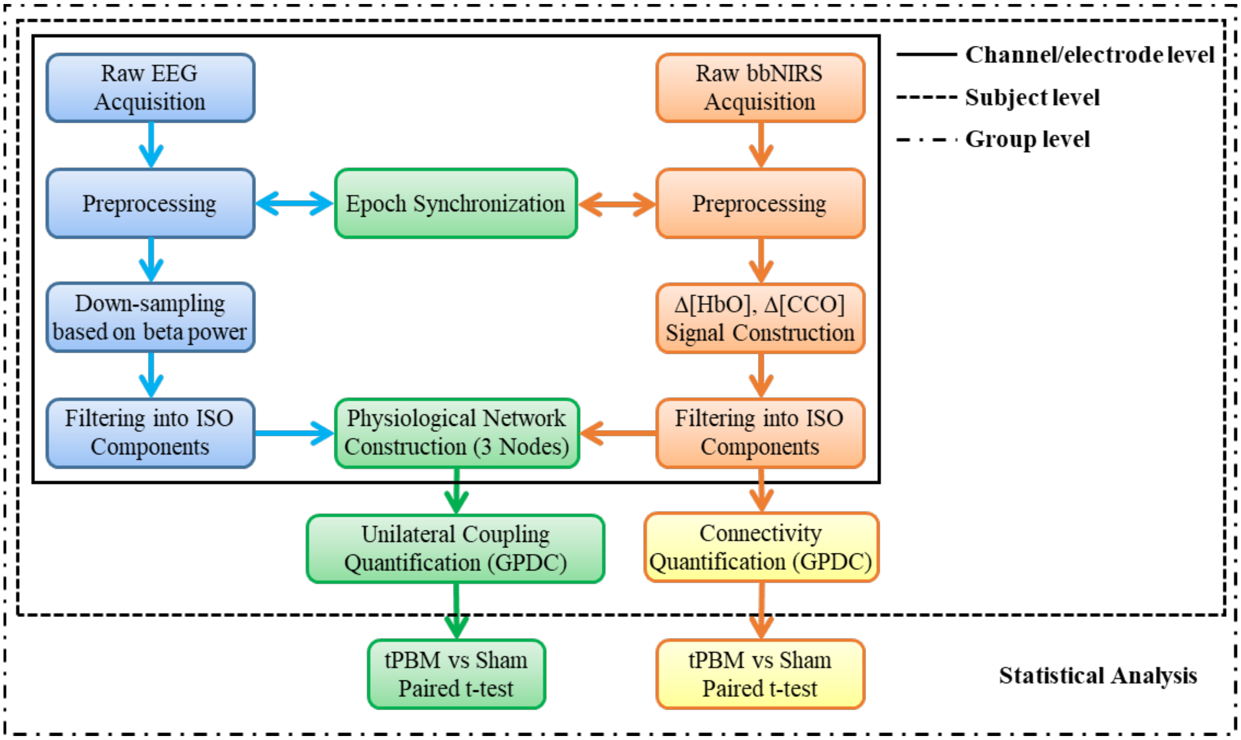

Figure 5. 2 A data processing flow chart, including steps for (1) EEG data analysis (blue boxes), (2) bbNIRS data analysis (orange boxes), (3) bilateral hemodynamic and metabolic connectivity (yellow boxes), and (4) integrated EEG-bbNIRS data analysis including epoch synchronization and unilateral physiological network analysis (green boxes).

5.2.3 bbNIRS data preprocessing

Each 7-minute data collection period consists of 280 time points (i.e., 0.67 Hz) with an optical spectrum recorded in each time point. The recorded spectrum wavelength was 740-1100 nm. However, previous studies have shown that the 780-900 nm band is sufficient to estimate the chromophores' concentration efficiently with a relatively low level of error propagated from noise [172]. Modified Beer-Lambert law then was used to estimate Δ[HbO] and Δ[CCO] for each time point [58, 135, 136], and the time series of Δ[HbO] and Δ[CCO] was constructed. These time series were then filtered into the three ISO components (i.e., E/N/M).

5.2.4 EEG data preprocessing

EEGLAB, an open-source software package based on MATLAB, was used to pre-process the EEG data. First, the 19-channel raw EEG data was band-pass filtered from 1 to 55 Hz. Second, each EEG time series was re-referenced to the voltage average over all the 19 channels. Next, to remove noise and artifacts [71, 72] such as eye movements, saccades, and jaw clenching, independent component analysis (ICA) [73, 74] was used, and finally, artifact subspace reconstruction (ASR) was used to reconstruct bad epochs using principal component analysis (PCA) [182]. Then, clean EEG signals from electrodes Fp1 and Fp2 were selected and band-pass filtered in the 13-30 Hz range to obtain beta-band temporal activity in the prefrontal area.

5.2.5 Multivariate autoregressive (MVAR) model and GPDC

As mentioned in the introduction, MVAR enables us to take into account all the links (i.e., interactions) between nodes in a network simultaneously. In this method, for a *k*-node process of X(t) we have:

$$X\left(t\right)=\left(X_1\left(t\right),X_2\left(t\right),\ \ldots,X_k\left(t\right)\right)\ , \tag{5-1}$$

The model takes the form:

$$X(t)=\sum_{j=1}^{p}A(j)X(t-j)+E(t)\ , \tag{5-2}$$

where *A* is the *k* × *k*-sized matrix of coefficients, *E*(*t*) is a prediction error vector of size *k*, and p is the order of the model. Generalized partial directed coherence (GPDC) for frequency *f* then can be calculated as:

$$GPDC_{j,i}(f)=\frac{A_{ij}(f)}{\sum_{i=1}^{k}\left|A_{ij}(f)\right|^2} \tag{5-3}$$

where $A_{ij}(f)$ is an element of $A(f)$ – a Fourier transform of MVAR model coefficients $A(t)$ [183]. Thus, the output adjacency matrix is a $k \times k$-sized nonsymmetrical matrix with elements of $\text{GPDC}_{j,i}$ where the element in column j and row i denotes the effective (directed) connectivity from node j to node i.

5.2.5 EEG data down-sampling

In order to integrate two datasets with significantly different sampling frequencies (i.e., 0.67 Hz and 500 Hz for bbNIRS and EEG, respectively), EEG data was down-sampled to match the sampling rate of bbNIRS data as was done in [184]. Therefore, the EEG data were segmented into 1.5-s epochs (i.e., the data acquisition rate of the bbNIRS signal) and the power spectrum density (PSD) of the EEG signal was obtained for each epoch using a single-tapered fast Fourier transform. The area under the curve of PSD in the beta frequency band (13-30 Hz) was calculated and used to construct a time series of EEG beta power with 1.5-s temporal resolution (0.67 Hz, 280 time points). This down-sampled EEG time series was then filtered into the main ISO band (i.e., 0.005-0.2 Hz). Figure 5.3 is a schematic illustration of the down-sampling process of the EEG data.

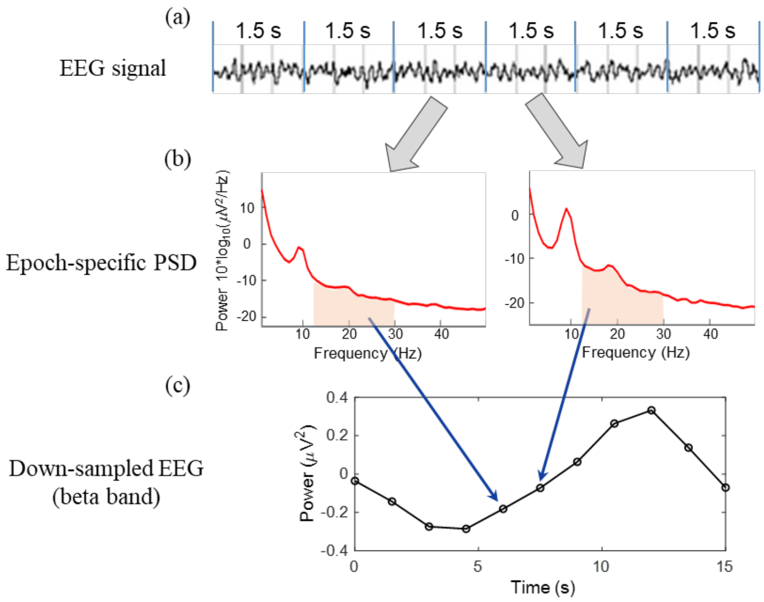

Figure 5. 3 Schematic illustration of the process for down-sampling EEG data. (a) EEG time series segmented in 1.5-s epochs. (b) power spectral density (PSD) obtained from each epoch. The area under the curve in the beta band is calculated and used to construct (c) down-sampled EEG time series.

5.2.6 Topographical directed hemodynamic and metabolic connectivity

To investigate the effective interaction between similar physiological signals over the bilateral prefrontal cortex (i.e., $\Delta[\mathrm{HbO}]_{\mathrm{right}}$ - $\Delta[\mathrm{HbO}]_{\mathrm{left}}$, $\Delta[\mathrm{CCO}]_{\mathrm{right}}$ - $\Delta[\mathrm{CCO}]_{\mathrm{left}}$) over the frequency band of ISO, multivariate autoregressive (MVAR) model followed by GPDC was used. Based on the Akaike information criterion (AIC), a method to evaluate the goodness of fit, the order of the MVAR model was set to 1. The MVAR model followed by GPDC was used to quantify the bilateral connectivity between the same signal in presence of other physiological signals.

5.2.7 physiological network construction

In order to investigate the causal interaction between different physiological representations of local brain activity (i.e., left or right prefrontal cortex), hemodynamic, metabolic, and electrophysiological signals were integrated to construct a 3-node physiology network consisting of (1) Δ[HbO], (2) Δ[CCO], and (3) EEG beta band. To obtain the links connecting these nodes, GPDC was calculated for all 3×3 possible connections, and the physiological network was constructed for each ISO frequency band.

5.2.8 tPBM-induced modulation in metabolic-vascular and physiological network

In this study, our primary interest was to investigate the photobiomodulated prefrontal physiological network in comparison to the baseline. Therefore, the post-stimulation MVC and physiology network metrics compared to the control group (sham stimulation) can represent the physiological effects of tPBM. This comparison consists of baseline subtraction and statistical testing. Baseline subtraction of post-stimulation $\mathrm{GPDC}_{j,i}$ values for MVC and physiological network was performed as expressed below:

$$\Delta GPDC^{f}_{j,i} = GPDC^{f}_{j,i,post} - \mathrm{GPDC}^{f}_{j,i,pre} \tag{5-4}$$

where f is the ISO frequency component (i.e., E/N/M).

The obtained $\Delta GPDC_{j,i}$ was then statistically examined using paired t-test for left 800-nm laser (L800) vs left sham (LS).

To simplify the representation of the physiological network matrix, sham-subtracted values of unilateral coupling were calculated based on the following equation:

$$\Delta GPDC^{f}_{j,i,ss} = \Delta GPDC^{f}_{j,i,tPBM} - \Delta \mathrm{GPDC}^{f}_{j,i,sham} \tag{5-5}$$

These values were then utilized to illustrate the difference between sham and active tPBM stimulation conditions.

The obtained values from the GPDC method are grouped into two main categories: bilateral (topographical) connectivity (i.e., bCON) between the same signals from different channels, and unilateral (physiological) coupling (i.e., uCOP) between different signals recorded from the same channel/electrode.

5.3 Results

5.3.1 Resting-state prefrontal metabolic-vascular network

As described in materials and methods and illustrated in figure 5.2 (orange boxes), the 2-channel bbNIRS data recorded for each subject was used to estimate two pairs of hemodynamic and metabolic signals, namely, $\Delta[\mathrm{HbO}]_{\mathrm{right}}$, $\Delta[\mathrm{CCO}]_{\mathrm{right}}$, $\Delta[\mathrm{HbO}]_{\mathrm{left}}$, and $\Delta[\mathrm{CCO}]_{\mathrm{left}}$ from 110 measurements (i.e., 22 subjects and 5 visits for each)

These signals were then used to construct the metabolic-vascular network for each ISO frequency band in the resting state consisting of 4 signals as the nodes (yellow boxes in figure 5.2). As shown in figure 5.4, this network assesses the level of bilateral connectivity for HbO and CCO as well as the unilateral coupling of HbO-CCO on each side of the prefrontal cortex. This figure consists of three main boxes for E/N/M frequency bands each of which includes the color-coded adjacency matrix and graphical representation of the network. As illustrated in this figure, bilateral hemodynamic connectivity plays a prominent role in this network's overall ISO frequency bands; especially, in the myogenic band.

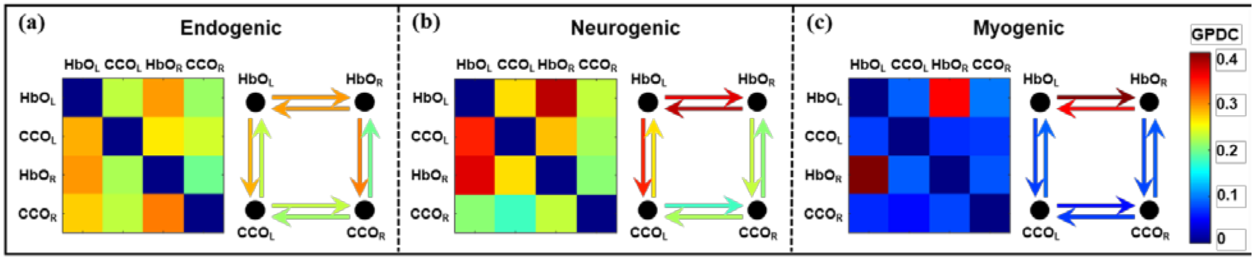

Figure 5. 4 Adjacency matrices and graphical illustration of resting state metabolic-vascular network on the prefrontal cortex obtained from 2-bbNIRS. Three boxes represent (a) endogenic, (b) neurogenic, and (c) myogenic components of ISO. The nodes in the network are $\mathrm{HbO_{left}}$, $\mathrm{CCO_{left}}$, $\mathrm{HbO_{right}}$, and $\mathrm{CCO_{right}}$.

A notable unilateral HbO-CCO coupling is also observed in endogenic and neurogenic bands where HbO activity is leading CCO. However, no significant metabolic connectivity or metabolic-vascular coupling is observed in the myogenic band.

Figure 5.5 represents the bilateral connectivity of HbO and CCO, extracted from the adjacency matrices represented in figure 5.4. This figure helps to investigate the directionality between lateral sides of PFC in the resting state.

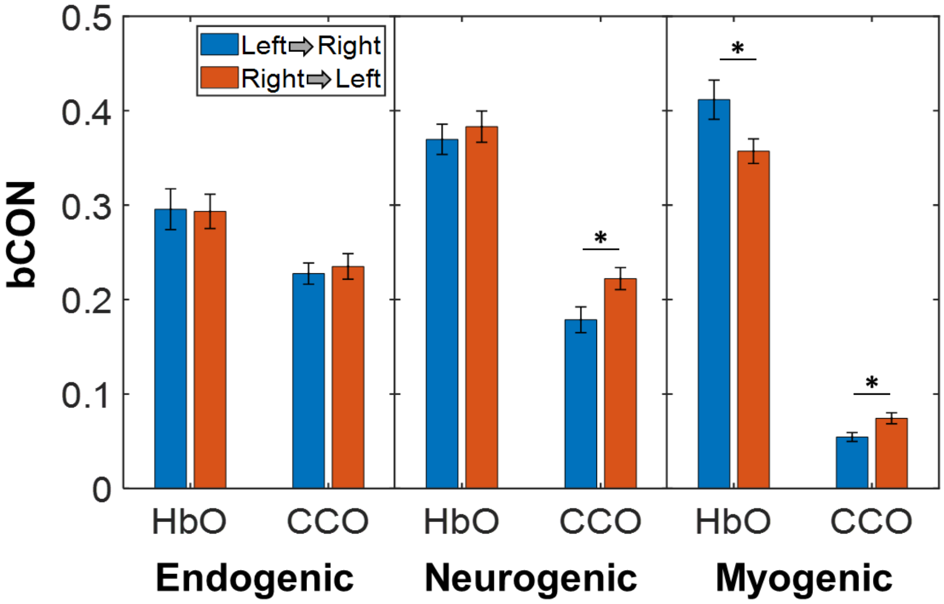

Figure 5. 5 Directed bilateral hemodynamic and metabolic connectivity between left and right prefrontal cortex in endogenic, neurogenic, and myogenic bands. Error bars represent the standard error of the mean. *: p-value < 0.05.

As illustrated in this figure, the directed connectivity from CCO_{right} to CCO_{left} is statistically higher than in the opposite direction in neurogenic and myogenic bands. On the other hand, HbO_{left}-HbO_{right} shows a higher GPDC index than HbO_{right}-HbO_{left}.

5.3.2 Resting-state unilateral physiological network

3 different physiological signals, namely, HbO, CCO, and EEG collected from the same prefrontal region (i.e., left or right PFC), were used to construct the physiological network (PN) over that region in different ISO frequency bands utilizing the MVAR model followed by GPDC. As illustrated in figure 5.6, the myogenic band, compared to the other bands, represents significantly lower levels of coupling between cerebral hemodynamic, metabolic, and electrophysiological

activities on both lateral PFC. On the other hand, high levels of coupling between all three components are observed in the endogenic band denoting a closely coupled activity between three nodes of the network on both lateral PFC. In addition, the physiological network reveals a highly synchronized HbO-CCO and HbO-EEG in the neurogenic component of ISO, while the CCO-EEG causal coupling is comparably low in this frequency band over both lateral PFC.

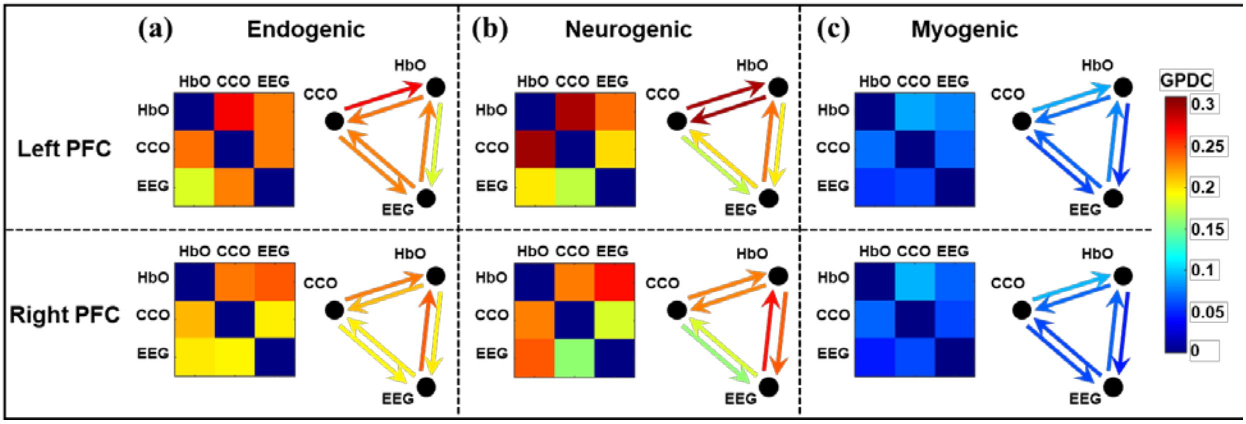

Figure 5. 6 Adjacency matrices and graphical illustration of resting state physiological network on the prefrontal cortex obtained from dual-mode 2-bbNIRS and EEG dataset. Three columns represent (a) endogenic, (b) neurogenic, and (c) myogenic components of ISO over left and right PFC. The nodes in the network are HbO, CCO, and EEG.

5.3.3 tPBM-induced directed alterations in bilateral metabolic and hemodynamic connectivity

As elaborated above, one of the major aims of this study was to investigate the effects of left frontal 800-nm laser stimulation on bilateral metabolic and hemodynamic connectivity. To quantify this effect, as described in equation (5-4), baseline normalized values of GPDC (i.e., ΔGPDC) obtained from the metabolic-vascular network were calculated for each frequency band. Changes in directional bilateral connectivity for HbO and CCO (i.e., $\Delta bCON_{HbO}$ and $\Delta bCON_{CCO}$) were then extracted and represented in figure 5.7. As shown in this figure, left prefrontal stimulation with an 800-nm laser induces an increase in directed hemodynamic and metabolic connectivity from left to right PFC in the endogenic band, accompanied by a decrease in the same metric in the neurogenic band. The other significant effect of tPBM in the endogenic band is the decrease in $\Delta bCON_{HbO}$ from right PFC to left compared to sham stimulation. In addition, an increase in left to right $\Delta bCON_{HbO}$ and right to left $\Delta bCON_{CCO}$ is observed.

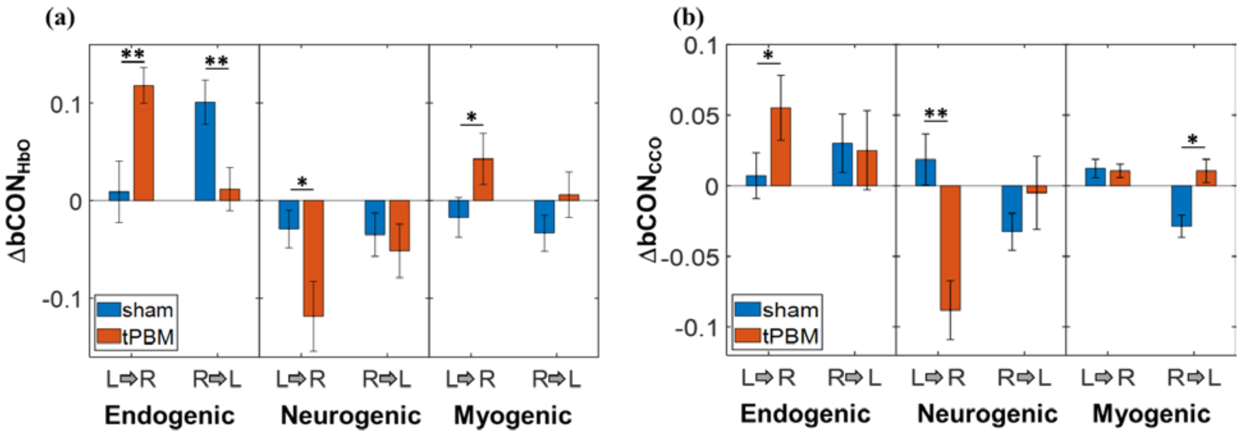

Figure 5. 7 Changes in directed bilateral (a) hemodynamic and (b) metabolic connectivity between left and right prefrontal cortex in endogenic, neurogenic, and myogenic bands in response to left prefrontal 800-nm tPBM. Error bars represent the standard error of the mean. *: p-value < 0.05, **: p-value < 0.01.

5.3.4 tPBM-induced directed alterations in unilateral physiological network

Following equation (5-5), the sham-subtracted values of $\Delta GPDC$ (i.e., $\Delta GPDC_{ss}$) were calculated and represented as color-coded adjacency matrices in figure 5.8. Since no significant connectivity/coupling except $bCON_{HbO}$ was identified in the myogenic band, and this band does not represent any electrophysiological-related phenomenon, only $\Delta GPDC_{ss}$ for endogenic and neurogenic bands are reported in this figure. In addition to adjacency matrices, a graphical representation of the network is provided to help visualize changes in the network by color-coding statistically significant links (i.e., uCOP). This figure shows an increase in directed coupling from HbO and CCO to EEG in the endogenic band over ipsilateral PFC (i.e., left), while there is a significant decrease in the bidirectional coupling of HbO and CCO. In addition, left PFC shows an increased bidirectional coupling between electrophysiological and hemodynamic activity in the neurogenic band, while the leading effect of EEG and HbO on CCO has a significant reduction.

On the contralateral side of PFC, only a decrease in effective coupling is observed, namely, a reduction of effective coupling from HbO to CCO in the endogenic band, as well as a decrease in this metric from CCO to EEG, and bidirectional coupling of CCO and HbO.

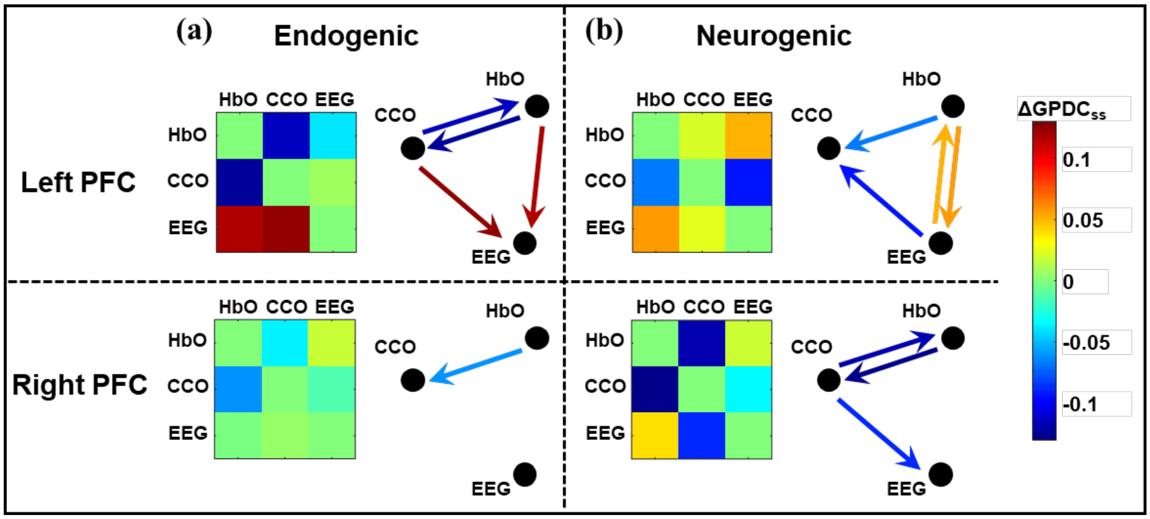

Figure 5. 8 Adjacency matrices and graphical illustration of changes in unilateral coupling in the physiological network on the prefrontal cortex in response to left 800-nm tPBM. Three columns represent (a) endogenic and (b) neurogenic components of ISO over left and right PFC. The nodes in the network are HbO, CCO, and EEG. Drawn links are the $\Delta uCOP_{j,i,ss}$ in which $\Delta uCOP_{j,i,tPBM}$ and $\Delta uCOP_{j,i,sham}$ return a p-value less than 0.05.

5.4 Discussion

5.4.1 Resting-state prefrontal metabolic-vascular network

Figure 5.4 illustrated the resting state metabolic-vascular network constructed from ISO hemodynamic and metabolic activity on lateral sides of PFC obtained from 110 measurements from 22 young healthy adults. The strength of links in directed connectivity in these networks denotes the level by which the activity of a node (signal) affects the activity of another. The links in the metabolic-vascular network in each ISO frequency band consist of directed (1) bilateral hemodynamic connectivity ($bCON_{HbO}$), (2) bilateral metabolic connectivity ($bCON_{CCO}$), (3) unilateral metabolic-vascular coupling on the left PFC (MVC_{Left}) and (4) unilateral metabolic-vascular coupling on the right PFC (MVC_{Right}).

As reported in figure 5.4, $bCON_{HbO}$ is the strongest link in all three frequency bands, especially in the myogenic band where no other strong link is observed between other nodes. This phenomenon is in agreement with the previously studied sources of each frequency band. For instance, the fluctuation in the myogenic band is mediated by the smooth muscle of the vasculature where the relaxation-contraction cycles are mainly controlled by hormones in the bloodstream and autocrine/paracrine agents [185] and the effect of local CCO concentration in the neurons are minimally affecting the smooth muscle oscillations. Smooth muscle cells are also responsible for the contraction and dilation of cerebral vessels to maintain blood pressure in a specific range; thus, the contraction-relaxation cycles in different regions of the brain are highly synchronized. In contrast to the myogenic band, $bCON_{HbO}$ in the endogenic and neurogenic bands are accompanied by comparable MVC on both lateral PFC. On the other hand, $bCON_{CCO}$ is at a minimal level in each network which is in agreement with the local nature of CCO activation in neurons. The levels of MVC in endogenic and neurogenic bands are in a similar range where the unilateral information flow is mainly from HbO to CCO. The unilateral coupling of HbO and CCO will be discussed in detail in the physiological network analysis where the effect of electrophysiological activity is considered in the network construction.

To better understand the directionality of the bilateral hemodynamic and metabolic connectivity, $bCON_{HbO}$ and $bCON_{CCO}$ values were extracted from figure 5.4 and represented in figure 5.5. In this figure, the effective connectivity of $bCON_{HbO}$ and $bCON_{CCO}$ from left PFC to right PFC is statistically compared to the opposite direction. As shown in this figure, no statistically significant differences are observed in $bCON_{HbO}$ over endogenic and neurogenic bands. However, the effective connectivity in the myogenic band from HbO_{left} to HbO_{right} is significantly higher than in the opposite direction. In addition, $bCON_{CCO}$ has no statistically significant directionality in the endogenic band; whereas, the causal connectivity in the neurogenic and myogenic bands from CCO_{right} to CCO_{left} is significantly higher than in the opposite direction. To the best of our knowledge, the observed directionalities in the resting state are being reported for the first time, and no similar study is done to assess directed hemodynamic and metabolic connectivity between bilateral PFC.

5.4.2 Resting-state prefrontal unilateral physiological network

Figure 5.6 illustrated the resting state physiological network constructed from ISO hemodynamic, metabolic, and electrophysiological activity on lateral sides of PFC obtained from 110 measurements from 22 young healthy adults. The links in the physiological network in each ISO frequency band over each lateral PFC consist of directed (1) unilateral neurovascular coupling (NVC), (2) unilateral neurometabolic connectivity (NMC), and (3) unilateral metabolic-vascular coupling (MVC).

As shown in figure 5.6, there is a balanced coupling between all three nodes of the physiological network in the endogenic band in the resting state. This observation is in agreement with the physiological source of the endogenic band oscillation where the contraction and relaxation of the endothelial layer of the vessel wall, as a prominent component of the blood-brain barrier, regulates the hemodynamics and metabolism as well as neural activity. In other words, the oxygen supply-demand balance between neural activity, metabolism, and hemodynamics is mainly controlled in this frequency band bidirectionally.

The neurogenic band, on the other hand, reflects the ISO of vasculature in response to the neural stimulations via neurotransmitters. The neurogenic physiological network represented in figure 5.6(b) also denotes a high level of NVC and MVC. Furthermore, directed connectivity from EEG to HbO and from EEG to CCO is observed and the lowest effective coupling is corresponding to the link from CCO to EEG in this frequency band over both lateral PFCs. These observations reveal a directed information flow from electrophysiological activity to the highly coupled metabolism and hemodynamics.

As expected from the definition of the myogenic band, and seen in figure 5.6(c), the strength of coupling among all nodes of the physiological network is significantly lower than the other frequency bands. This phenomenon, as justified in the last section, emphasizes the fact that the dominant component of connectivity/coupling in this frequency band is the very robust bilateral connectivity between hemodynamic activity on the lateral PFCs originating from the smooth muscle contraction-relaxation cycles, and these oscillations are not affected by local electrophysiological and/or metabolic activity of the cerebral cortex.

5.4.3 Alterations in bilateral metabolic and hemodynamic connectivity, modulated by prefrontal tPBM

Baseline-normalized values of bilateral connectivity (see equation (5-4)) for two groups (i.e., sham vs tPBM, n=22) are represented in figure 5.7. As shown in figures 5.7(a) and 5.7(b), the left prefrontal 800-nm laser induces an increase in effective connectivity of both HbO and CCO from the stimulation site (i.e., left PFC) to the contralateral side (i.e., right PFC) in the endogenic band compared to the sham group. This observation is in agreement with previous studies reporting the local and global (bilateral) effects of prefrontal tPBM on connectivity and spectral amplitude of HbO and CCO. The other modulation in the endogenic band is the decrease in the $\Delta bCON_{HbO}$ from right to left sides. This phenomenon reveals a significant disturbance in the balance of bilateral information flow between ISO of endothelium leading to a highly uni-directional effective connectivity from the ipsilateral side of the tPBM to the contralateral side.

The effect of left frontal tPBM on the bilateral hemodynamic and metabolic connectivity in the neurogenic band is similar, where the causal connectivity from left PFC to right PFC significantly decreases in response to left tPBM compared to sham. Since the neurogenic band mainly represents the neurally-regulated oscillations of the blood vessel wall, and consecutively blood flow and HbO concentration, changes in this frequency band reveal an electrophysiologically-induced alteration in the oscillations of HbO and CCO. The decline in effective connectivity from left to right HbO and CCO highlights the fact that the hemodynamic and metabolic activity on the contralateral PFC is less influenced by left HbO and CCO and mediated more by a neural regulatory measure. A more detailed investigation of this phenomenon can is done in the next section.

The myogenic frequency band, in addition, shows a boosted directionality in bilateral hemodynamic and metabolic connectivity where an increase in the left to right $bCON_{HbO}$ and right to left $bCON_{CCO}$ is observed. This phenomenon emphasizes the effect of tPBM on strengthening the natural uni-directional connectivity between hemodynamics and metabolism activity mediated by the oscillations in smooth muscles in the cerebral vasculature.

5.4.4 Alterations in the unilateral physiological network, modulated by prefrontal tPBM

Sham- subtracted values of the physiological network (i.e., $\Delta GPDC_{ss}$, see equation (5-5)) constructed from endogenic and neurogenic hemodynamic, metabolic, and electrophysiological activity on lateral sides of PFC obtained from 22 young healthy adults were reported in figure 5.8. The links in the physiological network in each ISO frequency band over each lateral PFC consist of directed (1) unilateral neurovascular coupling (NVC), (2) unilateral neurometabolic connectivity (NMC), and (3) unilateral metabolic-vascular coupling (MVC). This figure clearly shows that the major effect of tPBM on the physiological network on the ipsilateral side of the stimulation is in the endogenic band where CCO and HbO lose coupling and both lead EEG more strongly in parallel to each other. This observation supports the current hypothesis that tPBM stimulates both hemodynamic and metabolic activity [43]. The former is done by releasing nitric oxide (NO) which leads to alteration in contraction-dilation of the endothelial layer [186] and the latter is done by photo-oxidizing cytochrome c oxidase in the neurons' mitochondria [174]. Since the tPBM is acting on the HbO and CCO activity independently, the coupling between these two signals decreases. However, each of them plays a more robust role in the modulation of the electrophysiological activity of the neurons (EEG).

The reduction in MVC is observed in both frequency bands over both channels, especially from HbO to CCO which can be interpreted as a perturbation in the balance of information flow between hemodynamic and metabolic activity.

In the neurogenic band, however, the NVC is enhanced bidirectionally, meaning that the information flow between neuronal and hemodynamic activity is significantly increased while metabolism is less mediated by hemodynamics and electrophysiological activity (the CCO is activated independently from HbO and EEG). A similar effect of left prefrontal tPBM on NMC and MVC is observed over the contralateral side of the stimulation (i.e., right PFC) where MVC and NMC are significantly decreased bidirectionally and from CCO to EEG, respectively.

5.4.5 Combination of dual-mode data and MVAR model-based connectivity analysis

In this study, by utilizing a dual-mode data collection setup and a multivariate connectivity measure that focuses only on the direct connectivity of the signals, we could identify and quantify directed (effective) connectivity between different aspects of the cerebral cortex as potential features of resting-state activity. These features can be further investigated in different groups of interest. For instance, the effect of age, gender, neurological disorders, or diseases on the proposed networks can be assessed. The methodology developed in this study also opens the door to identifying potential biomarkers for early-stage diagnosis of neurophysiological diseases such as dementia, Alzheimer’s disease, etc. Furthermore, this methodology helped us to evaluate the separately hypothesized mechanisms of action of tPBM in one semi-complex network.

5.4.6 Limitations and future works

First, the relatively low sampling frequency of the bbNIRS data and short data collection duration prevented us to achieve a high-frequency resolution, which may lead to low accuracy in spectral amplitude and coherence in the low-frequency range, especially in the endogenic band. Second, our bbNIRS system was sensitive to motion; the eyes-closed resting-state protocol may have caused the sleepiness of the participants during the measurements. Last, our quantified results or metrics may be potentially contaminated by extracranial layers of the human head. It is known that fNIRS signals obtained over the scalp of the human participants are contaminated by the extracranial layers, namely, the human scalp and skull. To minimize this potential confounding factor, extra optical channels of fNIRS with a short source-detector (S-D) separation (commonly ~0.8-1.2 cm) have been used for systemic noise removal in task-evoked hemodynamic studies [162-166], where a cortical region was activated by stimulating tasks. However, most fNIRS-based studies for the quantification of resting-state functional connectivity (RSFC) did not develop an appropriate methodology to remove this confounding effect until a recent report, which confirmed that RSFC can be quantified more accurately with a short S-D reading correction than without correction [167].

As for future work, to enable a longer and less-artifact recording from the human brain, modifications or improvements are needed on the bbNIRS setup, measurement protocol, and the computational methods for reducing movement artifacts and systemic/physiological noises. Also, it is necessary to consider the implementation of short-distance channels in bbNIRS for removing possible contamination of extracranial layers to the determined/interpreted results. The networks developed in this exploratory study are considered the first step in the investigation of physiological network quantification. These networks can be extended to other EEG frequency bands and the quantified features of physiological coupling can be assessed further to propose potential biomarkers to diagnose different neurological disorders.

5.5 Conclusion

In this study, we hypothesized that prefrontal cortical connectivity and coupling of ISO in the resting human brain can be quantified using dual-mode (i.e., 2-bbNIRS and EEG) and may serve as features to reflect brain state. To prove this hypothesis, we implemented the dual-mode setup and performed bilateral, prefrontal, 7-min measurements at the eyes-closed resting state from 22 young and healthy participants, repeatedly 5 times over 5 weeks. The measured time series were analyzed to detect cerebral hemodynamic, metabolic, and electrophysiological ISO at rest. MVAR model followed by GPDC was utilized to construct the bilateral metabolic-vascular and unilateral physiological networks. We defined and investigated several ISO-specific metrics, including bilateral connectivity for both hemodynamic and metabolic activity, and unilateral MVC, NVC, and NMC at rest. The essential rationale of the proposed biomarkers was that the success of separating the three ISO components of prefrontal hemodynamics and metabolism would enable us to detect and distinguish neurophysiological disorders (e.g., age-related cognition impairments, cardiovascular disease, Alzheimer’s disease, hypertension, and stroke) based on sources of impaired or abnormal signals (e.g., endothelium, inter-neuron, or smooth muscle).

The 7-min post-stimulation dual-modality measurements enabled us to identify the ISO frequency-specific tPBM-induced alterations such as (1) excitement of effective metabolic and hemodynamic connectivity from left to right PFC in the E band, (2) inhibition of effective metabolic and hemodynamic connectivity from left to right PFC in the N band, (3) decrease of unilateral causal coupling between HbO and CCO connectivity in E and N band over ipsilateral and contralateral PFCs, (4) increase of unilateral effective coupling from HbO to EEG and CCO to EEG in E band, and (5) enhancement of unilateral coupling between HbO and EEG in E band. The reported observations prove the complex mechanism of action of tPBM where it simultaneously affects the hemodynamics and metabolism directly which leads to an increase in the electrophysiological activity. Based on the ongoing studies focusing on the neurophysiological disorder and their corresponding changes in each metric, we suggest that tPBM can be considered as a potential method to reverse the neurophysiological deficiency.

Chapter 6

Conclusion

6.1 Summary of the Dissertation

As the first aim of my dissertation, I utilized three analysis steps to identify the electrophysiological effects of tPBM in a healthy human brain. First, power spectral analysis revealed that alterations in EEG spectral powers were mainly present in the alpha and beta bands of the fronto-central-parietal regions. Second, a topological approach, GTA, facilitated findings on significant modulation of the EEG beta rhythm in the information path and enhancement of the brain network complexity at the global network level during and after the stimulation. Finally, assessment of the nodal measures of the network at the regional and cluster levels confirmed that tPBM had a major effect on the frontal and parietal clusters in the beta band. The information paths were enhanced during and post tPBM in the prefrontal regions near the stimulation site.

In the second aim, as represented in chapter 3, I hypothesized that 2-bbNIRS, along with frequency-domain analysis, enables the quantification of prefrontal cortical connectivity and coupling of ISO in the resting human brain. To test this hypothesis, I implemented 2-channel bbNIRS and performed bilateral, prefrontal, 7-min measurements in an eyes-closed resting state in vivo from 26 young and healthy participants, repeated 5 times over 5 weeks. The measured time series were analyzed using a frequency-domain approach to detect cerebral hemodynamic and metabolic ISO in three endogenic, neurogenic, and myogenic frequency bands at rest. Specifically, coherence analysis facilitated the quantification of bilateral connectivity and unilateral hemodynamic-metabolic coupling in the human prefrontal regions. Accordingly, I identified eight stable resting-state ISO-specific metrics or features, including bilaterally averaged SA_{HbO} in all three bands, bilaterally averaged SA_{CCO} in the M band only, and bilaterally connected network metrics for both $bCON_{HbO}$ and $bCON_{CCO}$, each of which were statistically identical in the E and N frequency bands, respectively. The last two features were the bilaterally averaged coupling indices of $uCOP_{HbO\text{-}CCO}$ over the E- and M-bands, given that the coupling indices were statistically equivalent for both bands.

As the third aim, I hypothesized that the tPBM-induced alterations in the bilateral prefrontal neurophysiological states can be monitored and quantified by the spectral amplitudes of hemodynamic and metabolic activity ipsilateral and contralateral to the stimulation site, bilateral hemodynamic and metabolic connectivity, and unilateral hemodynamic-metabolic coupling ipsilateral and contralateral to the stimulation site. To assess this hypothesis, I implemented 2-channel bbNIRS measurements including 7-min pre- and 7-min post-stimulation at eyes-closed resting state from 26 young healthy participants. The measurement was repeated 5 times for all participants over 5 weeks with different 8-min stimulation conditions, namely, (1) Right prefrontal 800-nm tPBM, (2) Right prefrontal 850-nm tPBM, (3) Right prefrontal sham, (4) Left prefrontal 800-nm tPBM, (5) Left prefrontal sham stimulation.

The 7-min post-stimulation dual-channel bbNIRS measurements enabled to identify the wavelength- and location-independent tPBM-induced alterations such as (1) excitement of ipsilateral hemodynamic spectral amplitude in E band, (2) inhibition of contralateral metabolic spectral amplitude in E band, (3) decrease of bilateral hemodynamic connectivity in M band, (4) decrease of bilateral metabolic connectivity in N band, and (5) increase of unilateral hemodynamic-metabolic coupling in E band. Furthermore, the reported observations reveal that despite high levels of similarities among different tPBM conditions, there still are differences in some details regarding the wavelength and stimulation site.

In the fourth aim, as presented in chapter 5, I showed that prefrontal cortical connectivity and coupling of ISO in the resting human brain can be quantified using dual-mode (i.e., 2-bbNIRS and EEG) and may serve as features to reflect brain state. The measured time series were analyzed to detect cerebral hemodynamic, metabolic, and electrophysiological ISO at rest. MVAR model followed by GPDC was utilized to construct the bilateral metabolic-vascular and unilateral physiological networks. Then, I defined and investigated several ISO-specific metrics, including bilateral connectivity for both hemodynamic and metabolic activity, and unilateral MVC, NVC, and NMC at rest. The essential rationale of the proposed biomarkers was that the success of separating the three ISO components of prefrontal hemodynamics and metabolism would enable to detect and distinguish neurophysiological disorders (e.g., age-related cognition impairments, cardiovascular disease, Alzheimer’s disease, hypertension, and stroke) based on sources of impaired or abnormal signals (e.g., endothelium, inter-neuron, or smooth muscle).

The 7-min post-stimulation dual-modality measurements enabled to identify the ISO frequency-specific tPBM-induced alterations such as (1) excitement of effective metabolic and hemodynamic connectivity from left to right PFC in the E band, (2) inhibition of effective metabolic and hemodynamic connectivity from left to right PFC in the N band, (3) decrease of unilateral causal coupling between HbO and CCO connectivity in E and N band over ipsilateral and contralateral PFCs, (4) increase of unilateral effective coupling from HbO to EEG and CCO to EEG in E band, and (5) enhancement of unilateral coupling between HbO and EEG in E band. The reported observations prove the complex mechanism of action of tPBM where it simultaneously affects the hemodynamics and metabolism directly which leads to an increase in the electrophysiological activity.

6.2 Limitations and Future Works

Regarding 64-channel EEG study, the international 10–10 electrode placement system in the EEG study was not strictly followed on the human head because a clear area with 4.2 cm in diameter was needed for tPBM light delivery on the right forehead. The EEG cap was shifted 1–2 cm backward. There was a systematic shift in the electrode locations given in Figs. 4 and 6 with respect to the standard 64-electrode locations. Second, the power spectral and connectivity analyses were performed in the sensor space. Source space analysis can be conducted to observe specific cortical and subcortical regions in the brain affected by tPBM. Third, the current study was based on EEG signals of the tPBM-treated human brain in the resting state without the evaluation of any behavioural assessment. It is highly desirable to obtain concurrent assessments of changes in brain connectivity metrics and cognitive enhancement after tPBM. A combination of electrophysiological and behavioural measures would provide more informative and comprehensive views of the correlation and association between functional connectivity and behavioural effects of tPBM. Overall, there are few publications in the literature on how tPBM affects brain connectivity and the association between tPBM-induced network changes and cognitive improvement.

In the case of bbNIRS-based studies, the relatively low sampling frequency and short data collection duration (i.e., 7-min) prevented us from achieving high-frequency resolution, which may have led to low accuracy in spectral amplitude and coherence calculations in the low-frequency range, especially in the endogenic band. It is suggested to have a longer measurement duration, for example, 10 min or longer. Second, our bbNIRS system was sensitive to motion; the eyes-closed resting-state protocol may have caused sleepiness in the participants during the measurements. Finally, our quantified results or metrics may be contaminated by the extracranial layers of the human head. It is known that fNIRS signals obtained over the scalp of human participants are contaminated by extracranial layers, namely, the human scalp and skull. To minimize this potential confounding factor, additional optical channels of fNIRS with a short source-detector (S-D) separation (commonly ~0.8-1.2 cm) have been used for systemic noise removal in task-evoked hemodynamic studies [162, 163] [164] [165, 166], where a cortical region was activated by stimulating tasks. However, most fNIRS-based studies for quantifying resting-state functional connectivity (RSFC) have not developed an appropriate methodology to remove this confounding effect [147, 148]. It is reported only recently that RSFC can be quantified more accurately with a short S-D reading correction than without correction [167].

In future work, to enable a longer-period and less-artifact recording from the human brain, modifications or improvements are needed in the bbNIRS setup, measurement protocol, and computational methods to reduce movement artifacts and systemic/physiological noises. In addition, it is necessary to consider the implementation of short-distance channels in bbNIRS to remove the possible contamination of extracranial layers from the determined/interpreted results. The current study included only healthy controls without any disease-related patients; thus, it was an exploratory study [42]. While we believe that the identified ISO features are good neurological representations of the human brain, proof-of-principle or confirmatory research must be conducted for these features to become biomarkers of neurological diseases. It is also necessary to promote and conduct more investigations in this line of work to make tPBM a non-invasive, portable, and low-cost intervention tool for healing patients with certain brain disorders as well as for healthy aging in the rapidly growing aging population.

References

[1] J. C. Rojas and F. Gonzalez-Lima, "Low-level light therapy of the eye and brain," *Eye Brain,* vol. 3, pp. 49-67, 2011, doi: 10.2147/EB.S21391.

[2] D. W. Barrett and F. Gonzalez-Lima, "Transcranial infrared laser stimulation produces beneficial cognitive and emotional effects in humans," (in en), *Neuroscience,* vol. 230, pp. 13-23, 2013/01/29/ 2013, doi: 10.1016/j.neuroscience.2012.11.016.

[3] N. J. Blanco, W. T. Maddox, and F. Gonzalez-Lima, "Improving executive function using transcranial infrared laser stimulation," *Journal of Neuropsychology,* vol. 11, no. 1, pp. 14-25, 2017/03/01/ 2017, doi: 10.1111/jnp.12074.

[4] N. J. Blanco, C. L. Saucedo, and F. Gonzalez-Lima, "Transcranial infrared laser stimulation improves rule-based, but not information-integration, category learning in humans," *Neurobiology of Learning and Memory,* vol. 139, pp. 69-75, 2017/03/01/ 2017, doi: https://doi.org/10.1016/j.nlm.2016.12.016.

[5] E. Vargas *et al.*, "Beneficial neurocognitive effects of transcranial laser in older adults," *Lasers Med Sci,* vol. 32, no. 5, pp. 1153-1162, Jul 2017, doi: 10.1007/s10103-017-2221-y.

[6] C. M. O'Donnell, D. W. Barrett, L. H. Fink, E. C. Garcia-Pittman, and F. Gonzalez-Lima, "Transcranial Infrared Laser Stimulation Improves Cognition in Older Bipolar Patients: Proof of Concept Study," *J Geriatr Psychiatry Neurol,* p. 891988720988906, Feb 2 2021, doi: 10.1177/0891988720988906.

[7] X. Wang *et al.*, "Up-regulation of cerebral cytochrome-c-oxidase and hemodynamics by transcranial infrared laser stimulation: A broadband near-infrared spectroscopy study," *J Cereb Blood Flow Metab,* vol. 37, no. 12, pp. 3789-3802, Dec 2017, doi: 10.1177/0271678X17691783.

[8] Q. Wu, X. Wang, H. Liu, and L. Zeng, "Learning Hemodynamic Effect of Transcranial Infrared Laser Stimulation Using Longitudinal Data Analysis," *IEEE Journal of Biomedical and Health Informatics,* pp. 1-1, 2019, doi: 10.1109/JBHI.2019.2951772.

[9] T. Pruitt, X. Wang, A. Wu, E. Kallioniemi, M. M. Husain, and H. Liu, "Transcranial Photobiomodulation (tPBM) With 1,064-nm Laser to Improve Cerebral Metabolism of the Human Brain In Vivo," *Lasers Surg Med,* vol. 52, no. 9, pp. 807-813, Nov 2020, doi: 10.1002/lsm.23232.

[10] T. Karu, "Primary and secondary mechanisms of action of visible to near-IR radiation on cells," *J Photochem Photobiol B,* vol. 49, no. 1, pp. 1-17, Mar 1999, doi: 10.1016/S1011-1344(98)00219-X.

[11] H. Chung, T. Dai, S. K. Sharma, Y. Y. Huang, J. D. Carroll, and M. R. Hamblin, "The nuts and bolts of low-level laser (light) therapy," *Ann Biomed Eng,* vol. 40, no. 2, pp. 516-33, Feb 2012, doi: 10.1007/s10439-011-0454-7.

[12] T. Pruitt, C. Carter, X. Wang, A. Wu, and H. Liu, "Photobiomodulation at Different Wavelengths Boosts Mitochondrial Redox Metabolism and Hemoglobin Oxygenation: Lasers vs. Light-Emitting Diodes In Vivo," *Metabolites,* vol. 12, no. 2, p. 103, 2022.

[13] A. M. Bastos and J. M. Schoffelen, "A Tutorial Review of Functional Connectivity Analysis Methods and Their Interpretational Pitfalls," *Front Syst Neurosci,* vol. 9, p. 175, 2015, doi: 10.3389/fnsys.2015.00175.

[14] K. J. Friston, "Functional and effective connectivity in neuroimaging: a synthesis," *Human brain mapping,* vol. 2, no. 1-2, pp. 56-78, 1994.

[15] C. Rosazza and L. Minati, "Resting-state brain networks: literature review and clinical applications," *Neurol Sci,* vol. 32, no. 5, pp. 773-85, Oct 2011, doi: 10.1007/s10072-011-0636-y.

[16] L. Beynel, J. P. Powers, and L. G. Appelbaum, "Effects of repetitive transcranial magnetic stimulation on resting-state connectivity: A systematic review," *Neuroimage,* vol. 211, p. 116596, 2020.

[17] R. Jain and A. G. Ramakrishnan, "Electrophysiological and neuroimaging studies–during resting state and sensory stimulation in disorders of consciousness: a review," *Frontiers in Neuroscience,* vol. 14, p. 987, 2020.

[18] M. Mondino, S. Ghumman, C. Gane, E. Renauld, K. Whittingstall, and S. Fecteau, "Effects of transcranial stimulation with direct and alternating current on resting-state functional connectivity: An exploratory study simultaneously combining stimulation and multiband functional magnetic resonance imaging," *Frontiers in human neuroscience,* vol. 13, p. 474, 2020.

[19] A. H. Meghdadi *et al.*, "Resting state EEG biomarkers of cognitive decline associated with Alzheimer's disease and mild cognitive impairment," *PloS one*, vol. 16, no. 2, p. e0244180, 2021.

[20] M. Seraji, M. Mohebbi, A. Safari, and B. Krekelberg, "Multiple sclerosis reduces synchrony of the magnocellular pathway," *PLoS One,* vol. 16, no. 8, p. e0255324, 2021, doi: 10.1371/journal.pone.0255324.

[21] L. F. Chalak *et al.*, "Novel Wavelet Real Time Analysis of Neurovascular Coupling in Neonatal Encephalopathy," *Sci Rep,* vol. 7, p. 45958, Apr 10 2017, doi: 10.1038/srep45958.

[22] Y. Das, X. Wang, S. Kota, R. Zhang, H. Liu, and L. F. Chalak, "Neurovascular coupling (NVC) in newborns using processed EEG versus amplitude-EEG," *Scientific reports,* vol. 11, no. 1, pp. 1-7, 2021.

[23] D. Hendrikx *et al.*, "Measurement of Neurovascular Coupling in Neonates," *Front Physiol,* vol. 10, p. 65, 2019, doi: 10.3389/fphys.2019.00065.

[24] M. Nourhashemi, M. Mahmoudzadeh, S. Goudjil, G. Kongolo, and F. Wallois, "Neurovascular coupling in the developing neonatal brain at rest," *Human brain mapping,* vol. 41, no. 2, pp. 503-519, 2020.

[25] P. Pinti, M. F. Siddiqui, A. D. Levy, E. J. H. Jones, and I. Tachtsidis, "An analysis framework for the integration of broadband NIRS and EEG to assess neurovascular and neurometabolic coupling," *Sci Rep,* vol. 11, no. 1, p. 3977, Feb 17 2021, doi: 10.1038/s41598-021-83420-9.

[26] L. Minati, G. Varotto, L. D'Incerti, F. Panzica, and D. Chan, "From brain topography to brain topology: relevance of graph theory to functional neuroscience," *Neuroreport,* vol. 24, no. 10, pp. 536-543, 2013.

[27] X. Wang, H. Wanniarachchi, A. Wu, F. Gonzalez-Lima, and H. Liu, "Transcranial photobiomodulation and thermal stimulation induce distinct topographies of EEG alpha and beta power changes in healthy humans," *Sci Rep,* vol. 11, no. 1, p. 18917, Sep 23 2021, doi: 10.1038/s41598-021-97987-w.

[28] X. Wang, H. Wanniarachchi, A. Wu, and H. Liu, "Combination of Group Singular Value Decomposition and eLORETA Identifies Human EEG Networks and Responses to Transcranial Photobiomodulation," *Front Hum Neurosci,* vol. 16, p. 853909, 2022, doi: 10.3389/fnhum.2022.853909.

[29] R. Zomorrodi, G. Loheswaran, A. Pushparaj, and L. Lim, "Pulsed Near Infrared Transcranial and Intranasal Photobiomodulation Significantly Modulates Neural Oscillations: a pilot exploratory study," *Sci Rep,* vol. 9, no. 1, p. 6309, Apr 19 2019, doi: 10.1038/s41598-019-42693-x.

[30] A. H. Ghaderi, A. Jahan, F. Akrami, and M. Moghadam Salimi, "Transcranial photobiomodulation changes topology, synchronizability, and complexity of resting state brain networks," *J Neural Eng,* vol. 18, no. 4, May 10 2021, doi: 10.1088/1741-2552/abf97c.

[31] L. A. Brown, B. J. Key, and T. A. Lovick, "Inhibition of vasomotion in hippocampal cerebral arterioles during increases in neuronal activity," *Auton Neurosci,* vol. 95, no. 1-2, pp. 137-40, Jan 10 2002, doi: 10.1016/s1566-0702(01)00395-2.

[32] A. Vermeij, A. S. Meel-van den Abeelen, R. P. Kessels, A. H. van Beek, and J. A. Claassen, "Very-low-frequency oscillations of cerebral hemodynamics and blood pressure are affected by aging and cognitive load," *Neuroimage,* vol. 85 Pt 1, pp. 608-15, Jan 15 2014, doi: 10.1016/j.neuroimage.2013.04.107.

[33] D. F. van Helden and M. S. Imtiaz, "Venous Vasomotion," *Adv Exp Med Biol,* vol. 1124, pp. 313-328, 2019, doi: 10.1007/978-981-13-5895-1_13.

[34] F. J. Klocke, "Epicardial coronary artery vasomotion," *J Am Coll Cardiol,* vol. 56, no. 20, pp. 1666-7, Nov 9 2010, doi: 10.1016/j.jacc.2010.05.048.

[35] C. Rivadulla, C. de Labra, K. L. Grieve, and J. Cudeiro, "Vasomotion and neurovascular coupling in the visual thalamus in vivo," *PLoS One,* vol. 6, no. 12, p. e28746, 2011, doi: 10.1371/journal.pone.0028746.

[36] M. P. Wiedeman, "Effect of venous flow on frequency of venous vasomotion in the bat wing," *Circ Res,* vol. 5, no. 6, pp. 641-4, Nov 1957, doi: 10.1161/01.res.5.6.641.

[37] D. G. Buerk and C. E. Riva, "Vasomotion and spontaneous low-frequency oscillations in blood flow and nitric oxide in cat optic nerve head," *Microvasc Res,* vol. 55, no. 1, pp. 103-12, Jan 1998, doi: 10.1006/mvre.1997.2053.

[38] B. M. Bosch, A. Bringard, G. Ferretti, S. Schwartz, and K. Igloi, "Effect of cerebral vasomotion during physical exercise on associative memory, a near-infrared spectroscopy study," *Neurophotonics,* vol. 4, no. 4, p. 041404, Oct 2017, doi: 10.1117/1.NPh.4.4.041404.

[39] J. A. Vita and J. F. Keaney, Jr., "Endothelial function: a barometer for cardiovascular risk?," *Circulation,* vol. 106, no. 6, pp. 640-2, Aug 6 2002, doi: 10.1161/01.cir.0000028581.07992.56.

[40] J. E. Deanfield, J. P. Halcox, and T. J. Rabelink, "Endothelial function and dysfunction: testing and clinical relevance," *Circulation,* vol. 115, no. 10, pp. 1285-95, Mar 13 2007, doi: 10.1161/CIRCULATIONAHA.106.652859.

[41] L. Y. Di Marco, E. Farkas, C. Martin, A. Venneri, and A. F. Frangi, "Is vasomotion in cerebral arteries impaired in Alzheimer's disease?," *Journal of Alzheimer's Disease,* vol. 46, no. 1, pp. 35-53, 2015.

[42] B. Hallingberg *et al.*, "Exploratory studies to decide whether and how to proceed with full-scale evaluations of public health interventions: a systematic review of guidance," *Pilot Feasibility Stud,* vol. 4, p. 104, 2018, doi: 10.1186/s40814-018-0290-8.

[43] X. Wang, L.-C. Ma, S. Shahdadian, A. Wu, N. C. D. Truong, and H. Liu, "Metabolic Connectivity and Hemodynamic-Metabolic Coherence of Human Prefrontal Cortex at Rest and Post Photobiomodulation Assessed by Dual-Channel Broadband NIRS," *Metabolites,* vol. 12, no. 1, p. 42, 2022.

[44] S. Shahdadian, X. Wang, S. Kang, C. Carter, A. Chaudhari, and H. Liu, "Prefrontal Cortical Connectivity and Coupling of Infraslow Oscillation in the Resting Human Brain: A Two-Channel Broadband NIRS Study," *Cerebral Cortex Communications,* In Press.

[45] M. T. T. Wong-Riley *et al.*, "Photobiomodulation Directly Benefits Primary Neurons Functionally Inactivated by Toxins: ROLE OF CYTOCHROME c OXIDASE," *Journal of Biological Chemistry,* vol. 280, no. 6, pp. 4761-4771, 2005. [Online]. Available: http://www.jbc.org/content/280/6/4761.abstract.

[46] F. Gonzalez-Lima and D. W. Barrett, "Augmentation of cognitive brain functions with transcranial lasers," *Front Syst Neurosci,* vol. 8, p. 36, 2014, doi: 10.3389/fnsys.2014.00036.

[47] M. R. Hamblin, "Shining light on the head: Photobiomodulation for brain disorders," *BBA Clin,* vol. 6, pp. 113-124, Dec 2016, doi: 10.1016/j.bbacli.2016.09.002.

[48] M. A. Naeser, A. Saltmarche, M. H. Krengel, M. R. Hamblin, and J. A. Knight, "Improved cognitive function after transcranial, light-emitting diode treatments in chronic, traumatic brain injury: two case reports," *Photomed Laser Surg,* vol. 29, no. 5, pp. 351-8, May 2011, doi: 10.1089/pho.2010.2814.

[49] M. A. Naeser *et al.*, "Significant improvements in cognitive performance post-transcranial, red/near-infrared light-emitting diode treatments in chronic, mild traumatic brain injury: open-protocol study," *J Neurotrauma,* vol. 31, no. 11, pp. 1008-17, Jun 1 2014, doi: 10.1089/neu.2013.3244.

[50] M. R. Hamblin, "Photobiomodulation for traumatic brain injury and stroke," *J Neurosci Res,* vol. 96, no. 4, pp. 731-743, Apr 2018, doi: 10.1002/jnr.24190.

[51] M. G. Figueiro Longo *et al.*, "Effect of Transcranial Low-Level Light Therapy vs Sham Therapy Among Patients With Moderate Traumatic Brain Injury: A Randomized Clinical Trial," *JAMA Netw Open*, vol. 3, no. 9, p. e2017337, Sep 1 2020, doi: 10.1001/jamanetworkopen.2020.17337.

[52] J. C. Rojas and F. Gonzalez-Lima, "Neurological and psychological applications of transcranial lasers and LEDs," *Biochem Pharmacol,* vol. 86, no. 4, pp. 447-57, Aug 15 2013, doi: 10.1016/j.bcp.2013.06.012.

[53] P. Cassano, "Transcranial Photobiomodulation for Psychiatric Disorders: Past and Future Directions," in *2018 Conference on Lasers and Electro-Optics (CLEO)*, 13-18 May 2018 2018, pp. 1-2.

[54] D. Nizamutdinov *et al.*, "Transcranial Near Infrared Light Stimulations Improve Cognition in Patients with Dementia," *Aging Dis,* vol. 12, no. 4, pp. 954-963, Jul 2021, doi: 10.14336/AD.2021.0229.

[55] A. S. Chan, T. L. Lee, M. R. Hamblin, and M. C. Cheung, "Photobiomodulation Enhances Memory Processing in Older Adults with Mild Cognitive Impairment: A Functional Near-Infrared Spectroscopy Study," *Journal of Alzheimer's disease : JAD,* vol. 83, no. 4, pp. 1471-1480, 2021, doi: 10.3233/JAD-201600.

[56] G. Dougal, A. Ennaceur, and P. L. Chazot, "Effect of Transcranial Near-Infrared Light 1068 nm Upon Memory Performance in Aging Healthy Individuals: A Pilot Study," *Photobiomodul Photomed Laser Surg,* vol. 39, no. 10, pp. 654-660, Oct 2021, doi: 10.1089/photob.2020.4956.

[57] X. Wang, D. D. Reddy, S. S. Nalawade, S. Pal, F. Gonzalez-Lima, and H. Liu, "Impact of heat on metabolic and hemodynamic changes in transcranial infrared laser stimulation measured by broadband near-infrared spectroscopy," *Neurophotonics,* vol. 5, no. 1, p. 011004, 2017/09// 2017, doi: 10.1117/1.NPh.5.1.011004.

[58] S. Shahdadian, N. C. D. Truong, X. Wang, and H. Liu, "Effects of signal fluctuations in broadband near-infrared spectroscopy (bb-NIRS) on concentration quantification," 2021: Optical Society of America, p. JTu4A. 15.

[59] N. C. D. Truong, S. Shahdadian, X. Wang, and H. Liu, "How random measurement errors propagate to the chromophore concentration calculation in broadband near-infrared spectroscopy," 2021: Optical Society of America, p. JTu4A. 24.

[60] M. H. Berman, M. R. Hamblin, and P. Chazot, "Chapter 4 - Photobiomodulation and Other Light Stimulation Procedures," in *Rhythmic Stimulation Procedures in Neuromodulation*, J. R. Evans and R. P. Turner Eds.: Academic Press, 2017, pp. 97-129.

[61] V. Spera *et al.*, "Pilot Study on Dose-Dependent Effects of Transcranial Photobiomodulation on Brain Electrical Oscillations: A Potential Therapeutic Target in Alzheimer's Disease," *J Alzheimers Dis,* vol. 83, no. 4, pp. 1481-1498, 2021, doi: 10.3233/JAD-210058.

[62] J. Hsu, *Multiple comparisons: theory and methods*. CRC Press, 1996.

[63] E. Maris and R. Oostenveld, "Nonparametric statistical testing of EEG-and MEG-data," *Journal of neuroscience methods,* vol. 164, no. 1, pp. 177-190 %@ 0165-0270, 2007.

[64] L. E. Ismail and W. Karwowski, "A Graph Theory-Based Modeling of Functional Brain Connectivity Based on EEG: A Systematic Review in the Context of Neuroergonomics," *IEEE Access,* vol. 8, pp. 155103-155135, 2020, doi: 10.1109/access.2020.3018995.

[65] M. Rubinov and O. Sporns, "Complex network measures of brain connectivity: uses and interpretations," *Neuroimage,* vol. 52, no. 3, pp. 1059-69, Sep 2010, doi: 10.1016/j.neuroimage.2009.10.003.

[66] M. Teplan, "Fundamentals of EEG measurement," *Measurement science review,* vol. 2, no. 2, pp. 1-11, 2002.

[67] J. Maltez, L. Hyllienmark, V. V. Nikulin, and T. Brismar, "Time course and variability of power in different frequency bands of EEG during resting conditions," *Neurophysiologie Clinique/Clinical Neurophysiology,* vol. 34, no. 5, pp. 195-202, 2004.

[68] V. Jurcak, D. Tsuzuki, and I. Dan, "10/20, 10/10, and 10/5 systems revisited: their validity as relative head-surface-based positioning systems," *Neuroimage,* vol. 34, no. 4, pp. 1600-11, Feb 15 2007, doi: 10.1016/j.neuroimage.2006.09.024.

[69] J. Wright, A. Ganesh, S. R. Rao, Y. Peng, and Y. Ma, "Robust principal component analysis: Exact recovery of corrupted low-rank matrices via convex optimization," in *NIPS*, 2009, vol. 58, pp. 289-298.

[70] E. J. Candès, X. Li, Y. Ma, and J. Wright, "Robust principal component analysis?," *Journal of the ACM (JACM),* vol. 58, no. 3, pp. 1-37, 2011.

[71] D. Lehmann and W. Skrandies, "Reference-free identification of components of checkerboard-evoked multichannel potential fields," *Electroencephalography and clinical neurophysiology,* vol. 48, no. 6, pp. 609-621, 1980.

[72] T.-P. Jung *et al.*, "Removing electroencephalographic artifacts by blind source separation," *Psychophysiology,* vol. 37, no. 2, pp. 163-178, 2000.

[73] A. Hyvärinen and E. Oja, "Simple neuron models for independent component analysis," *International Journal of Neural Systems,* vol. 7, no. 06, pp. 671-687, 1996.

[74] H. Li and T. Adali, "A class of complex ICA algorithms based on the kurtosis cost function," *IEEE Transactions on Neural Networks,* vol. 19, no. 3, pp. 408-420, 2008.

[75] J. J. Allen, J. A. Coan, and M. Nazarian, "Issues and assumptions on the road from raw signals to metrics of frontal EEG asymmetry in emotion," *Biological psychology,* vol. 67, no. 1-2, pp. 183-218, 2004.

[76] T. Popov, R. Oostenveld, and J. M. Schoffelen, "FieldTrip Made Easy: An Analysis Protocol for Group Analysis of the Auditory Steady State Brain Response in Time, Frequency, and Space," *Front Neurosci,* vol. 12, p. 711, 2018, doi: 10.3389/fnins.2018.00711.

[77] R. Oostenveld, P. Fries, E. Maris, and J.-M. Schoffelen, "FieldTrip: open source software for advanced analysis of MEG, EEG, and invasive electrophysiological data," *Computational intelligence and neuroscience,* vol. 2011, 2011.

[78] E. Maris and R. Oostenveld, "Nonparametric statistical testing of EEG- and MEG-data," *J Neurosci Methods,* vol. 164, no. 1, pp. 177-90, Aug 15 2007, doi: 10.1016/j.jneumeth.2007.03.024.

[79] J. Park, C. R. Lindberg, and F. L. Vernon III, "Multitaper spectral analysis of high-frequency seismograms," *Journal of Geophysical Research: Solid Earth,* vol. 92, no. B12, pp. 12675-12684, 1987.

[80] B. Babadi and E. N. Brown, "A review of multitaper spectral analysis," *IEEE Transactions on Biomedical Engineering,* vol. 61, no. 5, pp. 1555-1564, 2014.

[81] G. Nolte, O. Bai, L. Wheaton, Z. Mari, S. Vorbach, and M. Hallett, "Identifying true brain interaction from EEG data using the imaginary part of coherency," *Clin Neurophysiol,* vol. 115, no. 10, pp. 2292-307, Oct 2004, doi: 10.1016/j.clinph.2004.04.029.

[82] J. Wang, X. Wang, M. Xia, X. Liao, A. Evans, and Y. He, "GRETNA: a graph theoretical network analysis toolbox for imaging connectomics," *Frontiers in human neuroscience,* vol. 9, p. 386, 2015.

[83] E. Qazi, M. Hussain, and H. A. AboAlsamh, "Electroencephalogram (EEG) Brain Signals to Detect Alcoholism Based on Deep Learning," *Computers, Materials & Continua,* vol. 67, no. 3, pp. 3329-3348, 2021.

[84] J. Hwang, D. M. Castelli, and F. Gonzalez-Lima, "Cognitive enhancement by transcranial laser stimulation and acute aerobic exercise," *Lasers Med Sci,* vol. 31, no. 6, pp. 1151-60, Aug 2016, doi: 10.1007/s10103-016-1962-3.

[85] X. Wang, J. Dmochowski, M. Husain, F. Gonzalez-Lima, and H. Liu, "Proceedings #18. Transcranial Infrared Brain Stimulation Modulates EEG Alpha Power," *Brain Stimulation,* vol. 10, no. 4, pp. e67-e69, 2017/07/01/ 2017, doi: https://doi.org/10.1016/j.brs.2017.04.111.

[86] X. Wang *et al.*, "Transcranial photobiomodulation with 1064-nm laser modulates brain electroencephalogram rhythms," (in en), *Neurophotonics,* vol. 6, no. 02, p. 1, 2019/06/13/ 2019, doi: 10.1117/1.NPh.6.2.025013.

[87] S. Marek and N. U. Dosenbach, "The frontoparietal network: function, electrophysiology, and importance of individual precision mapping," *Dialogues in clinical neuroscience,* vol. 20, no. 2, p. 133, 2018.

[88] J. L. Cantero, M. Atienza, and R. M. Salas, "Human alpha oscillations in wakefulness, drowsiness period, and REM sleep: different electroencephalographic phenomena within the alpha band," *Neurophysiol Clin,* vol. 32, no. 1, pp. 54-71, Jan 2002, doi: 10.1016/s0987-7053(01)00289-1.

[89] W. Klimesch, "EEG-alpha rhythms and memory processes," *Int J Psychophysiol,* vol. 26, no. 1-3, pp. 319-40, Jun 1997, doi: 10.1016/s0167-8760(97)00773-3.

[90] S. Palva and J. M. Palva, "New vistas for alpha-frequency band oscillations," *Trends Neurosci,* vol. 30, no. 4, pp. 150-8, Apr 2007, doi: 10.1016/j.tins.2007.02.001.

[91] S. Hanslmayr, J. Gross, W. Klimesch, and K. L. Shapiro, "The role of alpha oscillations in temporal attention," *Brain Res Rev,* vol. 67, no. 1-2, pp. 331-43, Jun 24 2011, doi: 10.1016/j.brainresrev.2011.04.002.

[92] M. Hosťovecký and B. Babušiak, "Brain activity: beta wave analysis of 2D and 3D serious games using EEG," (in English), *Journal of Applied Mathematics, Statistics and Informatics,* vol. 13, no. 2, pp. 39-53, 2017, doi: https://doi.org/10.1515/jamsi-2017-0008.

[93] W. J. Ray and H. W. Cole, "EEG alpha activity reflects attentional demands, and beta activity reflects emotional and cognitive processes," *Science,* vol. 228, no. 4700, pp. 750-2, May 10 1985, doi: 10.1126/science.3992243.

[94] A. H. Ghaderi, B. R. Baltaretu, M. N. Andevari, V. Bharmauria, and F. Balci, "Synchrony and complexity in state-related EEG networks: an application of spectral graph theory," *Neural Computation,* vol. 32, no. 12, pp. 2422-2454, 2020.

[95] L. Yu and Y. Yu, "Energy-efficient neural information processing in individual neurons and neuronal networks," *Journal of Neuroscience Research,* vol. 95, no. 11, pp. 2253-2266, 2017.

[96] V. Saba *et al.*, "Brain connectivity and information-flow breakdown revealed by a minimum spanning tree-based analysis of MRI data in behavioral variant Frontotemporal dementia," *Frontiers in neuroscience,* vol. 13, p. 211, 2019.

[97] C. G. Antonopoulos, S. Srivastava, S. E. d. S. Pinto, and M. S. Baptista, "Do brain networks evolve by maximizing their information flow capacity?," *PLOS computational biology,* vol. 11, no. 8, p. e1004372, 2015.

[98] V. Spera *et al.*, "Pilot Study on Dose-Dependent Effects of Transcranial Photobiomodulation on Brain Electrical Oscillations: A Potential Therapeutic Target in Alzheimer's Disease," *Journal of Alzheimer's Disease,* no. Preprint, pp. 1-18, 2021.

[99] V. Spera *et al.*, "Transcranial Near-Infrared Light: Dose-Dependent Effects on EEG Oscillations but not Cerebral Blood Flow," *bioRxiv,* p. 837591, 2019, doi: 10.1101/837591.

[100] R. Schmidt, M. Herrojo Ruiz, B. E. Kilavik, M. Lundqvist, P. A. Starr, and A. R. Aron, "Beta Oscillations in Working Memory, Executive Control of Movement and Thought, and Sensorimotor Function," *J Neurosci,* vol. 39, no. 42, pp. 8231-8238, Oct 16 2019, doi: 10.1523/JNEUROSCI.1163-19.2019.

[101] F. Taya, Y. Sun, F. Babiloni, N. V. Thakor, and A. Bezerianos, "Topological Changes in the Brain Network Induced by the Training on a Piloting Task: An EEG-Based Functional Connectome Approach," *IEEE Trans Neural Syst Rehabil Eng,* vol. 26, no. 2, pp. 263-271, Feb 2018, doi: 10.1109/TNSRE.2016.2581809.

[102] J. Toppi *et al.*, "Different topological properties of EEG-derived networks describe working memory phases as revealed by graph theoretical analysis," *Frontiers in Human Neuroscience,* vol. 11, p. 637, 2018.

[103] G. Tononi, O. Sporns, and G. M. Edelman, "A measure for brain complexity: relating functional segregation and integration in the nervous system," *Proceedings of the National Academy of Sciences,* vol. 91, no. 11, pp. 5033-5037, 1994.

[104] L. C. Freeman, "Centrality in social networks conceptual clarification," *Social networks,* vol. 1, no. 3, pp. 215-239, 1978.

[105] T. Pruitt, X. Wang, H. Wanirachichi, and H. Liu, "Transcranial Photobiomodulation (tPBM) Recipients Present Information Flow Alterations in the Cortex: an eCONNECTOME Brain Space

ROI Analysis," in *Novel Techniques in Microscopy*, 2021: Optical Society of America, p. JTu4A. 27.

[106] T. J. Abel *et al.*, "Beta modulation reflects name retrieval in the human anterior temporal lobe: an intracranial recording study," *Journal of neurophysiology,* vol. 115, no. 6, pp. 3052-3061, 2016.

[107] M. E. Raichle and D. A. Gusnard, "Appraising the brain's energy budget," *Proc Natl Acad Sci U S A,* vol. 99, no. 16, pp. 10237-9, Aug 6 2002, doi: 10.1073/pnas.172399499.

[108] P. Magistretti and I. Allaman, "Brain energy metabolism," in *Neuroscience in the 21st century: from basic to clinical*: Springer New York, 2013, pp. 1591-1620.

[109] C. Mateo, P. M. Knutsen, P. S. Tsai, A. Y. Shih, and D. Kleinfeld, "Entrainment of Arteriole Vasomotor Fluctuations by Neural Activity Is a Basis of Blood-Oxygenation-Level-Dependent "Resting-State" Connectivity," *Neuron,* vol. 96, no. 4, pp. 936-948 e3, Nov 15 2017, doi: 10.1016/j.neuron.2017.10.012.

[110] X. H. Zhu, N. Zhang, Y. Zhang, K. Ugurbil, and W. Chen, "New insights into central roles of cerebral oxygen metabolism in the resting and stimulus-evoked brain," *J Cereb Blood Flow Metab,* vol. 29, no. 1, pp. 10-8, Jan 2009, doi: 10.1038/jcbfm.2008.97.

[111] A. Stefanovska, M. Bracic, and H. D. Kvernmo, "Wavelet analysis of oscillations in the peripheral blood circulation measured by laser Doppler technique," *IEEE Trans Biomed Eng,* vol. 46, no. 10, pp. 1230-9, Oct 1999, doi: 10.1109/10.790500.

[112] M. Bracic and A. Stefanovska, "Wavelet-based analysis of human blood-flow dynamics," *Bull Math Biol,* vol. 60, no. 5, pp. 919-35, Sep 1998, doi: 10.1006/bulm.1998.0047.

[113] A. Bernjak, P. B. Clarkson, P. V. McClintock, and A. Stefanovska, "Low-frequency blood flow oscillations in congestive heart failure and after beta1-blockade treatment," *Microvasc Res,* vol. 76, no. 3, pp. 224-32, Nov 2008, doi: 10.1016/j.mvr.2008.07.006.

[114] A. Mustari, N. Nakamura, S. Kawauchi, S. Sato, M. Sato, and I. Nishidate, "RGB camera-based imaging of cerebral tissue oxygen saturation, hemoglobin concentration, and hemodynamic spontaneous low-frequency oscillations in rat brain following induction of cortical spreading depression," *Biomed Opt Express,* vol. 9, no. 3, pp. 933-951, Mar 1 2018, doi: 10.1364/BOE.9.000933.

[115] H. D. Kvernmo, A. Stefanovska, K. A. Kirkeboen, and K. Kvernebo, "Oscillations in the human cutaneous blood perfusion signal modified by endothelium-dependent and endothelium-independent vasodilators," *Microvasc Res,* vol. 57, no. 3, pp. 298-309, May 1999, doi: 10.1006/mvre.1998.2139.

[116] R. Zhang, J. H. Zuckerman, K. Iwasaki, T. E. Wilson, C. G. Crandall, and B. D. Levine, "Autonomic neural control of dynamic cerebral autoregulation in humans," *Circulation,* vol. 106, no. 14, pp. 1814-20, Oct 1 2002, doi: 10.1161/01.cir.0000031798.07790.fe.

[117] J. M. Newman, R. M. Dwyer, P. St-Pierre, S. M. Richards, M. G. Clark, and S. Rattigan, "Decreased microvascular vasomotion and myogenic response in rat skeletal muscle in association with acute insulin resistance," *J Physiol,* vol. 587, no. Pt 11, pp. 2579-88, Jun 1 2009, doi: 10.1113/jphysiol.2009.169011.

[118] F. M. Faraci and D. D. Heistad, "Regulation of the cerebral circulation: role of endothelium and potassium channels," *Physiol Rev,* vol. 78, no. 1, pp. 53-97, Jan 1998, doi: 10.1152/physrev.1998.78.1.53.

[119] H. Girouard and C. Iadecola, "Neurovascular coupling in the normal brain and in hypertension, stroke, and Alzheimer disease," *J Appl Physiol (1985),* vol. 100, no. 1, pp. 328-35, Jan 2006, doi: 10.1152/japplphysiol.00966.2005.

[120] J. A. Schmidt, P. Borgstrom, and M. Intaglietta, "Neurogenic modulation of periodic hemodynamics in rabbit skeletal muscle," *J Appl Physiol (1985),* vol. 75, no. 3, pp. 1216-21, Sep 1993, doi: 10.1152/jappl.1993.75.3.1216.

[121] J. S. Damoiseaux *et al.*, "Consistent resting-state networks across healthy subjects," *Proc Natl Acad Sci U S A,* vol. 103, no. 37, pp. 13848-53, Sep 12 2006, doi: 10.1073/pnas.0601417103.

[122] E. W. Lang *et al.*, "Spontaneous oscillations of arterial blood pressure, cerebral and peripheral blood flow in healthy and comatose subjects," *Neurol Res,* vol. 21, no. 7, pp. 665-9, Oct 1999, doi: 10.1080/01616412.1999.11740995.

[123] X. Tang, Y. X. Luo, H. Z. Chen, and D. P. Liu, "Mitochondria, endothelial cell function, and vascular diseases," *Front Physiol,* vol. 5, p. 175, 2014, doi: 10.3389/fphys.2014.00175.

[124] H. Obrig *et al.*, "Spontaneous low frequency oscillations of cerebral hemodynamics and metabolism in human adults," *Neuroimage,* vol. 12, no. 6, pp. 623-39, Dec 2000, doi: 10.1006/nimg.2000.0657.

[125] J. C. Motzkin, J. P. Newman, K. A. Kiehl, and M. Koenigs, "Reduced prefrontal connectivity in psychopathy," *J Neurosci,* vol. 31, no. 48, pp. 17348-57, Nov 30 2011, doi: 10.1523/JNEUROSCI.4215-11.2011.

[126] F. S. Racz, P. Mukli, Z. Nagy, and A. Eke, "Increased prefrontal cortex connectivity during cognitive challenge assessed by fNIRS imaging," *Biomed Opt Express,* vol. 8, no. 8, pp. 3842-3855, Aug 1 2017, doi: 10.1364/BOE.8.003842.

[127] J. W. Yu *et al.*, "Prefrontal functional connectivity analysis of cognitive decline for early diagnosis of mild cognitive impairment: a functional near-infrared spectroscopy study," *Biomed Opt Express,* vol. 11, no. 4, pp. 1725-1741, Apr 1 2020, doi: 10.1364/BOE.382197.

[128] D. D. Jobson, Y. Hase, A. N. Clarkson, and R. N. Kalaria, "The role of the medial prefrontal cortex in cognition, ageing and dementia," *Brain Commun,* vol. 3, no. 3, p. fcab125, Jul 2021, doi: 10.1093/braincomms/fcab125.

[129] D. Sampath, M. Sathyanesan, and S. S. Newton, "Cognitive dysfunction in major depression and Alzheimer's disease is associated with hippocampal–prefrontal cortex dysconnectivity," *Neuropsychiatric Disease and Treatment,* vol. 13, p. 1509, 2017.

[130] R. E. Gagnon *et al.*, "Comparison of 13 published cytochrome c oxidase near-infrared spectroscopy algorithms," *European Journal of Applied Physiology and Occupational Physiology,* vol. 74, no. 6, pp. 487-495, 1996/12/01 1996, doi: 10.1007/BF02376763.

[131] C. Kolyva *et al.*, "Systematic investigation of changes in oxidized cerebral cytochrome c oxidase concentration during frontal lobe activation in healthy adults," *Biomed Opt Express,* vol. 3, no. 10, pp. 2550-66, Oct 1 2012, doi: 10.1364/BOE.3.002550.

[132] S. J. Matcher, C. E. Elwell, C. E. Cooper, M. Cope, and D. T. Delpy, "Performance comparison of several published tissue near-infrared spectroscopy algorithms," (in eng), *Anal Biochem,* vol. 227, no. 1, pp. 54-68, May 1 1995, doi: 10.1006/abio.1995.1252.

[133] B. W. Pogue and M. S. Patterson, "Error assessment of a wavelength tunable frequency domain system for noninvasive tissue spectroscopy," *J Biomed Opt,* vol. 1, no. 3, pp. 311-23, Jul 1996, doi: 10.1117/12.240679.

[134] K. Uludağ, J. Steinbrink, M. Kohl-Bareis, R. Wenzel, A. Villringer, and H. Obrig, "Cytochrome-c-oxidase redox changes during visual stimulation measured by near-infrared spectroscopy cannot be explained by a mere cross talk artefact," *NeuroImage,* vol. 22, no. 1, pp. 109-119, 2004/05/01/ 2004, doi: https://doi.org/10.1016/j.neuroimage.2003.09.053.

[135] A. Bainbridge *et al.*, "Brain mitochondrial oxidative metabolism during and after cerebral hypoxia-ischemia studied by simultaneous phosphorus magnetic-resonance and broadband near-infrared spectroscopy," *NeuroImage,* vol. 102 Pt 1, pp. 173-83, Nov 15 2014, doi: 10.1016/j.neuroimage.2013.08.016.

[136] G. Bale, S. Mitra, J. Meek, N. Robertson, and I. Tachtsidis, "A new broadband near-infrared spectroscopy system for in-vivo measurements of cerebral cytochrome-c-oxidase changes in neonatal brain injury," *Biomed Opt Express,* vol. 5, no. 10, pp. 3450-66, Oct 1 2014, doi: 10.1364/BOE.5.003450.

[137] J. T. Eells *et al.*, "Mitochondrial signal transduction in accelerated wound and retinal healing by near-infrared light therapy," *Mitochondrion,* vol. 4, no. 5-6, pp. 559-67, Sep 2004, doi: 10.1016/j.mito.2004.07.033.

[138] F. Gonzalez-Lima and A. Auchter, "Protection against neurodegeneration with low-dose methylene blue and near-infrared light," *Front Cell Neurosci,* vol. 9, p. 179, 2015, doi: 10.3389/fncel.2015.00179.

[139] F. Gonzalez-Lima, B. R. Barksdale, and J. C. Rojas, "Mitochondrial respiration as a target for neuroprotection and cognitive enhancement," *Biochem Pharmacol,* vol. 88, no. 4, pp. 584-93, Apr 15 2014, doi: 10.1016/j.bcp.2013.11.010.

[140] M. T. Wong-Riley *et al.*, "Photobiomodulation directly benefits primary neurons functionally inactivated by toxins: role of cytochrome c oxidase," *J Biol Chem,* vol. 280, no. 6, pp. 4761-71, Feb 11 2005, doi: 10.1074/jbc.M409650200.

[141] I. Tachtsidis, L. Gao, T. S. Leung, M. Kohl-Bareis, C. E. Cooper, and C. E. Elwell, "A hybrid multi-distance phase and broadband spatially resolved spectrometer and algorithm for resolving absolute concentrations of chromophores in the near-infrared light spectrum," (in eng), *Adv Exp Med Biol,* vol. 662, pp. 169-75, 2010, doi: 10.1007/978-1-4419-1241-1_24.

[142] X. Wang, F. Tian, S. S. Soni, F. Gonzalez-Lima, and H. Liu, "Interplay between up-regulation of cytochrome-c-oxidase and hemoglobin oxygenation induced by near-infrared laser," *Sci Rep,* vol. 6, p. 30540, Aug 3 2016, doi: 10.1038/srep30540.

[143] D. A. Boas, C. E. Elwell, M. Ferrari, and G. Taga, "Twenty years of functional near-infrared spectroscopy: introduction for the special issue," *NeuroImage,* vol. 85 Pt 1, pp. 1-5, Jan 15 2014, doi: 10.1016/j.neuroimage.2013.11.033.

[144] F. Tian, A. Yennu, A. Smith-Osborne, F. Gonzalez-Lima, C. S. North, and H. Liu, "Prefrontal responses to digit span memory phases in patients with post-traumatic stress disorder (PTSD): A functional near infrared spectroscopy study," *Neuroimage Clin,* vol. 4, pp. 808-19, 2014, doi: 10.1016/j.nicl.2014.05.005.

[145] A. Yennu, F. Tian, A. Smith-Osborne, J. G. R, F. L. Woon, and H. Liu, "Prefrontal responses to Stroop tasks in subjects with post-traumatic stress disorder assessed by functional near infrared spectroscopy," *Sci Rep,* vol. 6, p. 30157, 2016, doi: 10.1038/srep30157.

[146] H. Niu and Y. He, "Resting-state functional brain connectivity: lessons from functional near-infrared spectroscopy," *Neuroscientist,* vol. 20, no. 2, pp. 173-88, Apr 2014, doi: 10.1177/1073858413502707.

[147] L. Cai, Q. Dong, and H. Niu, "The development of functional network organization in early childhood and early adolescence: A resting-state fNIRS study," *Dev Cogn Neurosci,* vol. 30, pp. 223-235, Apr 2018, doi: 10.1016/j.dcn.2018.03.003.

[148] Z. Hu *et al.*, "Disrupted signal variability of spontaneous neural activity in children with attention-deficit/hyperactivity disorder," *Biomed Opt Express,* vol. 12, no. 5, pp. 3037-3049, May 1 2021, doi: 10.1364/BOE.418921.

[149] N. C. D. Truong, S. Shahdadian, S. Kang, X. Wang, and H. Liu, "Influence of the Signal-To-Noise Ratio on Variance of Chromophore Concentration Quantification in Broadband Near-Infrared Spectroscopy," *Frontiers in Photonics,* vol. 3, p. 908931, 2022, doi: 10.3389/fphot.2022.90893.

[150] D. B. Percival and A. T. Walden, *Spectral analysis for physical applications*. cambridge university press, 1993.

[151] W. L. Chen *et al.*, "Functional Near-Infrared Spectroscopy and Its Clinical Application in the Field of Neuroscience: Advances and Future Directions," *Front Neurosci,* vol. 14, p. 724, 2020, doi: 10.3389/fnins.2020.00724.

[152] E. M. Buckley, A. B. Parthasarathy, P. E. Grant, A. G. Yodh, and M. A. Franceschini, "Diffuse correlation spectroscopy for measurement of cerebral blood flow: future prospects," *Neurophotonics,* vol. 1, no. 1, p. 011009, 2014.

[153] T. Durduran and A. G. Yodh, "Diffuse correlation spectroscopy for non-invasive, micro-vascular cerebral blood flow measurement," *NeuroImage,* vol. 85 Pt 1, pp. 51-63, Jan 15 2014, doi: 10.1016/j.neuroimage.2013.06.017.

[154] Y. He *et al.*, "Ultra-Slow Single-Vessel BOLD and CBV-Based fMRI Spatiotemporal Dynamics and Their Correlation with Neuronal Intracellular Calcium Signals," *Neuron,* vol. 97, no. 4, pp. 925-939 e5, Feb 21 2018, doi: 10.1016/j.neuron.2018.01.025.

[155] H. Liu, S. M. Stufflebeam, J. Sepulcre, T. Hedden, and R. L. Buckner, "Evidence from intrinsic activity that asymmetry of the human brain is controlled by multiple factors," *Proc Natl Acad Sci U S A*, vol. 106, no. 48, pp. 20499-503, Dec 1 2009, doi: 10.1073/pnas.0908073106.

[156] J. A. Nielsen, B. A. Zielinski, M. A. Ferguson, J. E. Lainhart, and J. S. Anderson, "An evaluation of the left-brain vs. right-brain hypothesis with resting state functional connectivity magnetic resonance imaging," *PLoS One,* vol. 8, no. 8, p. e71275, 2013, doi: 10.1371/journal.pone.0071275.

[157] P. Salvi *et al.*, "Increase in slow-wave vasomotion by hypoxia and ischemia in lowlanders and highlanders," *Journal of applied physiology,* vol. 125 3, pp. 780-789, 2018.

[158] B. M. Bosch, A. Bringard, G. Ferretti, S. Schwartz, and K. Iglói, "Effect of cerebral vasomotion during physical exercise on associative memory, a near-infrared spectroscopy study," *Neurophotonics,* vol. 4, no. 4, p. 041404, 2017.

[159] M. Razavi, B. Eaton, S. Paradiso, M. Mina, A. G. Hudetz, and L. Bolinger, "Source of low-frequency fluctuations in functional MRI signal," *Journal of Magnetic Resonance Imaging: An Official Journal of the International Society for Magnetic Resonance in Medicine,* vol. 27, no. 4, pp. 891-897, 2008.

[160] C. Elwell, R. Springett, E. Hillman, and D. T. Delpy, "Oscillations in cerebral haemodynamics," in *Oxygen transport to tissue XXI*: Springer, 1999, pp. 57-65.

[161] S. Deng *et al.,* "Hemodynamic and metabolic correspondence of resting-state voxel-based physiological metrics in healthy adults," *Neuroimage,* vol. 250, p. 118923, Apr 15 2022, doi: 10.1016/j.neuroimage.2022.118923.

[162] Q. Zhang, E. N. Brown, and G. E. Strangman, "Adaptive filtering for global interference cancellation and real-time recovery of evoked brain activity: a Monte Carlo simulation study," *J Biomed Opt,* vol. 12, no. 4, p. 044014, Jul-Aug 2007, doi: 10.1117/1.2754714.

[163] F. Tian, H. Niu, B. Khan, G. Alexandrakis, K. Behbehani, and H. Liu, "Enhanced functional brain imaging by using adaptive filtering and a depth compensation algorithm in diffuse optical tomography," *IEEE transactions on medical imaging,* vol. 30, no. 6, pp. 1239-51, Jun 2011, doi: 10.1109/TMI.2011.2111459.

[164] M. A. Yucel *et al.,* "Short separation regression improves statistical significance and better localizes the hemodynamic response obtained by near-infrared spectroscopy for tasks with differing autonomic responses," *Neurophotonics,* vol. 2, no. 3, p. 035005, Jul 2015, doi: 10.1117/1.NPh.2.3.035005.

[165] J. A. Noah *et al.*, "Comparison of short-channel separation and spatial domain filtering for removal of non-neural components in functional near-infrared spectroscopy signals," *Neurophotonics,* vol. 8, no. 1, p. 015004, Jan 2021, doi: 10.1117/1.NPh.8.1.015004.

[166] X. Zhou, G. Sobczak, C. M. McKay, and R. Y. Litovsky, "Comparing fNIRS signal qualities between approaches with and without short channels," *PLoS One,* vol. 15, no. 12, p. e0244186, 2020.

[167] I. Paranawithana, D. Mao, Y. T. Wong, and C. M. McKay, "Reducing false discoveries in resting-state functional connectivity using short channel correction: an fNIRS study," *Neurophotonics,* vol. 9, no. 1, p. 015001, Jan 2022, doi: 10.1117/1.NPh.9.1.015001.

[168] M. R. Hamblin and Y. Y. Huang, Eds. *Photobiomodulation in the Brain*. San Diago, CA: Acamemic press, 2019.

[169] Q. Wu, X. Wang, H. Liu, and L. Zeng, "Learning Hemodynamic Effect of Transcranial Infrared Laser Stimulation Using Longitudinal Data Analysis," *IEEE J Biomed Health Inform,* vol. 24, no. 6, pp. 1772-1779, Jun 2020, doi: 10.1109/JBHI.2019.2951772.

[170] E. L. Urquhart, H. Wanniarachchi, X. Wang, F. Gonzalez-Lima, G. Alexandrakis, and H. Liu, "Transcranial photobiomodulation-induced changes in human brain functional connectivity and

network metrics mapped by whole-head functional near-infrared spectroscopy in vivo," *Biomed Opt Express*, vol. 11, no. 10, pp. 5783-5799, Oct 1 2020, doi: 10.1364/BOE.402047.

[171] X. Wang, D. D. Reddy, S. S. Nalawade, S. Pal, F. Gonzalez-Lima, and H. Liu, "Impact of heat on metabolic and hemodynamic changes in transcranial infrared laser stimulation measured by broadband near-infrared spectroscopy," *Neurophotonics*, vol. 5, no. 1, p. 011004, Jan 2018, doi: 10.1117/1.NPh.5.1.011004.

[172] N. C. D. Truong, S. Shahdadian, S. Kang, X. Wang, and H. Liu, "Influence of the Signal-To-Noise Ratio on Variance of Chromophore Concentration Quantification in Broadband Near-Infrared Spectroscopy," *Frontiers in Photonics*, p. 18, 2022.

[173] M. Yang, Z. Yang, T. Yuan, W. Feng, and P. Wang, "A Systemic Review of Functional Near-Infrared Spectroscopy for Stroke: Current Application and Future Directions," *Front Neurol*, vol. 10, p. 58, 2019, doi: 10.3389/fneur.2019.00058.

[174] X. Wang, F. Tian, S. S. Soni, F. Gonzalez-Lima, and H. Liu, "Interplay between up-regulation of cytochrome-c-oxidase and hemoglobin oxygenation induced by near-infrared laser," *Scientific Reports*, vol. 6, no. 1, p. 30540, 2016/08/03 2016, doi: 10.1038/srep30540.

[175] G. M. Dmochowski and J. P. Dmochowski, "Increased Blood Flow and Oxidative Metabolism in the Human Brain by Transcranial Laser Stimulation," *bioRxiv*, p. 459883, 2018, doi: 10.1101/459883.

[176] Y. Y. Huang *et al.*, "Transcranial low level laser (light) therapy for traumatic brain injury," *J Biophotonics*, vol. 5, no. 11-12, pp. 827-37, Nov 2012, doi: 10.1002/jbio.201200077.

[177] C. Thunshelle and M. R. Hamblin, "Transcranial Low-Level Laser (Light) Therapy for Brain Injury," *Photomed Laser Surg*, vol. 34, no. 12, pp. 587-598, Dec 2016, doi: 10.1089/pho.2015.4051.

[178] F. Salehpour, J. Mahmoudi, F. Kamari, S. Sadigh-Eteghad, S. H. Rasta, and M. R. Hamblin, "Brain Photobiomodulation Therapy: a Narrative Review," *Mol Neurobiol*, vol. 55, no. 8, pp. 6601-6636, Aug 2018, doi: 10.1007/s12035-017-0852-4.

[179] K. Masamoto, H. Hirase, and K. Yamada, *New horizons in neurovascular coupling: a bridge between brain circulation and neural plasticity*. Elsevier, 2016.

[180] C. Lecrux and E. Hamel, "Neuronal networks and mediators of cortical neurovascular coupling responses in normal and altered brain states," *Philosophical Transactions of the Royal Society B: Biological Sciences*, vol. 371, no. 1705, p. 20150350, 2016.

[181] N. C. D. Truong, X. Wang, H. Wanniarachchi, and H. Liu, "Enhancement of Frequency-Specific Hemodynamic Power and Functional Connectivity by Transcranial Photobiomodulation in Healthy Humans," *Frontiers in Neuroscience*, vol. 16, 2022.

[182] C.-Y. Chang, S.-H. Hsu, L. Pion-Tonachini, and T.-P. Jung, "Evaluation of artifact subspace reconstruction for automatic artifact components removal in multi-channel EEG recordings," *IEEE Transactions on Biomedical Engineering*, vol. 67, no. 4, pp. 1114-1121, 2019.

[183] K. J. Blinowska, "Review of the methods of determination of directed connectivity from multichannel data," *Med Biol Eng Comput*, vol. 49, no. 5, pp. 521-9, May 2011, doi: 10.1007/s11517-011-0739-x.

[184] P. Pinti, M. Siddiqui, A. Levy, E. Jones, and I. Tachtsidis, "An analysis framework for the integration of broadband NIRS and EEG to assess neurovascular and neurometabolic coupling," *Scientific reports*, vol. 11, no. 1, pp. 1-20, 2021.

[185] R. C. Webb, "Smooth muscle contraction and relaxation," *Advances in physiology education*, vol. 27, no. 4, pp. 201-206, 2003.

[186] G. M. Dmochowski, A. D. Shereen, D. Berisha, and J. P. Dmochowski, "Near-infrared light increases functional connectivity with a non-thermal mechanism," *Cerebral Cortex Communications*, vol. 1, no. 1, p. tgaa004, 2020.

[187] Anisha. TOST(sample1, sample2, d1, d2, alpha)

Appendix A

Table A1 Description of global and local graphical metrics significantly altered by tPBM ([65, 82])

Global graphical metrics	**Description of graph theory metrics significantly altered by tPBM**
Synchronization (*S*)	The *S* is the average of weighted or binarized functional connectivity index between all nodes in the network. It represents how likely it is that all nodes fluctuate in the same wave pattern. It ranges between 0 and 1.
Global Efficiency (*GE*)	The *GE* measures the efficiency of parallel information transfer in a network globally. It is inversely correlated with the characteristic shortest path of the network. The characteristic shortest path is the average of routes between all pairs of nodes with minimum number of edges. Also, the *GE* is associated with the level of integration and efficiency of parallel information transfer in a network. It ranges between 0 and 1.
Small-worldness (*SW*)	Small-world networks have a shorter characteristic path length than regular networks (which have high clustering and long path lengths) but greater local interconnectivity than random networks (which have low clustering coefficient and short path lengths). The *SW* supports both specialized/ modularized and integrated/distributed information processing and maximizes the efficiency of information transfer at a relatively low wiring cost.
Nodal Graphical metrics	***Description*** **of graph theory metrics significantly altered by tPBM**
Nodal Clustering Coefficient (*nCC*)	The *nCC* of a given node is associated with the numbers of triangles around that node. One triangle around a node will be constructed when two neighbors of the given node are connected. If all neighbors are connected, *C = 1* (the maximum value of *nCC*). In short, the *nCC* measures the likelihood that its neighborhoods are connected to each other.
Nodal Local Efficiency (*nLE*)	The *nLE* is the average of efficiency of local nodes. This index displays the level of segregation in the graph (comparable with the *nCC*). The *nLE* of a given node measures how efficient the

	communication is among the first neighbors of this node when it is removed.
Nodal Efficiency (*nE*)	The *nE* for a given node characterizes the efficiency of parallel information transfer of that node in the network. It is inversely correlated with the characteristic shortest path of one node to all other nodes in the network. It is associated with the level of integration of one node in the graph.
Betweenness Centrality (*BC*)	The *BC* represents the fraction of all shortest paths in the network that pass through a given node. The *BC* for a given node characterizes its effect on information flow between other nodes.
Degree Centrality (*DC*)	The *DC* is the number of connections between one node and all other nodes in the network. Nodes with a high degree are interacting with many other nodes in the network. The *DC* of a given node reflects its information communication ability in the functional network.

Appendix B

B.1 Steps for Frequency-Domain Data Analysis of Prefrontal Δ[HbO] and Δ[CCO] at Rest

Figure B1 shows a detailed flow chart and demonstrates the frequency analysis steps for a pair of signals, namely, Δ[HbO] and Δ[CCO]. These steps consist of two major functions available in the FieldTrip toolbox [76, 77], namely, "ft_freqanalysis" for amplitude and phase quantifications of each signal, and "ft_connectivityanalysis" for coherence quantification between the two signals.

As illustrated in this figure, the input for function "ft_freqanalysis" can be a single time series of two signals, followed by frequency-domain analysis using the multi-taper method (mtm) with *k* tapers. In this step, each tapered time series was subjected to a fast Fourier transform (FFT) to obtain the first set of outputs for this function. A total of k tapers resulted in k sets of complex numbers with their respective amplitudes and phases in the frequency range of the signal. Next, the mtm-based power spectral density (mtm-PSD) and spectral power were obtained for the input signal by averaging k sets of spectral powers. Accordingly, the respective spectral amplitude (SA) was calculated by taking the square root of the mtm-derived spectral power of the input time series (i.e., Δ[HbO] or Δ[CCO]) in the frequency band of interest. These steps are outlined by blue and orange boxes in Figure B1 for Δ[HbO] and Δ[CCO], respectively.

In addition, the outputs of *k* complex members from "ft_freqanalysis" are used as the inputs for function "ft_connectivityanalysis." This function quantifies the coherence index between the *i*th tapered output of the first signal and the corresponding (i.e., the *i*th) tapered output of the second signal. Each spectral coherence between a pair of temporal signals with the same *k*th taper was averaged over all *k* tapers, leading to the quantification of bilateral connectivity (i.e., $bCON_{HbO}$ and $bCON_{CCO}$) and unilateral coupling (i.e., $uCOP_{HbO\text{-}CCO}$) in all three E/N/M frequency bands, as marked by the three green boxes in the figure.

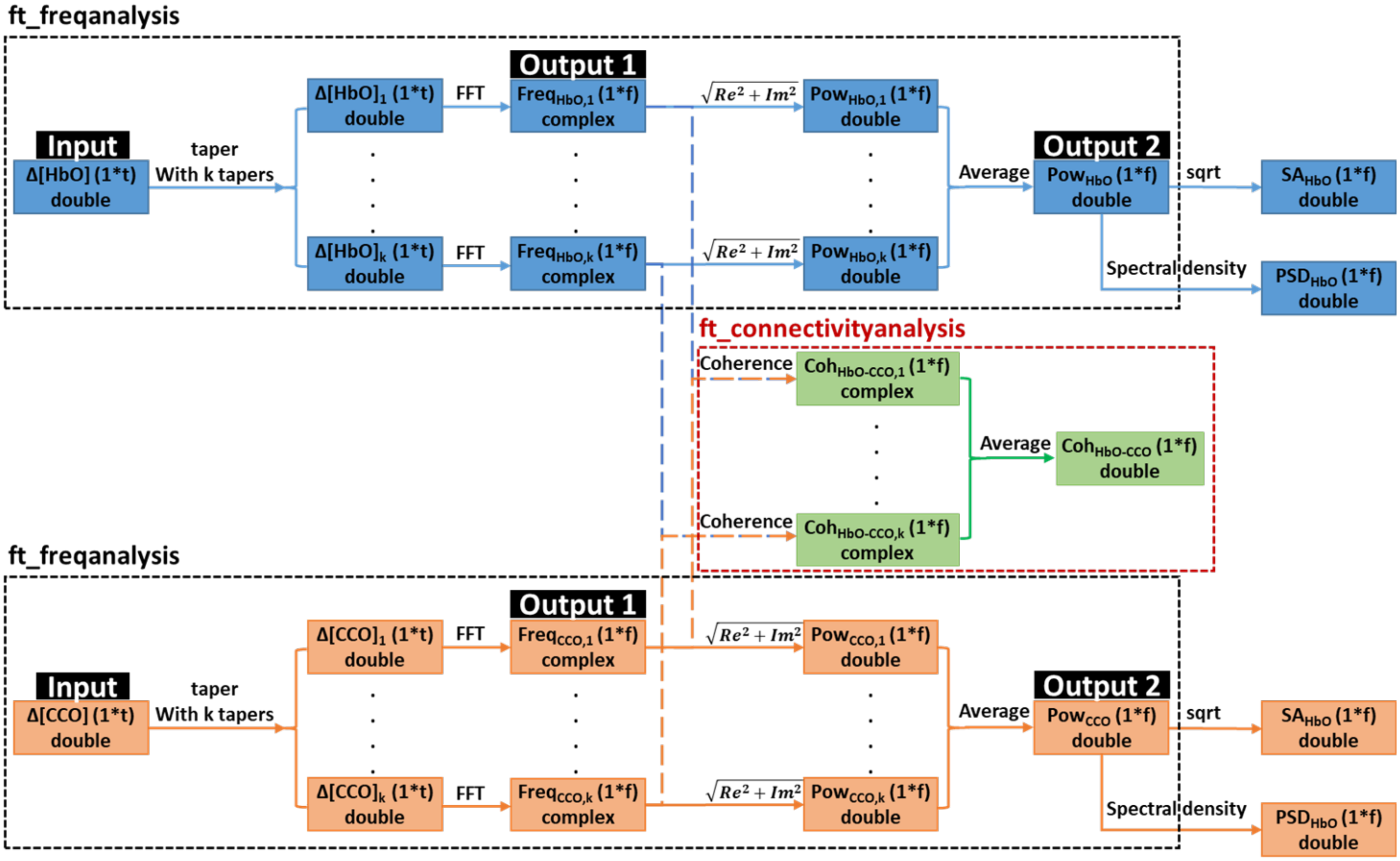

Figure B1 Schematic flow chart of spectral analysis for the quantification of SA and coherence. For demonstration, two time series, Δ[HbO] and Δ[CCO], are used as separate input signals with a time period of 't'. Blue and orange blocks represent frequency analysis steps operated on signal 1 (i.e., Δ[HbO]) and signal 2 (i.e., Δ[CCO]), using "ft_freqanalysis" function (outlined by black dashed boxes). The word of "double" and "complex" indicates a real number with double precision and a complex number, respectively. Furthermore, green blocks represent connectivity analysis steps operated on the frequency-domain outputs of the two signals, using "ft_connectivityanalysis" function (red dashed box).

B.2 Statistical Analysis for the Test of Equivalence Using the Two One-Sided Tests (TOST)

The two one-sided tests (TOST) analysis was utilized to evaluate the equivalence of the features that did not show a significant difference between right and left (for SA_{HbO}, SA_{CCO}, and $uCOP_{HbO\text{-}CCO}$) or between endogenic and neurogenic (for $bCON_{HbO}$ and $bCON_{CCO}$).

In each set of tests, the null hypothesis was that the means of the two samples were not equivalent. In principle, TOST returns two p-values (one for each side of the test). Thus, if both p-values obtained from this test are lower than the significance level threshold (i.e., 0.05), we can reject the null hypothesis and conclude that the means of the two samples are equivalent. In this method, a pair of lower and upper bounds for the feature must be determined, which is closely related to the hypothesis or the predefined effect size. In our study, for each feature in each frequency band, we defined the upper and lower bounds for the equivalence test as $M \times (1 \pm 0.2)$, where M is the average value of the two means of the two samples. In the case of statistically significant equivalence between the two samples (i.e., $p_{TOST} < 0.05$), the average of the tested features was also reported. A function of "TOST" in MATLAB was used in our analysis for TOST in this step of analysis [187].

B.3 Decomposition of a [HbO] Time Series into Three ISO Frequency Bands

Figure B2(a) shows an example of the Δ[HbO] time series from one channel of 2-bbNIRS in the dataset of a subject. Figures B2(b) to S2(d) were obtained after applying a Butterworth band-pass filter to the trace in Figure B2(a) using separate bandwidths of three endogenic (E:0.005-0.02 Hz), neurogenic (N:0.02-0.04 Hz), and myogenic (M:0.04-0.2 Hz) frequency ranges. This set of figures illustrates how different ISO components contribute to the composition of the wideband (0.005–0.2 Hz) original signal, as shown in Figure B2(a).

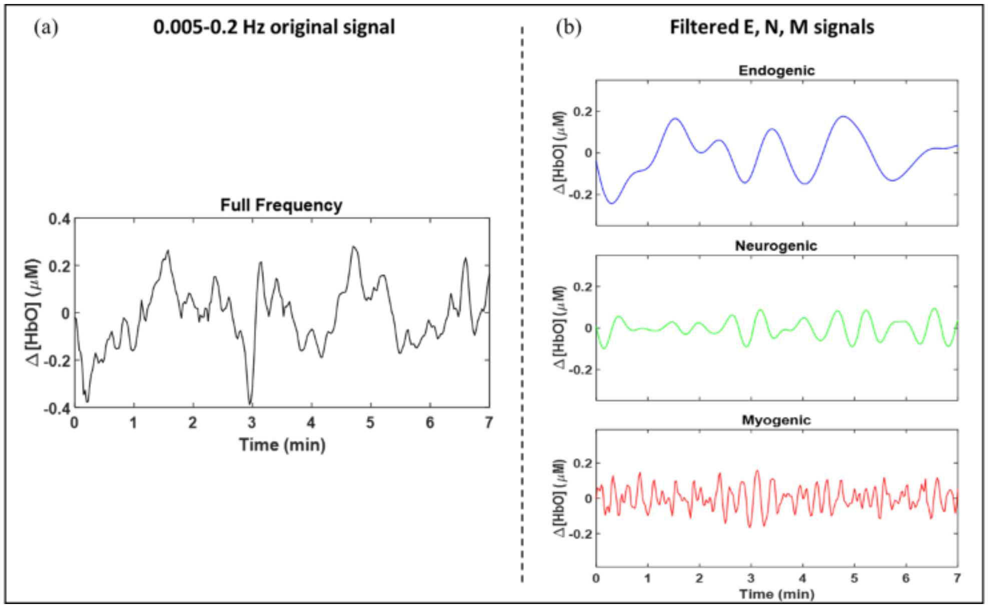

Figure B2 (a) A 7-min time series of Δ[HbO] derived from one channel of 2-bbNIRS of a subject's dataset. The three panels on the right were obtained after Butterworth band-pass filtering of the original signal in the three predefined E/N/M bands, namely, 0.005-0.02 Hz, 0.02-0.04 Hz, and 0.04-0.2 Hz, respectively.